







## Review

# A Brief Review of Atomistic Studies on BaTiO<sub>3</sub> as a Photocatalyst for Solar Water Splitting

Aisulu U. Abuova <sup>1</sup>, Ulzhan Zh. Tolegen <sup>1</sup>, Talgat M. Inerbaev <sup>1,2</sup>, Mirat Karibayev <sup>3</sup>, Balzhan M. Satanova <sup>1</sup>, Fatima U. Abuova <sup>1,\*</sup> and Anatoli I. Popov <sup>1,4,\*</sup>

- <sup>1</sup> Institute of Physical and Technical Sciences, L. N. Gumilyov Eurasian National University, Astana 010000, Kazakhstan; abuova\_au@enu.kz (A.U.A.); tolegen\_uzh\_2@enu.kz (U.Z.T.); inerbaev\_tm@enu.kz (T.M.I.); satanova\_bm\_2@enu.kz (B.M.S.)
  - <sup>2</sup> Vernadsky Institute of Geochemistry and Analytical Chemistry, Russian Academy of Science, 119991 Moscow, Russia
  - <sup>3</sup> Laboratory of Renewable Energy, National Laboratory Astana, Nazarbayev University, Astana 010000, Kazakhstan; mirat.karibayev@nu.edu.kz
  - <sup>4</sup> Institute of Solid State Physics, University of Latvia, Kengaraga 8, LV-1063 Riga, Latvia
- \* Correspondence: abuova\_fu@enu.kz (F.U.A.); popov@latnet.lv (A.I.P.)

## Abstract

Barium titanate (BaTiO<sub>3</sub>) has long been recognized as a promising photocatalyst for solar-driven water splitting due to its unique ferroelectric, piezoelectric, and electronic properties. This review provides a comprehensive analysis of atomistic simulation studies of BaTiO<sub>3</sub>, highlighting the role of density functional theory (DFT), ab initio molecular dynamics (MD), and classical all-atom MD in exploring its photocatalytic behavior, in line with various experimental findings. DFT studies have offered valuable insights into the electronic structure, density of state, optical properties, bandgap engineering, and other features of BaTiO<sub>3</sub>, while MD simulations have enabled dynamic understanding of water-splitting mechanisms at finite temperatures. Experimental studies demonstrate photocatalytic water decomposition and certain modifications, often accompanied by schematic diagrams illustrating the principles. This review discusses the impact of doping, surface modifications, and defect engineering on enhancing charge separation and reaction kinetics. Key findings from recent computational works are summarized, offering a deeper understanding of BaTiO<sub>3</sub>'s photocatalytic activity. This study underscores the significance of advanced multi-scale simulation techniques for optimizing BaTiO<sub>3</sub> for solar water splitting and provides perspectives on future research in developing high-performance photocatalytic materials.

**Keywords:** BaTiO<sub>3</sub>; doping; defect engineering; surface functionalization; atomistic study; photocatalytic water splitting



Academic Editors: Gilbert Fantozzi and Vincent Garnier

Received: 31 May 2025

Revised: 9 July 2025

Accepted: 1 August 2025

Published: 4 August 2025

**Citation:** Abuova, A.U.; Tolegen, U.Z.; Inerbaev, T.M.; Karibayev, M.; Satanova, B.M.; Abuova, F.U.; Popov, A.I. A Brief Review of Atomistic Studies on BaTiO<sub>3</sub> as a Photocatalyst for Solar Water Splitting. *Ceramics* **2025**, *8*, 100. <https://doi.org/10.3390/ceramics8030100>

**Copyright:** © 2025 by the authors. Licensee MDPI, Basel, Switzerland. This article is an open access article distributed under the terms and conditions of the Creative Commons Attribution (CC BY) license (<https://creativecommons.org/licenses/by/4.0/>).

## 1. Introduction

Green hydrogen, produced from renewable energy sources, is a promising alternative fuel that plays a key role in reducing carbon emissions and enabling a sustainable, carbon-free energy future, in line with the goals of the Paris Agreement [1–5]. Several key methods are employed to produce green hydrogen efficiently [6–10]. Among them, photocatalytic water splitting is a well-established technique that uses photocatalysts, typically semiconductor materials such as titanium dioxide (TiO<sub>2</sub>) or other metal oxides, to absorb sunlight and facilitate the decomposition of water into hydrogen and oxygen [11–16]. These photocatalysts enhance reaction efficiency by reducing activation energy and improving charge separation, making them a cost-effective and scalable option for hydrogen production.

### 1.1. Photocatalytic Water Splitting and Its Challenges

Figure 1 presents a schematic illustration of three distinct water-splitting methods: electrochemical, photoelectrochemical, and photocatalytic water splitting [17].

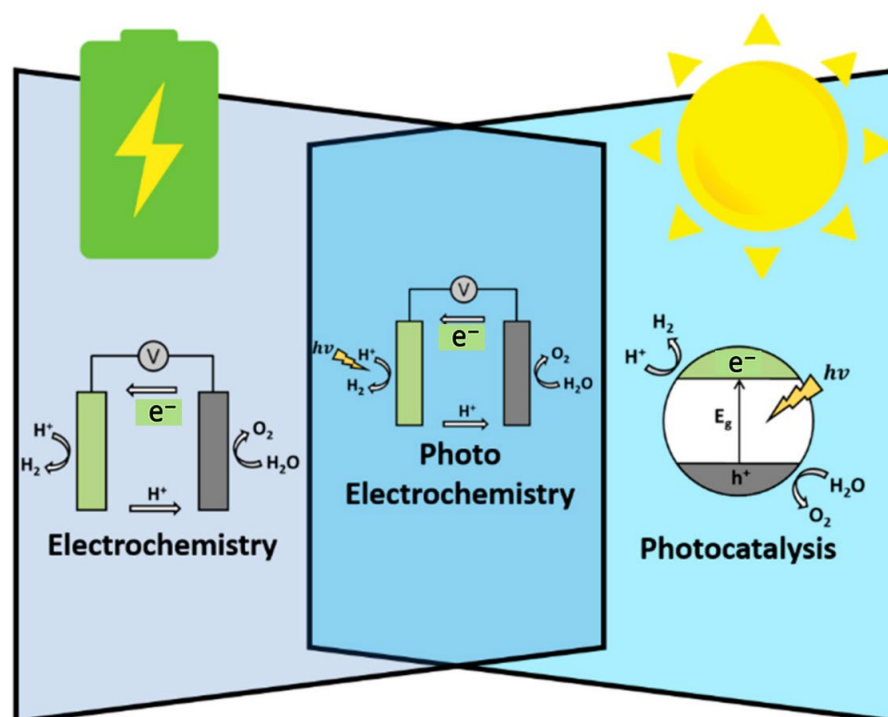


**Figure 1.** Schemes illustrate three major water splitting methods. Reprinted from [18].

In electrochemical water splitting, an external electrical source drives the water electrolysis process, typically using alkaline or proton exchange membrane electrolyzers. Photo electrochemical water splitting combines light absorption and electrochemical reactions in a single system, where a semiconductor photoelectrode absorbs solar energy to generate charge carriers for water splitting. In photocatalytic water splitting, a photocatalyst directly absorbs sunlight to excite electrons, facilitating overall water splitting without external bias, though its efficiency remains lower than the other methods [18–22]. Photocatalytic water splitting relies on semiconductor photocatalysts that absorb light and generate electron–hole pairs, which facilitate the redox reactions necessary for water decomposition.

Various photocatalysts have been explored for their efficiency and stability in hydrogen production [23–26]. Among these materials, perovskite-based photocatalysts have gained significant attention due to their excellent light absorption, charge separation efficiency, and structural tunability.

Despite its potential, photocatalytic water splitting faces several challenges that limit its efficiency and large-scale application, including (i) low efficiency—many photocatalytic materials exhibit low solar-to-hydrogen conversion efficiencies, requiring further improvements to enhance practical viability; (ii) limited light absorption—some photocatalysts, such as  $\text{TiO}_2$ , primarily absorb ultraviolet light, which constitutes only a small fraction of the solar spectrum, limiting their overall efficiency in utilizing sunlight for hydrogen production; (iii) charge recombination—the photogenerated electron–hole pairs often recombine before participating in the water-splitting reaction, significantly reducing the quantum yield and overall hydrogen generation rate; (iv) photocorrosion—certain semiconductor materials suffer from instability in aqueous solutions, undergoing degradation due to photocorrosion, which compromises their long-term performance; and (v) high overpotentials—the water-

splitting reaction requires overcoming high overpotentials, which slows down reaction kinetics and demands the use of additional co-catalysts to improve efficiency [26–30].

Addressing these challenges requires material modifications, such as doping, hetero-junction formation, and surface engineering, to improve light absorption, charge separation, and stability. In this regard, barium titanate ( $\text{BaTiO}_3$ ) has long been recognized as a promising photocatalyst for water splitting due to its strong ferroelectric properties, high chemical stability, and ability to enhance charge separation, thereby improving photocatalytic efficiency. This review focuses on the role of  $\text{BaTiO}_3$  in photocatalytic water splitting.  $\text{BaTiO}_3$ , with its inherent ferroelectric properties and chemical stability, has shown promise in overcoming some of these limitations, making it a compelling candidate for photocatalytic water splitting applications.

### *1.2. Background Information Regarding the Use of $\text{BaTiO}_3$ for Photocatalytic Water Splitting*

$\text{BaTiO}_3$  is a perovskite-type oxide semiconductor that has attracted significant attention for photocatalytic water splitting due to its unique combination of structural and electronic properties [31–38]. The following features are particularly important for its photocatalytic performance:

#### (i) Wide bandgap semiconductor

$\text{BaTiO}_3$  possesses a wide bandgap (typically 3.0–3.2 eV), enabling it to absorb ultraviolet light and generate the electron–hole pairs necessary for photocatalytic reactions. This bandgap is suitable for driving the redox reactions involved in water splitting, although it limits absorption to the ultraviolet region.

#### (ii) Ferroelectricity and spontaneous polarization

The ferroelectric nature of  $\text{BaTiO}_3$ , especially in its tetragonal phase, results in spontaneous polarization. This internal electric field promotes efficient separation of photogenerated electron–hole pairs, reducing recombination and enhancing photocatalytic efficiency.

#### (iii) High charge separation efficiency

The intrinsic polarization fields in  $\text{BaTiO}_3$  facilitate the migration of electrons and holes to the surface, where they participate in water oxidation and reduction reactions. This property is crucial for improving the quantum efficiency of photocatalytic water splitting.

#### (iv) Chemical stability

$\text{BaTiO}_3$  exhibits excellent chemical stability in aqueous environments and under irradiation, making it a durable photocatalyst for long-term water splitting applications.

#### (v) Favorable band edge positions

The conduction band (CB) and valence band (VB) edges of  $\text{BaTiO}_3$  are well-aligned with the redox potentials required for water splitting. The CB is sufficiently negative for hydrogen evolution, while the VB is positive enough for oxygen evolution.

#### (vi) Perovskite crystal structure

The perovskite structure of  $\text{BaTiO}_3$  allows for easy modification through doping or compositional tuning, which can further optimize its optical absorption, charge transport, and surface reactivity for photocatalytic applications.

Moreover,  $\text{BaTiO}_3$  undergoes several phase transitions (cubic, tetragonal, hexagonal, orthorhombic, and rhombohedral), depending on the temperature (Figure 2) [39–42]. At above  $\sim 120^\circ\text{C}$ , it adopts a cubic ( $\text{Pm}\bar{3}\text{m}$ ) perovskite structure, which is a paraelectric and centrosymmetric phase. Between  $\sim 5^\circ\text{C}$  and  $120^\circ\text{C}$ ,  $\text{BaTiO}_3$  transitions to a tetragonal ( $\text{P4mm}$ ) phase, a ferroelectric structure characterized by spontaneous polarization along the c-axis. As the temperature decreases further to between  $\sim -90^\circ\text{C}$  and  $5^\circ\text{C}$ , it takes on

an orthorhombic ( $Amm2$ ) phase, where the polarization shifts to a different direction compared to the tetragonal phase. Below  $\sim -90^\circ\text{C}$ , the material stabilizes in a rhombohedral ( $R3m$ ) phase, with spontaneous polarization along the  $[111]$  direction. Additionally,  $\text{BaTiO}_3$  can exist in a hexagonal ( $P63/mmc$ ) phase under high-pressure or non-equilibrium conditions, but this phase is not a stable ferroelectric structure under normal conditions [39–42]. Among all those phases, the tetragonal phase, stable at room temperature, is particularly beneficial for photocatalysis due to its strong ferroelectric polarization, which enhances charge separation [41–55].

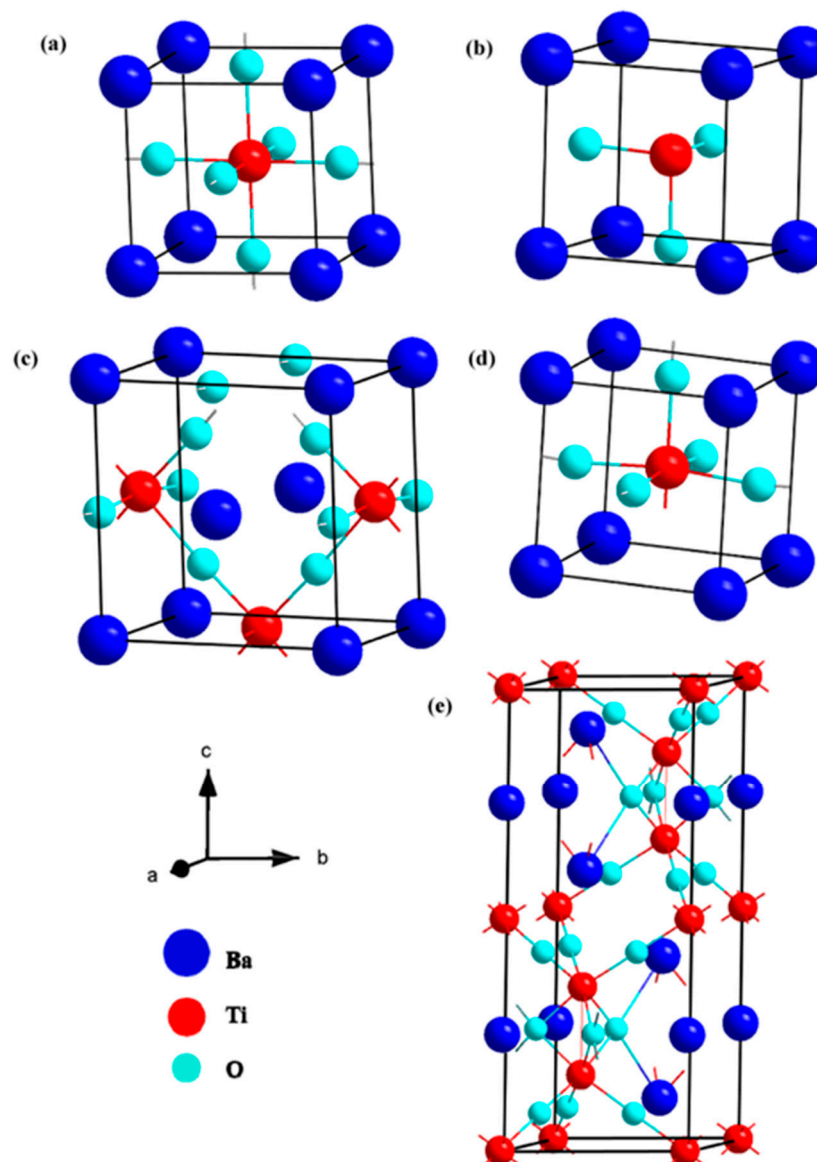


**Figure 2.** Atomistic representation of polymorphic  $\text{BaTiO}_3$  structures in different phases: (a) cubic, (b) rhombohedral, (c) orthorhombic, (d) tetragonal, and (e) hexagonal [40]. Reprinted with permission from [40]. Copyright 2023, Elsevier.

### 1.3. Atomistic Studies of the $\text{BaTiO}_3$ Photocatalyst

Atomistic simulations play a crucial role in understanding the photocatalytic properties of  $\text{BaTiO}_3$ , providing insights at multiple scales through density functional theory (DFT), ab initio molecular dynamics (MD), and classical all-atom MD simulations (Figure 3) [56,57].

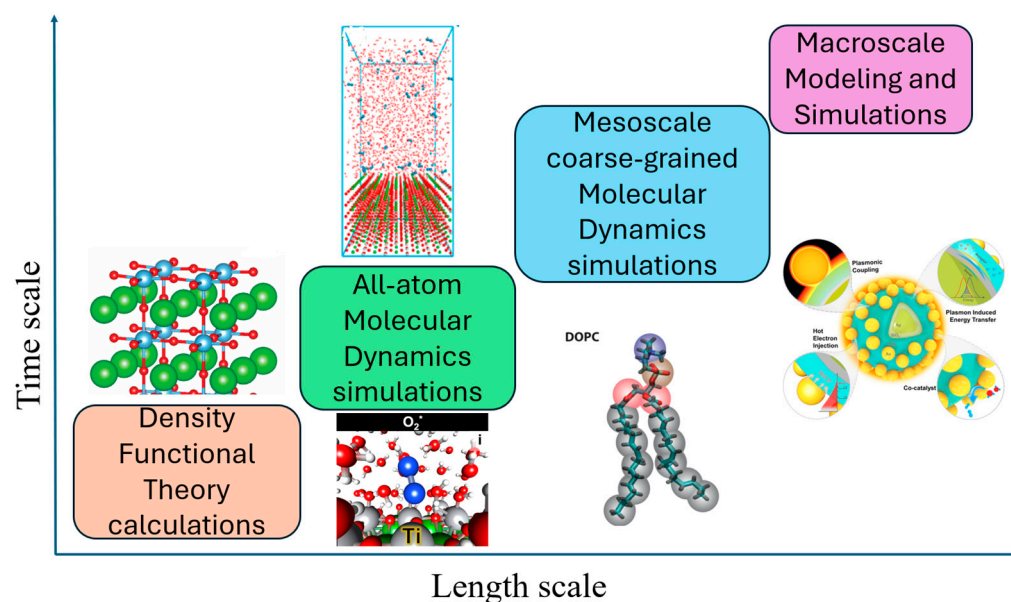


**Figure 3.** Illustration of different scales in computational engineering and material design. Reprinted from [58–62]. Copyright 2022, Elsevier [59]; copyright 2020, American Chemical Society [62].

DFT is widely utilized to accurately describe the electronic structure, phase stability, and defect behavior of  $\text{BaTiO}_3$  at the atomic level. It offers a cost-effective approach for investigating its ferroelectric and piezoelectric properties, which are crucial for its photocatalytic activity. Given that  $\text{BaTiO}_3$  undergoes multiple temperature-dependent phase transitions, DFT calculations help predict the relative stability of different polymorphs (cubic, tetragonal, hexagonal, orthorhombic, and rhombohedral) and their corresponding electronic and vibrational characteristics [63–65]. Moreover, DFT enables researchers to explore how external factors such as doping, strain, and electric fields modify the dielectric and electronic properties, making it invaluable for designing optimized photocatalytic materials.

Beyond structural analysis, DFT provides detailed insights into  $\text{BaTiO}_3$ 's electronic band structure and charge distribution, which are fundamental for photocatalysis. It aids in determining bandgap energies and evaluating charge transfer mechanisms, crucial for understanding photoinduced electron–hole separation in water splitting applications [64–69]. Additionally, defect formation energy calculations using DFT help assess the impact of oxygen vacancies, which play a critical role in tuning  $\text{BaTiO}_3$ 's optical and electronic response for enhanced photocatalytic performance.

To complement DFT, *ab initio* MD simulations provide a temperature-dependent and dynamic perspective on  $\text{BaTiO}_3$ 's behavior in aqueous environments or under irradiation conditions. *Ab initio* MD simulations help investigate surface interactions, the stability of adsorbed water molecules, and proton transfer mechanisms, which are essential for assessing  $\text{BaTiO}_3$ 's efficiency in photocatalytic water splitting [70–75]. Furthermore, *ab initio* MD simulations capture thermal fluctuations and structural rearrangements that static DFT calculations cannot fully describe, offering a more realistic depiction of  $\text{BaTiO}_3$ 's catalytic interface under operating conditions.

In addition, classical all-atom MD simulations provide large-scale insights into  $\text{BaTiO}_3$  nanoparticle stability, solvent interactions, and ion diffusion in solution-based photocatalytic processes. By employing force field-based molecular dynamics, these simulations help analyze solute–solvent interactions, charge carrier mobility, and ion adsorption at  $\text{BaTiO}_3$  surfaces [72–80]. This is particularly important for studying  $\text{BaTiO}_3$ -based hybrid photocatalysts, where interactions with co-catalysts, organic molecules, or electrolyte species significantly influence performance.



By integrating DFT calculations, ab initio MD simulations, and classical all-atom MD simulations, researchers can develop a multiscale understanding of BaTiO<sub>3</sub>'s photocatalytic properties. This combined approach not only aids in optimizing BaTiO<sub>3</sub>'s electronic and structural features, but also guides the design of novel photocatalytic systems for applications in hydrogen production.

#### 1.4. Outline of Our Review

This work presents a topical and characteristic analysis of recent computational studies of BaTiO<sub>3</sub>-based photocatalysts for solar water splitting. There were various works conducted for the atomistic study of advanced energy materials, including fuel cells, batteries, hydrogen fuel storage, carbon capture, drug design, and others [81–100]. Computational modeling and simulation techniques have become essential tools for examining the electronic structure, defect dynamics, charge transport, and reaction mechanisms of BaTiO<sub>3</sub> in photocatalytic applications.

Several computational approaches are commonly utilized in this field:

DFT calculations offer critical insights into the band structure, density of states, charge transfer processes, and defect formation energies [101–110] of BaTiO<sub>3</sub>. These studies assist in identifying optimal doping strategies to enhance photocatalytic performance.

Ab initio MD simulations are used to investigate the thermal stability, charge carrier dynamics, and interfacial interactions [111–120] of BaTiO<sub>3</sub> in aqueous environments under realistic conditions. Ab initio MD provides valuable data on the time evolution of atomic-scale processes.

Classical all-atom MD simulations help analyze the structural and solvation characteristics [121–125] of BaTiO<sub>3</sub> surfaces in water. These simulations offer insights into surface adsorption behavior, charge transfer dynamics, and the mechanisms underlying the water-splitting reaction.

To the best of our knowledge, comprehensive reviews integrating these atomistic simulation techniques for BaTiO<sub>3</sub> photocatalysis remain scarce. This work aims to introduce these computational methods and highlight their recent applications in studying BaTiO<sub>3</sub>-based solar-driven water splitting, alongside relevant experimental findings to provide a more comprehensive understanding.

The discussions in this paper are illustrative, and the examples provided are representative. We believe this review will serve as a valuable resource for researchers focused on designing and optimizing BaTiO<sub>3</sub> photocatalysts, encouraging the adoption of DFT, ab initio MD, and classical all-atom MD simulations to explore material properties across different length and time scales, in line with relevant experimental works.

## 2. Main Body

### 2.1. DFT Calculations

DFT calculations serve as a cornerstone for investigating the electronic structure and energetic properties of BaTiO<sub>3</sub>-based systems. By solving the Kohn–Sham equations under various approximations for exchange–correlation functionals, DFT provides detailed insights into charge distribution, density of states, and interaction energies at the atomic scale [126–138]. Despite its accuracy, conventional DFT calculations can be computationally demanding, especially for large systems or complex defect structures. To address this, hybrid functionals and dispersion corrections are often incorporated to enhance accuracy, while computational efficiency is improved through localized basis sets and advanced numerical techniques. In this regard, a series of DFT studies in the field of photocatalytic water splitting for BaTiO<sub>3</sub>-based systems is reviewed in the following paragraphs and in Table 1.

**Table 1.** Recently performed DFT calculation details and main findings.

Designed Systems	Methods	Main Findings
TiO <sub>2</sub> , TiO <sub>2</sub> /BaTiO <sub>3</sub> , TiO <sub>2</sub> @BaTiO <sub>3</sub> /CdS [139]	<p>DFT calculations using Vienna Ab initio Simulation Package (VASP) with Generalized Gradient Approximation-Perdew Burke Ernzerhof (GGA-PBE) functional.</p> <p>Projector-augmented wave (PAW) method for ion–electron interactions (cutoff energy: 400 eV).</p> <p>DFT + Hubbard U correction (DFT + U) approach for d-electron correlation correction.</p> <p>Finite-Difference Time-Domain (FDTD) method for electric field distribution simulations.</p>	<p>Calculated bandgap of TiO<sub>2</sub>: 3.22 eV.</p> <p>CB primarily composed of O(p) orbitals.</p> <p>VB primarily composed of Ti(d) orbitals.</p> <p>Photogenerated charge likely accumulates in these orbitals.</p> <p>After combining with BaTiO<sub>3</sub>, CB and VB compositions remain similar to TiO<sub>2</sub>.</p> <p>Calculated bandgap decreases.</p> <p>Adding CdS clusters to TiO<sub>2</sub>/BaTiO<sub>3</sub> caused slight crystal distortion in BaTiO<sub>3</sub>, potentially inducing spontaneous polarization.</p> <p>Density of states at CB and VB formed by S(p), Ba(d), and Cd(d) orbitals.</p> <p>Bandgap further decreased.</p> <p>However, the authors noted that this significant reduction in bandgap contradicts experimental results due to known limitations of standard DFT.</p> <p>TiO<sub>2</sub>/BaTiO<sub>3</sub>/CdS nanosheet exhibits an intrinsic electric field, facilitating charge separation and diffusion to the surface.</p>
Wheat-heading BaTiO <sub>3</sub> , wheat-heading BaTiO <sub>3</sub> -oxygen vacancy [140]	<p>DFT calculations using Materials Studio 2017, with GGA-PBE functional.</p> <p>Plane wave cutoff energy: 400 eV.</p> <p>K-point mesh: 3 × 3 × 3.</p> <p>Maximum force tolerance: 0.05 eV/Å.</p> <p>Cleaved along [001] direction and vacuum thickness of 10 Å in z-direction.</p>	<p>Bandgap for wheat-heading BaTiO<sub>3</sub>: 3.05 eV.</p> <p>CB mainly composed of Ti 3d and O 2p orbitals.</p> <p>VB dominated by O 2p orbitals.</p> <p>Charge transfer from O 2p to Ti 3d.</p> <p>After oxygen vacancy, bandgap reduced to 2.71 eV. VB remains dominated by O 2p orbitals.</p> <p>CB contributions shift to O 2p, Ba 3d, and Ti 3d.</p> <p>Enhanced charge transfer between Ti and O vacancy.</p> <p>Higher charge density improves piezo-photocatalytic performance.</p>
Pure BaTiO <sub>3</sub> , non-metal-doped BaTiO <sub>3</sub> (X@O or X@Ti, X = C, Si, N, P, S, Se, F, Cl, Br, I) [141]	<p>Spin-polarized DFT calculations using VASP with GGA-PBE functional.</p> <p>PAW method for core electrons.</p> <p>Plane-wave cutoff energy: 400 eV.</p> <p>9 × 9 × 9 Monkhorst–Pack k-point mesh.</p> <p>Fully optimized cubic BaTiO<sub>3</sub> unit cell with a lattice parameter of 4.004 Å.</p> <p>Geometry convergence criterion: forces &lt; 0.01 eV/Å.</p> <p>Hybrid functional (HSE06) for electronic structure calculations with Hartree–Fock (HF) exchange fraction (α) = 0.32.</p> <p>Substituting O or Ti with non-metal dopants at a doping concentration of 2.5 at.%.</p>	<p>Structural and electronic properties of BaTiO<sub>3</sub> were well reproduced.</p> <p>Bandgap improved with HSE06 functional, aligning with experimental values.</p> <p>Basis for further doping studies to enhance photocatalytic properties.</p> <p>F- and N-doped BaTiO<sub>3</sub> (X@O) and Si-doped BaTiO<sub>3</sub> (X@Ti) showed negative formation energy, indicating thermodynamic stability.</p> <p>Stability of doping systems depends on ionic radius and electronegativity of dopants relative to O or Ti.</p> <p>C-, S-, Se-, and I-doped BaTiO<sub>3</sub> (X@O) extended the absorption edge into the visible light region, enhancing photocatalytic water splitting capabilities.</p> <p>S- and Se-doped BaTiO<sub>3</sub> (X@Ti) exhibited potential for water splitting under visible light.</p> <p>Doping-induced modifications improved both photo-oxidation and photo-reduction properties of BaTiO<sub>3</sub>.</p>
Pure BaTiO <sub>3</sub> , La-doped BaTiO <sub>3</sub> [142]	<p>Materials Studio DFT with GGA-PBE functional.</p> <p>Birch–Murnaghan equation of state for lattice optimization.</p> <p>Cut-off energy: 340 eV.</p>	<p>BaTiO<sub>3</sub> exists in a cubic structure (Pm3m) with Ba at corners, Ti at the body center, and O at face centers.</p> <p>The calculated lattice constant is 4.034 Å, closely matching experimental values.</p> <p>Optical properties such as dielectric function, absorption, and refractive index are analyzed.</p> <p>La doping at Ba sites reduces the lattice parameter (a = 3.971 Å) and unit cell volume.</p> <p>Reduced bandgap enhances conductivity by facilitating electron–hole recombination.</p> <p>The La-5d states contribute significantly to the conduction band.</p> <p>Optical properties, including dielectric function, absorption, and refractive index, are modified.</p>

Table 1. Cont.

Designed Systems	Methods	Main Findings
BaTiO <sub>3</sub> with Ba and Ti vacancy [143]	Modeled using Materials Studio.	<p>Lattice distortion occurs due to Ba and Ti vacancies, affecting oxygen coordination and Coulomb repulsion. Oxygen vacancies are necessary for charge conservation in the system.</p> <p>Lattice expansion and distortion due to Ti and O vacancies are significantly higher than those caused by Ba and O vacancies. Charge density changes:</p> <ul style="list-style-type: none"> <li>Ba and O vacancies decrease charge density in specific regions of the unit cell.</li> <li>Ti vacancy increases and homogenizes charge density at the vacancy position.</li> </ul> <p>Lattice deformation leads to internal atomic shifts, with Ti atoms moving away from symmetry centers.</p>
	Optimized structure using VASP.	
	First-principles calculations based on DFT framework.	
	2 × 2 × 2 crystal structure containing 8 Ba, 24 O, and 8 Ti atoms.	
	PAW and PBE methods used for structure optimization and charge density calculations.	
Pure BaTiO <sub>3</sub> , Mo-doped BaTiO <sub>3</sub> (2.5 at%) [144]	First-principles calculations using DFT with the supercell approach, performed using VASP.	<p>The calculated bandgap of pure BaTiO<sub>3</sub> is 1.56 eV, which is underestimated due to DFT limitations.</p> <p>Charge-density analysis confirms covalent Ti–O bonding. Mo doping narrows the bandgap to 1.27 eV due to impurity levels formed by Ti 3d and Mo 3d interactions, and DFT limitations.</p> <p>Mo–O bonding results in a more uniform charge distribution than pure BaTiO<sub>3</sub>.</p>
	Functional: GGA for the PAW method.	
	Structural model: cubic 1×1×1 BaTiO <sub>3</sub> unit cell.	
	Plane-wave energy cutoff: 500 eV.	
	K-point sampling: Monkhorst–Pack grid of 7 × 7 × 7.	
Pure BaTiO <sub>3</sub> , Cs-doped BaTiO <sub>3</sub> (0.13%, 0.26%, 0.39%) [145]	Geometry optimization and property investigation with GGA-PBE exchange correlation functional with DFT + U correction (U = 4 for Ti-d orbital).	<p>For pure BaTiO<sub>3</sub>.</p> <p>Total density of state maximum peak at 4.29 eV (6.58 value), with other peaks at 1.79 eV and 0.95 eV.</p> <p>Phonon spectra show no imaginary frequencies, confirming stability.</p> <p>For Cs-doped BaTiO<sub>3</sub> (0.13%, 0.26%, 0.39%).</p> <p>Bandgap converts from indirect to direct upon Cs doping. Total density of state of 0.13% Cs-doped BaTiO<sub>3</sub> shows enhanced peaks, with a maximum peak at 0.77 eV (57.46 value). New peaks in total density of state appear at 3.43, 2.37, 2.40, 3.36, and 4.47 eV.</p> <p>Phonon spectra confirm stability for 0.13% Cs-doped BaTiO<sub>3</sub> (no imaginary frequencies detected).</p>
	Vanderbilt-type ultrasoft pseudopotentials for electron–ion interactions.	
	Pulay density mixing scheme applied.	
	Monkhorst–Pack method for k-point sampling (6 × 6 × 6 k-points mesh).	
	Energy cutoff = 630 eV.	
	Total energy difference per atom: 2 × 10 <sup>5</sup> eV.	
	Max ionic displacement: 2 × 10 <sup>3</sup> Å.	
BaTiO <sub>3</sub> (111) surfaces with different terminations [146]	Cubic phase (Pm3m, 221) chosen.	<p>Surface energy and stability.</p> <p>BaO<sub>2</sub> and O terminations have the lowest cleavage energies, making them the most thermodynamically stable.</p> <p>Removal of oxygen, Ti, or Ba reduces cleavage energy, stabilizing polar surfaces.</p> <p>Excess Ba (BaO + O<sub>2</sub>) or oxygen (Ba + O<sub>3</sub>) leads to instability with higher cleavage energies.</p> <p>Phase diagram analysis.</p> <p>BaO<sub>2</sub> and O terminations dominate under wide O- and Ba-rich conditions.</p> <p>Stoichiometric BaO<sub>3</sub> and Ti terminations are stable only in limited conditions.</p> <p>Results from O-Ti phase diagram match O-Ba phase diagram, confirming BaO<sub>2</sub> and O as the most stable.</p> <p>Charge compensation mechanism.</p> <p>Bader charge analysis shows charge redistribution in surface layers to compensate dipole moments.</p>
	DFT calculations using VASP.	
	PAW method for core electrons.	
	Plane-wave basis with 400 eV cutoff.	
	DFT + U approach with PBE functional (U <sub>eff</sub> = 4.0 eV for Ti 3d).	
	Considered stoichiometric (BaO <sub>3</sub> , Ti) and non-stoichiometric (BaO <sub>2</sub> , BaO, Ba, O <sub>3</sub> , O <sub>2</sub> , O) terminations.	



Table 1. Cont.

Designed Systems	Methods	Main Findings
BaTiO <sub>3</sub> doped with chalcogens (S, Se, Te) at different concentrations [147]	DFT calculations using WIEN2K package with FP-LAPW method and LDA + mBJ exchange-correlation potential. Calculation of $\epsilon(\omega) = \epsilon_1(\omega) + i\epsilon_2(\omega)$ .	BaTiO <sub>3</sub> has a cubic Pm3m structure. Lattice constant ( $a_0 = 3.9412 \text{ \AA}$ ) agrees with experimental ( $4.0000 \text{ \AA}$ ) and theoretical values. The forbidden bandgap decreases with increasing chalcogen concentration due to electronegativity differences. Doping reduces the bandgap significantly. Strong hybridization occurs between O 2p and chalcogen p orbitals.
Pressed BaTiO <sub>3</sub> (2.3% axial compressive strain), BaTiO <sub>3</sub> under triaxial compressive strain [148]	Ab initio calculations based on DFT. Exchange correlation potential: local density approximation (LDA). Brillouin zone integration: $6 \times 6 \times 6$ k-points for electronic and optical properties, $10 \times 10 \times 10$ for thermoelectric properties. Structural optimization: comparison with experimental and theoretical results.	Lattice constant reduced to $a_p = 3.8505 \text{ \AA}$ . Pressed BaTiO <sub>3</sub> exhibits a direct bandgap at the $\Gamma$ point, unlike pure BaTiO <sub>3</sub> , which has an indirect bandgap. Further bandgap reduction compared to non-pressed doped structures. Pressed BaTiO <sub>3</sub> exhibits slightly higher optical property peaks in $\epsilon_1(\omega)$ and $\epsilon_2(\omega)$ compared to pure BaTiO <sub>3</sub> . Electronic properties: Pure BaTiO <sub>3</sub> is a semiconductor with an indirect bandgap. Under $\xi = 2.3\%$ compressive strain, BaTiO <sub>3</sub> transitions to a direct bandgap semiconductor, improving potential for photovoltaic applications. Density of states analysis confirms VB is mainly O 2p, while CB is Ti 3d. Bandgap increases with strain, indicating possible piezoelectric properties.
BaTiO <sub>3</sub> (001) surfaces doped with metal and non-metal elements [149]	DFT calculations using VASP, PBE functional under GGA, and HSE06 hybrid functional. Plane-wave cutoff energy: 400 eV. K-point mesh: $9 \times 9 \times 9$ for bulk optimization and $3 \times 3 \times 1$ for surface calculations.	The tetragonal BaTiO <sub>3</sub> unit cell was fully optimized, with lattice parameters $a = b = 3.992 \text{ \AA}$ , $c = 4.056 \text{ \AA}$ , matching experimental and theoretical results. BaTiO <sub>3</sub> (001) surface modeled with TiO <sub>2</sub> - and BaO- terminations. Symmetric slabs (odd atomic layers) were adopted due to the absence of macroscopic dipole moments. Co-doped systems (M + X) are more stable when M and X are adjacent due to M-X bond formation. Formation energies indicate that O substitution by C or N is easier under Ti-rich conditions, while Ti substitution by metal dopants is favored under O-rich conditions. Binding energy calculations show that co-doped systems are more stable than mono-doped systems. The computed bandgap of bulk BaTiO <sub>3</sub> is 3.03 eV, while the pure BaTiO <sub>3</sub> (001) surface has a bandgap of 1.42 eV. Passivated co-doping (e.g., V + N, Nb + N, Ta + N) introduces charge compensation, eliminating mid-gap states. The Ta + N co-doping system leads to the most significant bandgap narrowing (1.09 eV) due to the upshift of the valence band maximum.
BaTiO <sub>3</sub> polymorphs (cubic, rhombohedral, orthorhombic, tetragonal, hexagonal) [150]	First-principles calculations using DFT framework (GGA-PBE, LDA, and HSE06 functionals).	Optimized lattice parameters are consistent with theoretical and experimental results. Formation enthalpies indicate all phases are energetically stable, with the cubic phase being the most stable. Band structure analysis shows indirect bandgaps for four phases and a direct bandgap for the hexagonal phase. GGA-PBE and LDA underestimate bandgaps, while HSE06 gives values closer to experimental data. Higher electron mobility and conductivity inferred from band structure analysis. Density of states analysis confirms structural stability and electrical conductivity.

Table 1. Cont.

Designed Systems	Methods	Main Findings
Porous graphene with BaTiO <sub>3</sub> , [151]	Electronic structure and density of states calculations using Quantum Espresso with PBE pseudopotentials.  k-mesh: $9 \times 9 \times 1$ for self-consistent field (scf) and $18 \times 18 \times 1$ for non-self-consistent field calculations.  Energy cutoff: 90 Ry for wavefunctions, 740 Ry for charge density.	Redshift in absorption edges of porous graphene with BaTiO <sub>3</sub> compared to pure BaTiO <sub>3</sub> . Lower fluorescence intensity indicates reduced charge carrier recombination, enhancing photocatalytic efficiency. Electron migration from BaTiO <sub>3</sub> to porous graphene via Ba–C bond supports charge separation. Fully relaxed $5 \times 5 \times 1$ supercell of porous graphene with BaTiO <sub>3</sub> with a 12 Å vacuum to prevent interaction between composites. Estimated bandgap of 1.74 eV (indirect, R to $\Gamma$ ), lower due to DFT underestimation. Additional bandgaps observed: direct at $\Gamma$ , indirect from M to $\Gamma$ . BaTiO <sub>3</sub> : VB primarily from O 'p' states; CB dominated by Ti 'p' states with minor O 'p' contributions.
Ba <sub>1-x</sub> Ga <sub>x</sub> TiO <sub>3</sub> (x = 50%) [152]	DFT calculations.  Tetra-elastic package for elastic properties.  Ba <sub>1-x</sub> Ga <sub>x</sub> TiO <sub>3</sub> was studied using full-potential linearized augmented plane wave method.  A 2000 k-point mesh was used for Brillouin zone integration.  Band structure and density of states were analyzed for electronic properties.  Elastic coefficients were calculated using a Eulerian strain approach.  The unit cell structure was modeled with tetragonal symmetry.	Pristine BaTiO <sub>3</sub> exhibits an indirect bandgap of 2.65 eV. Partial density of states analysis shows significant contributions from O p, Ti d, and Ga p states. Dielectric constant ( $\epsilon_1(0)$ ) increased from 8.8 (pure) to 100 (Ga-doped). A peak in the imaginary dielectric function $\epsilon_2(\omega)$ at 3.9 eV corresponds to O p electron transitions to the conduction band. Ga doping shifts absorption peaks towards the visible and infrared regions, enhancing optical activity.
BaTiO <sub>3</sub> /NiFe heterojunctions [153]	First-principles DFT calculations within GGA using a PBE functional.  PAW potentials for ionic cores.  Plane-wave basis set with a 450 eV cutoff.	Formation of BaTiO <sub>3</sub> /NiFe heterojunctions increased Ni <sup>3+</sup> content (45% $\rightarrow$ 68% for NiFe, 61% $\rightarrow$ 83% for BaTiO <sub>3</sub> /NiFe) after oxygen evolution reaction test. Fe <sup>3+</sup> /Fe <sup>2+</sup> ratio increased slightly after oxygen evolution reaction test, improving oxygen evolution reaction electrocatalytic activity. Free energy calculation showed a lower rate-determining step energy for heterojunction. Charge density difference analysis showed electron transfer from NiFe to BaTiO <sub>3</sub> , improving oxygen evolution reaction activity.
BaTiO <sub>3</sub> [154]	DFT using VASP.  PBE exchange-correlation function.  PAW pseudopotentials.  Cutoff energy: 520 eV.  Monkhorst–Pack $2 \times 2 \times 1$ k-points for Brillouin zone sampling.	The bandgaps of synthesized materials (3.24 eV, 3.20 eV, and 3.13 eV) are close to theoretical values, confirming minimal influence from PtOx loading. Pt–O–Ti <sup>3+</sup> sites act as defect energy levels and oxidation sites. Charge density analysis revealed electron accumulation around PtOx and depletion around Ti atoms. Polarization studies showed improved current response for PtOx-loaded samples, confirming enhanced photocatalytic activity. Pt serves as an electron aggregation center, accelerating proton reduction for hydrogen production. Oxygen vacancies facilitate charge aggregation, and Ti <sup>3+</sup> defects enhance rapid electron transfer.
BaTiO <sub>3</sub> /SrTiO <sub>3</sub> [155]	First-principles calculations using DFT, VASP.  GGA with PBE functional.  Kinetic cutoff energy: 520 eV.  Brillouin zone sampling: $5 \times 5 \times 1$ .  External electrostatic field along [001] direction (E = 0.1 eV/Å).	The BaTiO <sub>3</sub> /SrTiO <sub>3</sub> heterojunction has a lower bandgap compared to individual SrTiO <sub>3</sub> and BaTiO <sub>3</sub> , promoting photocatalytic efficiency. Differential charge density analysis reveals efficient electron transfer from BaTiO <sub>3</sub> to SrTiO <sub>3</sub> at the heterostructure interface. Hydrogen adsorption Gibbs free energy shows SrTiO <sub>3</sub> (0.57 eV), BaTiO <sub>3</sub> (−1.01 eV), and BaTiO <sub>3</sub> /SrTiO <sub>3</sub> (−0.42 eV), indicating BaTiO <sub>3</sub> /SrTiO <sub>3</sub> has optimized adsorption–desorption balance.

Table 1. Cont.

Designed Systems	Methods	Main Findings
Zr + X co-doped BaTiO <sub>3</sub> systems [156]	<p>DFT calculations.</p> <p>Full-potential linearized augmented plane-wave.</p> <p><math>2 \times 2 \times 2</math> supercell approach for constructing doped and co-doped systems.</p> <p>K-mesh: <math>12 \times 12 \times 12</math> for bulk, <math>6 \times 6 \times 6</math> for supercell.</p>	<p>Structural and thermodynamic properties: The computed cohesive energies of S, Se, and Te match well with previous studies.</p> <p>Electronic properties: X-doped systems have valence band edges composed of O 2p states with contributions from X p states. Zr-doped system shows conduction band modifications due to Zr 4d states. Zr + X co-doping leads to a reduced bandgap, making it promising for visible light applications.</p>
Metal oxide/BaTiO <sub>3</sub> [157]	<p>DFT using Quantum Espresso.</p> <p>GGA for exchange-correlation functional.</p> <p>Plane wave basis (320 Ry cut-off) k-point meshes: <math>6 \times 6 \times 1</math> for integration, <math>12 \times 12 \times 1</math> for density of states.</p> <p>Marzari–Vanderbilt cold smearing (0.05 Ry).</p> <p>Charge carrier effective masses calculated from Bloch band curvature.</p>	<p>Structural properties: ZnO/BaTiO<sub>3</sub> shows a decrease in BaTiO<sub>3</sub> lattice vector c due to interface-induced tetragonality enhancement. Interface distances: ZnO/BaTiO<sub>3</sub> (2 Å), TiO<sub>2</sub>/BaTiO<sub>3</sub> and SnO<sub>2</sub>/BaTiO<sub>3</sub> (4 Å). ZnO mid-slab oxygen layers exhibit large displacements due to interface interactions. Lattice mismatch effects cause strain in BaTiO<sub>3</sub>, compressing c in ZnO/BaTiO<sub>3</sub>.</p> <p>Electronic properties: Bandgaps in bulk: BaTiO<sub>3</sub> (3.28 eV), ZnO (3.41 eV), TiO<sub>2</sub> (3.17 eV), SnO<sub>2</sub> (3.52 eV). Interface effects modify band structures, introducing metal-induced gap states in ZnO/BaTiO<sub>3</sub>.</p>
Rhombohedral BaTiO <sub>3</sub> surface, pure and Rh-doped [158]	<p>Ab initio plane-wave calculations using VASP with PAW formalism and PBE-GGA exchange-correlation functional.</p> <p>Monkhorst–Pack grid: <math>2 \times 2 \times 2</math> for bulk, <math>2 \times 2 \times 1</math> for slab.</p> <p>Cutoff energy: 520 eV.</p> <p>Convergence tolerance: <math>10^{-6}</math> eV.</p> <p>Slab models with seven alternating TiO<sub>2</sub>- and BaO-planes and 13 Å vacuum gap.</p> <p>Rh doping effects analyzed by replacing Ti with Rh and re-optimizing structures.</p>	<p>Rhombohedral BaTiO<sub>3</sub> is ferroelectric and stable below 90 °C. Structural calculations show good agreement with experimental and previous theoretical studies. Ti displacement (−0.0137 Å) and O displacement (0.0232 Å) along [111] in rhombohedral BaTiO<sub>3</sub>. Calculated Ba–O (2.87 Å) and Ti–O (1.89 Å) bond lengths match experimental data. Direct bandgap of 2.25 eV is consistent with previous theoretical studies, though underestimated by GGA-PBE. BaTiO<sub>3</sub> (001) surface (TiO<sub>2</sub>-terminated) is nonpolar with a vacuum gap of 13 Å in slab models. Rh doping (substituting Ti with Rh) slightly affects lattice structure; minimal bond length change observed. Effective charge of Rh (1.66 e) is lower than Ba (2.55 e). Rh doping reduces the bandgap from 1.45 eV to 0.67 eV and introduces an in-bandgap acceptor level (0.115 eV above Fermi level). Rh and O hybridized orbitals create defect states in the bandgap, influencing photocatalytic performance.</p>
BaTiO <sub>3</sub> /LaAlO <sub>3</sub> heterostructures [159]	<p>DFT calculations using Quantum Espresso.</p> <p>Norm-conserving pseudopotentials GGA-PBE functional for exchange-correlation.</p> <p>Monkhorst–Pack k-point grid (<math>10 \times 10 \times 1</math> for heterostructure, <math>12 \times 12 \times 1</math> for bulk).</p> <p>30 Å vacuum space with dipole correction DFT-D3(BJ) for van der Waals interactions.</p> <p>Plane-wave cutoff energy: 45 Ry.</p> <p>Slab model for surface and interface calculations.</p>	<p>Optimized lattice parameters of bulk LaAlO<sub>3</sub> (3.83 Å) and BaTiO<sub>3</sub> (3.97 Å) agree with experimental values. Small lattice mismatch (−3.16%) heterostructure allows epitaxial growth. Ab initio MD and phonon dispersion results confirm dynamic and thermal stability of BaTiO<sub>3</sub>/LaAlO<sub>3</sub>(001) heterostructures at 300 K. BaTiO<sub>3</sub>(001) surface has the lowest bandgap (3.44 eV), favoring higher photocatalytic performance. BaTiO<sub>3</sub>(011) and (111) surfaces show direct bandgap behavior (4.05 eV, 3.75 eV). Partial density of states analysis reveals that charge carrier separation efficiency is influenced by surface composition.</p>

Table 1. Cont.

Designed Systems	Methods	Main Findings
BaTiO <sub>3</sub> thin films with TiO <sub>2</sub> - and BaO-terminated slabs for electrocatalysis [160]	<p>Ab initio periodic DFT + U calculations using the Quantum Espresso package, with GGA + U approximation and ultrasoft pseudopotentials.</p> <p>U = 4 eV for Ti d states.</p> <p>Kinetic energy cutoff: 320 eV.</p> <p>K-point grids: 4 × 4 × 1.</p> <p>Slabs modeled with four BaO and four TiO<sub>2</sub> layers on Pt as an electron reservoir.</p>	<p>Polarization direction affects electronic structure: Upward polarization → Electron-rich surface (downward band bending, Ti d states near Fermi level). Downward polarization → Hole-doped surface (upward band bending, O p states near Fermi level).</p> <p>Surface energy calculations: TiO<sub>2</sub>-terminated slabs are the most stable.</p> <p>Hydrogen evolution reaction activity trends: Poled-up surfaces show smaller reaction barriers for hydrogen evolution reaction, making them more favorable. Only H adsorption on O site of poled-down surface is optimal.</p>
Up-poled and down-poled BiFeO <sub>3</sub> /BiVO <sub>4</sub> heterostructures [161]	<p>DFT calculations using CRYSTAL23 code with B3LYP functional, D3 dispersion corrections, and spin polarization.</p> <p>Slabs modeled in R3c space group with (110) surface exposed.</p>	<p>Up-poled BiFeO<sub>3</sub> surface: spontaneously dissociates water molecules, converting surface O to OH. Oxygen vacancies migrate to the surface under upward polarization, enhancing OH adsorption. Stronger interaction with water compared to down-poled BiFeO<sub>3</sub>, enhancing OW-C and OW-P peaks. Binds molecular oxygen more strongly, which may slow reaction rate.</p> <p>Down-poled BiFeO<sub>3</sub> surface: H<sup>+</sup> adsorption promotes surface OH<sup>−</sup> formation, enhancing OL-H peak. OL and OL-H peaks shift to higher binding energies due to ferroelectric polarization effects. Weaker interaction with water, dominated by physisorption, leading to weaker OW-C peak and stronger OW-P peak. More fluid interaction with water and easier oxygen desorption, improving reaction rate. pH significantly affects BiFeO<sub>3</sub>-water interactions due to availability of H<sup>+</sup>/OH<sup>−</sup>.</p>
Anionic mono- and co-doped BaTiO <sub>3</sub> [162]	<p>QuantumATK software package DFT with PBE-GGA.</p> <p>Norm-conserving PseudoDojo pseudopotential.</p> <p>Self-consistent field simulations, 10<sup>−8</sup> Ha tolerance.</p> <p>HSE06 hybrid density functional for electronic calculations.</p> <p>2 × 2 × 2 supercell approach with periodic boundary conditions.</p>	<p>Lattice constants of mono-doped and co-doped BaTiO<sub>3</sub> structures decrease due to incorporation of anionic elements. Formation energy calculations indicate anionic co-doping is more stable than mono-doping, especially in O-poor conditions. N-doping introduces asymmetrical density of state, leading to magnetic behavior (+1.0 μB). P-doping also induces magnetism (+1.0 μB) and localized states near the Fermi level. C-doping introduces two acceptor levels, with a strong magnetic moment (+2.002 μB). S-doping maintains valence electron count, interacting with Ti 3d states and resulting in a favorable bandgap (2.24 eV) for visible light absorption. Co-doped systems (e.g., N-N, C-S, N-P) exhibit lower formation energies than their mono-doped counterparts, making them more thermodynamically favorable. N–N co-doping is the most stable due to similar atomic radii and strong anionic interactions.</p>
Ir-doped BaTiO <sub>3</sub> [163]	<p>DFT calculations using VASP.</p> <p>PAW method, GGA with PBE functional.</p> <p>GGA + U method (U values: Ti = 4 eV, O = 8 eV, Ir = 2 eV).</p> <p>Self-consistent and non-self-consistent field calculations with Monkhorst–Pack k-point grids (3 × 3 × 3 and 7 × 7 × 7).</p> <p>Cutoff energy: 500 eV.</p>	<p>Ir doping at the Ti site in BaTiO<sub>3</sub> induces a transition from n-type to p-type conductivity. Density of state calculations reveal a substantial downward shift in the Fermi level (from 4.36 eV to 3.18 eV), confirming p-type behavior. Ir doping at the Ba site does not induce a similar Fermi-level shift. Density of states analysis indicates partially and fully occupied Ir 5d orbitals below and above the Fermi level. Charge neutrality is maintained by Ir<sup>3+</sup> to Ir<sup>4+</sup> transitions, contributing to hole formation and p-type behavior. Findings align with previous studies on Rh-doped SrTiO<sub>3</sub>. Ir-doped BaTiO<sub>3</sub> exhibits visible-light absorption, making it a promising material for optoelectronic and photocatalytic applications. Further investigations of solar hydrogen evolution activity are in progress.</p>

Table 1. Cont.

Designed Systems	Methods	Main Findings
Rh-doped BaTiO <sub>3</sub> (Case A: Rh at Ba and Ti sites) [164]	<p>First-principles DFT calculations using Quantum Espresso.</p> <p>LDA pseudopotential.</p> <p>Norm-conserving pseudopotential with valence electrons: 6s<sup>2</sup> (Ba), 3d<sup>2</sup>4s<sup>2</sup> (Ti), 2s<sup>2</sup>2p<sup>4</sup> (O).</p> <p>Plane wave cutoff: 120 Ry, charge density cutoff: 480 Ry.</p> <p>K-point mesh: 4 × 4 × 4, 8 × 8 × 8.</p> <p>Electronic structure along G-X-M-G-R-X path.</p>	<p>BaTiO<sub>3</sub> has a cubic perovskite structure.</p> <p>Direct bandgap of 1.929 eV at G point due to folding of R point onto G point in 2 × 2 × 2 supercell.</p> <p>Additional indirect bandgap transitions (R → G and M → G).</p> <p>Underestimation of bandgap in DFT due to derivative discontinuities.</p> <p>Valence band formed by O p-orbitals, conduction band formed by Ti d-orbitals.</p> <p>Ba atoms have an ionic nature and do not contribute significantly to partial density of states.</p> <p>Rh-doped BaTiO<sub>3</sub> (Case A: Rh at Ba and Ti sites).</p> <p>Acceptor level formed due to hybridization of Rh (Ba site) d-orbitals and O p-orbitals.</p> <p>Deep defect states observed in wavefunction analysis.</p> <p>Direct bandgap: 2.028 eV at G point.</p> <p>Indirect bandgap: 1.796 eV (X → G) due to defect band overlapping with valence band edge.</p> <p>Hybridization of O p-orbitals and Rh d-orbitals at defect band region.</p> <p>Rh-doped BaTiO<sub>3</sub> (Case C: Rh at Ba sites only).</p> <p>Valence band mainly from O p-orbitals, with hybridization with Rh d-orbitals.</p> <p>Minor Rh d-orbital contributions in conduction band.</p> <p>Single occupancy ensures continuous band structure, facilitating charge carrier migration.</p>
BaTiO <sub>3</sub> surfaces with different polarization states for hydrogen evolution reaction [165]	<p>First-principles calculations using VASP 5.4.4 with GGA-PBE functional and DFT-D3 dispersion correction.</p>	<p>The tetragonal phase of BaTiO<sub>3</sub> was used, as it is stable at room temperature where hydrogen evolution reaction occurs.</p> <p>GGA was chosen due to limitations of LDA for hydrogen-bonded ferroelectrics.</p> <p>Lattice constants were fixed to experimental values.</p> <p>Surface structure relaxation leads to rumpling, affecting adsorption behavior.</p> <p>For out-of-plane polarized BaTiO<sub>3</sub>, the most stable hydrogen adsorption site is the surface oxygen site. The surface titanium site is inactive for hydrogen evolution reaction.</p> <p>In-plane polarization states can be modulated via thin-film growth techniques and electrochemical poling.</p>
La-N/B co-doped BaTiO <sub>3</sub> [166]	<p>DFT computations using Material Studio.</p> <p>PBE exchange-correlation functional with GGA + U (U = 4.3 eV for Ti-3d, 8.1 eV for La-4f).</p> <p>Energy cutoff: 500 eV.</p> <p>K-point grid: 3 × 3 × 3.</p> <p>Ultra-soft pseudopotentials.</p> <p>Energy convergence: 1.0 × 10<sup>−5</sup> eV/atom.</p>	<p>La and N mono-doping effects:</p> <p>La substitution at the Ba site reduced the bandgap to 1.55 eV.</p> <p>La substitution at the Ti site caused a slight bandgap increase (+0.10 eV).</p> <p>Co-doping impact (La-N@B, 25%):</p> <p>Band edge positions were more favorable for photocatalytic water decomposition.</p> <p>Modulated electronic structure and optimized bandgap for improved absorption properties.</p> <p>Partial density of state and total density of state analysis revealed Ti-3d and O-2p as dominant contributors to the CB minimum and VB maximum.</p> <p>The cubic BaTiO<sub>3</sub> phase (Pm3m) was used as a structural model despite its high-temperature stability for computational feasibility.</p>
Pt-doped BaTiO <sub>3</sub> [167]	<p>First-principles calculations using the supercell method, DFT with GGA-PW91, PAW approach.</p> <p>Energy cutoff: 300 eV, Monkhorst–Pack k-mesh (4 × 4 × 4), Scissor operator (0.75 eV) applied</p>	<p>Optimized BaTiO<sub>3</sub> unit cell and constructed 2 × 2 × 2 supercell (40 atoms).</p> <p>Pt doping at Ba and Ti sites (0.125 ratio) slightly reduces stability but remains thermodynamically favorable.</p> <p>Strong hybridization between Pt-5d and O-2p states.</p> <p>Mulliken charge analysis shows increased charge redistribution around O atoms.</p> <p>Pt doping introduces ferromagnetism in BaTiO<sub>3</sub>.</p> <p>Charge density analysis confirms the ionic-covalent bonding nature.</p>



Table 1. Cont.

Designed Systems	Methods	Main Findings
BaTiO <sub>3</sub> /Cu <sub>2</sub> O heterojunction [168]	Quantum Espresso package DFT, GGA using PBE functional.	Band alignment and offsets were calculated using supercell periodic slab models.
	Ultrasoft pseudopotentials.	BaTiO <sub>3</sub> /Cu <sub>2</sub> O interface shows a staggered (Type-II) band alignment, which favors charge separation and enhances photoelectrochemical activity.
	Plane-wave basis set (30 Ry energy cutoff, 180 Ry charge density cutoff).	Band offset values were obtained by considering VB and CB discontinuities.
	Monkhorst–Pack mesh for Brillouin zone sampling.	Effective mass of electrons and holes was calculated, revealing that Cu <sub>2</sub> O has a lower electron effective mass, indicating higher carrier mobility.
	Structural optimization via Hellman–Feynman forces.	The interface has a built-in dipole due to electronic charge transfer, influencing potential shifts across the heterojunction.
Tetragonal BaTiO <sub>3</sub> with (001) TiO <sub>2</sub> - and BaO-terminated surfaces [58,136,169]	DFT calculations using HSE06 functional.	Modeled BaTiO <sub>3</sub> (001) surfaces with TiO <sub>2</sub> - and BaO-terminated slabs.
	Geometry optimization and substitution energy calculations.	Rh doping of Ba/Ti sites prevents dipole moments due to symmetry preservation.
	Density of states and optical absorption analysis.	BaO-terminated surfaces found to be unstable under operating conditions.
		Substitution of Ti <sup>4+</sup> with Rh <sup>4+</sup> slightly distorts the lattice, while Ba <sup>2+</sup> → Rh <sup>3+</sup> + OH <sup>−</sup> substitution leads to significant structural changes.
BaTiO <sub>3</sub> (001) surfaces, including perfect and oxygen-deficient (TiO <sub>2</sub> -terminated) surfaces [170]	DFT with DFT + U using the VASP.	Doping the TiO <sub>2</sub> -terminated surface with Rh <sup>4+</sup> introduces Rh-4d states in the bandgap, reducing its value.
		Optical absorption threshold shifts due to Rh <sup>4+</sup> doping, with density of state analysis confirming bandgap modifications.
		PBE + U(Ti,O) approach improves the accuracy of bandgap calculations and bond energy predictions compared to standard PBE and PBE + U(Ti).
		Oxygen vacancies introduce in-gap states with Ti 3d character, positioned ~1.0 eV above the VB maximum and ~0.8 eV below the CB minimum.

Yang et al. investigated the electronic properties and photocatalytic performance of TiO<sub>2</sub>, TiO<sub>2</sub>/BaTiO<sub>3</sub>, and TiO<sub>2</sub>/BaTiO<sub>3</sub>/cadmium sulfide (CdS) composites [139]. DFT calculations revealed that pure TiO<sub>2</sub> has a bandgap of 3.22 eV, with CB and VB primarily composed of O(p) and Ti(d) orbitals, respectively. After the incorporation of BaTiO<sub>3</sub>, the calculated bandgap decreased to 1.53 eV, while the CB and VB compositions remained largely unchanged. Further modification with CdS induced slight crystal distortion in BaTiO<sub>3</sub>, leading to spontaneous polarization and a further reduced DFT-calculated bandgap of 1.19 eV. However, the authors noted that this significant reduction is inconsistent with experimental observations and attributed the discrepancy to the well-known limitations of standard DFT methods. The internal electric field generated within the BaTiO<sub>3</sub> shell enhanced charge separation, contributing to improved photocatalytic hydrogen evolution. Among the tested systems, the TiO<sub>2</sub>/BaTiO<sub>3</sub>/CdS nanocomposite achieved the highest hydrogen evolution rate (13.22 mmol/g·h) and an extended charge carrier lifetime (0.42 ns), outperforming both individual materials and binary composites. This study underscores the promising role of ferroelectric photocatalysts in promoting efficient charge separation and enhancing overall photocatalytic activity.

A study by Cai et al. highlights the synergistic effect of oxygen vacancies and piezoelectric properties in enhancing the photocatalytic carbon dioxide (CO<sub>2</sub>) reduction performance [140] of BaTiO<sub>3</sub>. By introducing oxygen vacancies, the visible light absorption range was extended, and the density of active surface sites increased, significantly improving charge separation. The piezoelectric effect further facilitated electron–hole separation,

enhancing the photocatalytic efficiency. Among the synthesized  $\text{BaTiO}_3\text{-X}$  samples,  $\text{BaTiO}_3\text{-1.5}$  exhibited the highest carbon monoxide (CO) production, achieving  $6.41 \mu\text{mol}\cdot\text{g}^{-1}$  under light alone and  $9.17 \mu\text{mol}\cdot\text{g}^{-1}$  under light and ultrasound, outperforming pristine  $\text{BaTiO}_3$  by factors of 3.22 and 1.86, respectively. DFT calculations revealed that oxygen vacancies reduced the bandgap from 3.058 eV to 2.717 eV, improving charge transfer. These findings suggest that defect engineering, combined with piezoelectric effects, offers a promising strategy for optimizing  $\text{BaTiO}_3$ -based photocatalysts for  $\text{CO}_2$  conversion, with potential applications in sustainable energy solutions.

Wang et al. used first-principles DFT calculations to investigate how non-metal dopants ( $\text{X} = \text{C}, \text{Si}, \text{N}, \text{P}, \text{S}, \text{Se}, \text{F}, \text{Cl}, \text{Br}, \text{I}$ ) [141] affect the geometric and electronic structures (Figure 4), stability, and photocatalytic properties of  $\text{BaTiO}_3$ . They examined two doping scenarios: substitution at the oxygen site ( $\text{X@O}$ ) and the titanium site ( $\text{X@Ti}$ ). Their findings align with experimental data, particularly regarding bandgap narrowing in N-doped  $\text{BaTiO}_3$ . The preferred doping site depends on the dopant's ionic size and electronegativity.  $\text{C@O}$  and  $\text{I@O}$  doping extended absorption into the visible spectrum, enhancing photocatalytic efficiency, while S and Se doping at either site improved photo-oxidation and photo-reduction. F- and N-doped  $\text{BaTiO}_3$  ( $\text{X@O}$ ) and Si-doped  $\text{BaTiO}_3$  ( $\text{X@Ti}$ ) were thermodynamically favorable. The study supports previous theories, highlighting non-metal doping's role in modifying  $\text{BaTiO}_3$  for visible-light photocatalysis, with further experimental validation needed.

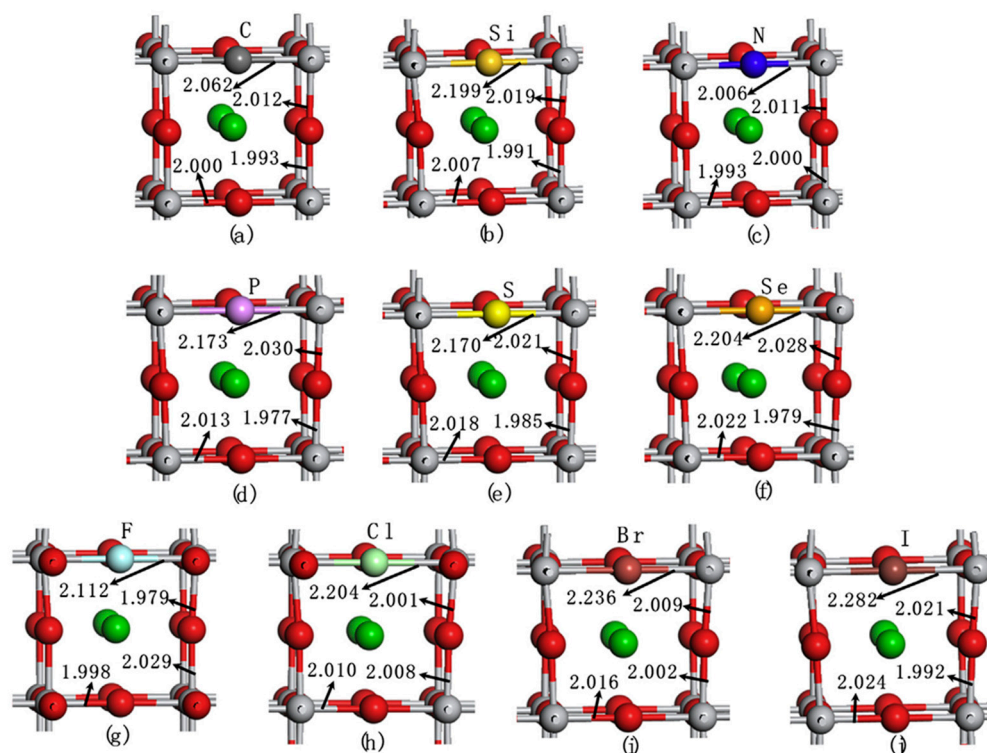


**Figure 4.** Optimized local structures of  $\text{BaTiO}_3$  configurations doped with (a) C, (b) Si, (c) N, (d) P, (e) S, (f) Se, (g) F, (h) Cl, (i) Br, and (j) I, where X substitutes O ( $\text{X@O}$ ). Reprinted with permission from [141]. Copyright 2019, Elsevier. Color key: Red, oxygen; green, titanium; grey, barium; dark grey, carbon; dark yellow, silicon; blue, nitrogen; violet, phosphorus; yellow, sulfur; orange, selenium; light grey, fluorine; light green, chlorine; dark red, bromine; brown, iodine.

Wang et al. demonstrated that non-metallic dopants, particularly nitrogen, are highly effective in narrowing the wide bandgap of  $\text{BaTiO}_3$ . Nitrogen doping introduces localized N 2p states that hybridize with O 2p orbitals, resulting in an upward shift of the valence

band and a reduced bandgap [141]. This modification enhances visible-light absorption without compromising the perovskite structure.

Rizwan et al. conducted a first-principles investigation of BaTiO<sub>3</sub> and La-doped BaTiO<sub>3</sub> using DFT with the GGA-PBE functional [142]. Their study examined structural, electronic, and optical properties before and after doping. The optimized lattice parameter for pure BaTiO<sub>3</sub> was 4.034 Å, closely matching experimental values, while La doping reduced it to 3.971 Å. The La-5d states played a crucial role in modifying the conduction band. Optical properties, including refractive index (2.598 for pure, 2.482 for doped) and absorption, were significantly affected by doping. The results demonstrated strong agreement with previous theoretical and experimental findings, validating the computational approach used in their study.

Xu et al. investigated the impact of the Ba/Ti ratio on the tetragonality of BaTiO<sub>3</sub> powder, challenging the conventional view that attributes tetragonality solely to grain size [143]. Their study demonstrated that, as the Ba/Ti ratio increased from 0.990 to 1.010, the particle size remained stable at approximately 200 nm. Tetragonality initially rose from 1.006 to a peak of 1.0092 at Ba/Ti = 1.000 before declining to 1.005. Using DFT, they analyzed electron density and lattice distortion, revealing that both Ba and Ti vacancies influence lattice deformation, with Ti vacancies causing more significant lattice expansion and reduced tetragonality (Figure 5). Their findings were supported by calculated charge density distributions, which showed that Ti vacancies increased charge uniformity. Using this optimized BaTiO<sub>3</sub> powder, they fabricated high-density ceramics and multilayer ceramic capacitors, highlighting the potential of Ba/Ti ratio control in developing advanced dielectric materials.

Xie et al. investigated the enhancement of photocatalytic hydrogen production through Mo doping of BaTiO<sub>3</sub> [144]. To improve light absorption, they synthesized Mo-doped BaTiO<sub>3</sub> via a solid-state reaction and modified the samples with 0.4 wt% Pt using a photoreduction method. Their findings revealed that Mo doping significantly narrows the bandgap, shifting the absorption edge into the visible-light region. Compared to pure BaTiO<sub>3</sub>, which has a hydrogen evolution rate of 35 mmol g<sup>-1</sup> h<sup>-1</sup>, Mo-doped BaTiO<sub>3</sub> (2 at%) achieved 63 mmol g<sup>-1</sup> h<sup>-1</sup>, nearly twice the efficiency. DFT calculations demonstrated that hybridization between the Ti 3d and Mo 3d orbitals led to a downward shift in the conduction band minimum, explaining the improved photocatalytic performance. Their study highlights how bandgap engineering via dopant selection enhances light absorption and provides valuable insights for designing high-performance metal-oxide photocatalysts for solar-driven hydrogen production.

Usman et al. conducted a theoretical investigation into the structural, electronic, and optical properties of pure and Cs-doped BaTiO<sub>3</sub> [145]. Their study employed the plane-wave pseudopotential method with the PBE exchange-correlation functional and the DFT + U approach to enhance electronic property accuracy. The calculated lattice parameter for pure BaTiO<sub>3</sub> was 4.034 Å, with an indirect bandgap of 2.513 eV, aligning well with prior research. Upon Cs doping (0.13%, 0.26%, and 0.39%), the bandgap transitioned to a direct type. Notably, 0.13% Cs-doped BaTiO<sub>3</sub> exhibited the highest absorption edge in the visible spectrum and the lowest energy loss, making it a promising candidate for photocatalytic water splitting. The introduction of Cs-3p states into the valence band enhanced photocatalytic activity, particularly in the visible range, improving BaTiO<sub>3</sub>'s potential for energy applications.

Chun et al. investigated the surface termination of single-crystal BaTiO<sub>3</sub> (111) using a combination of DFT and X-ray photoelectron spectroscopy [146]. Their study focused on the stability of stoichiometric (BaO<sub>3</sub> and Ti) and non-stoichiometric (BaO<sub>2</sub>, O, BaO, O<sub>2</sub>, Ba, and O<sub>3</sub>) terminations. DFT + U calculations revealed that BaO<sub>2</sub> and O terminations exhibit

the lowest cleavage and surface energies, making them the most stable under different conditions. The presence of  $\text{Ti}^{3+}$  states and oxygen defects was confirmed through X-ray photoelectron spectroscopy analysis of the O 1s and Ti 2p regions. Further DFT calculations of O 1s chemical shifts indicated that  $\text{OH}^*$  species preferentially adsorb on O-terminated surfaces, closely matching the experimental X-ray photoelectron spectroscopy data. Their findings suggest that  $\text{BaTiO}_3$  (111) favors an  $\text{OH}^*$ -covered O termination, with surface defects playing a crucial role in stabilizing the polar surface.

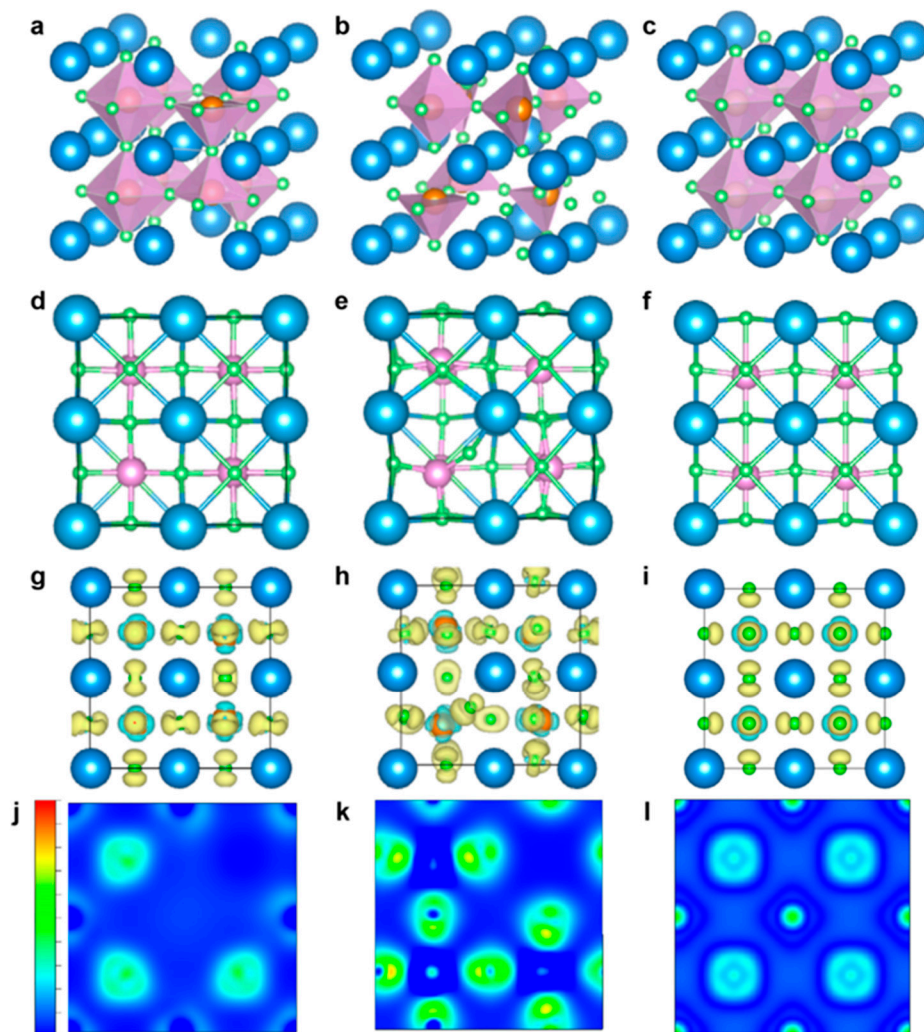


**Figure 5.**  $\text{BaTiO}_3$  lattice structure representations: (a) Ba vacancy, (b) Ti vacancy, and (c) ideal tetragonal  $\text{BaTiO}_3$ . (d) Ba and (e) Ti vacancies. (f) Front view of the tetragonal  $\text{BaTiO}_3$  model; front view of lattice structure simulation results. Charge density difference for (g) Ba vacancy and (h) Ti vacancy. (i) Ideal tetragonal  $\text{BaTiO}_3$  model viewed along the [001] zone axis. Charge density difference contour maps for (j) Ba vacancy and (k) Ti vacancy. (l) Ideal tetragonal  $\text{BaTiO}_3$  model. The intercepts are shown at 0 d, 0.25 d, and 0.5 d. Ba is represented in light blue, Ti in light orange, and O in light green. Reprinted with permission from [143]. Copyright 2024, Elsevier [143].

Dahbi et al. investigated the thermodynamic stability, electronic structures, and optical properties of pure and compressed  $\text{BaTiO}_3$  doped with varying concentrations of oxygen group elements (S, Se, and Te) using DFT [147]. Their findings revealed that substituting oxygen atoms with chalcogen elements significantly reduced the forbidden bandgap from 3.010 eV (for compressed  $\text{BaTiO}_3$ ) to 0.000 eV (for Te-doped  $\text{BaTiO}_3$ ), highlighting the crucial role of chalcogen impurities in modifying the electronic properties of  $\text{BaTiO}_3$ . Additionally, applying a 2.3% compressive strain, with or without chalcogen doping, transformed  $\text{BaTiO}_3$



from an indirect into a direct semiconductor. The calculated formation energy confirmed the thermodynamic stability of all studied compounds. Furthermore, doping altered the absorption behavior of BaTiO<sub>3</sub>, making it more suitable for optoelectronic applications due to the introduction of additional charge carriers into the system. These findings provide valuable insights into the potential applications of doped BaTiO<sub>3</sub> in electronic and optical devices.

Dahbi et al. investigated the impact of compressive strain on the electronic, optical, and thermoelectric properties of cubic and tetragonal phases of BaTiO<sub>3</sub> perovskite-type crystals using DFT [148]. Their study revealed that applying a compressive strain of 2.3% or higher transforms BaTiO<sub>3</sub> into a semiconductor with a direct bandgap, eliminating additional interactions in the conduction band, an important characteristic for photovoltaic applications. Additionally, the bandgap width increased with strain, highlighting the piezoelectric nature of BaTiO<sub>3</sub>. Optical analysis indicated that both pure and strained BaTiO<sub>3</sub> exhibit strong optical properties across the visible and ultraviolet spectra. Furthermore, compressive strain enhanced hole mobility, leading to improved thermal and electrical conductivity. A shift in absorption coefficient and optical conductivity peaks to higher ultraviolet energies further supported the piezoelectric behavior of BaTiO<sub>3</sub>. These findings underscore the potential of strained BaTiO<sub>3</sub> in electronic and energy-related applications.

Fo et al. conducted a DFT study to examine the effects of metal–non-metal co-doping on the stability, electronic properties, and photocatalytic activity of tetragonal BaTiO<sub>3</sub> (001) surfaces [149]. Their findings indicate that co-doped systems (M = V, Nb, Ta, Mo, W; X = N, C) are energetically stable, favoring formation in O-rich conditions. Most co-doped surfaces exhibit significantly reduced bandgaps, enhancing visible-light absorption. Additionally, co-doping improves water affinity and modifies active sites for the hydrogen evolution reaction and oxygen evolution reaction, with the O site and Ti site (adjacent to the metal dopant) acting as active centers (Figure 6). Notably, passivated co-doping lowers the hydrogen evolution reaction free energy barrier and reduces the oxygen evolution reaction overpotential compared to pristine BaTiO<sub>3</sub>. Among the studied systems, Ta + N, W + N, Mo + N, Mo + C, Mo + 2N, and W + 2N co-doped BaTiO<sub>3</sub> are highlighted as promising photocatalysts for overall water splitting. Co-doping strategies, such as the incorporation of both Ta and N, have shown superior performance compared to single-element doping. Metal dopants like Ta contribute additional donor states near the conduction band, while N modifies the valence band. This dual modification enables more precise control over the band structure, further narrowing the bandgap and improving charge carrier mobility. Importantly, co-doping helps to mitigate the formation of deep-level defects that can act as recombination centers, thus enhancing both the efficiency and stability of BaTiO<sub>3</sub>-based photocatalysts.

Chakraborty et al. investigated the structural, electronic, and optical properties of BaTiO<sub>3</sub> using DFT, highlighting its potential for photocatalytic applications, including water splitting and pollutant degradation [40]. Their study employed the hybrid HSE06 functional, yielding bandgap values of 3.254, 3.894, 3.694, 3.519, and 3.388 eV for cubic, rhombohedral, orthorhombic, tetragonal, and hexagonal BaTiO<sub>3</sub> polymorphs, respectively. Notably, this was the first DFT-based study to closely match experimental bandgap values. Electronic band structure analysis revealed that all polymorphs exhibit semiconducting behavior, with indirect bandgaps except for the hexagonal phase, which has a direct bandgap. The density of states analysis indicated significant hybridization between the O 2p and Ti 3d states. Optical studies confirmed strong absorption, low reflectivity, and optical anisotropy in the orthorhombic and tetragonal phases, making BaTiO<sub>3</sub> suitable for ultraviolet-based optical devices, waveguides, and dielectric applications [150]. The findings suggest that BaTiO<sub>3</sub>'s strong redox potential enhances its photocatalytic efficiency.



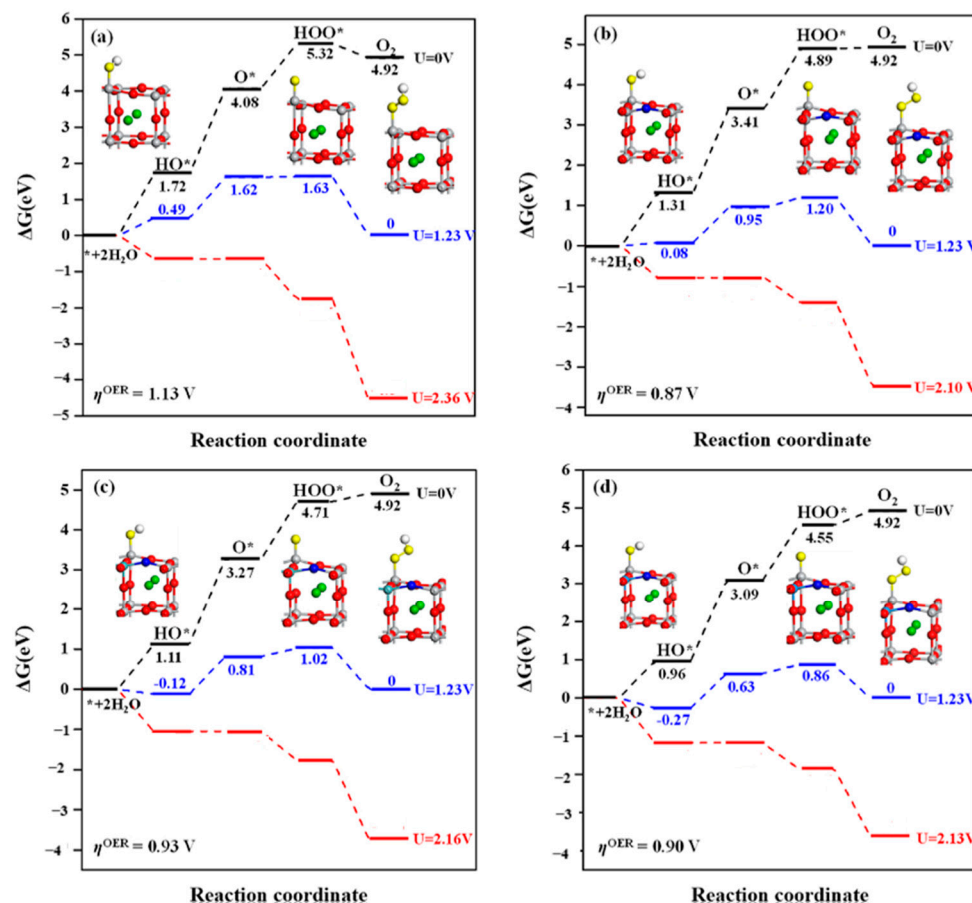


**Figure 6.** Free energy diagrams for the oxygen evolution reaction at the Ti site on BaTiO<sub>3</sub> (001) surfaces at pH = 0 and T = 298 K under different applied potentials: (a) pure, (b) (V + N)-co-doped, (c) (Nb + N)-co-doped, and (d) (Ta + N)-co-doped systems. Reprinted with permission from [149]. Copyright 2022, Elsevier [149]. Color key: Red, oxygen; green, titanium; grey, barium; dark grey, carbon; dark yellow, silicon; blue, nitrogen; violet, phosphorus; yellow, sulfur; orange, selenium; light grey, fluorine; light green, chlorine; dark red, bromine; brown, iodine.

Bhat et al. successfully synthesized a porous graphene–BaTiO<sub>3</sub> nanocomposite using a simple one-pot solvothermal method and investigated its photocatalytic efficiency in degrading methylene blue dye under visible light [151]. The combined experimental and theoretical analysis demonstrated enhanced photocatalytic performance, attributed to the formation of Ba–C bonds, which facilitated charge carrier transport and suppressed recombination. Additionally, the reduced bandgap due to hybridized states extended light absorption into the visible range, while the high surface area provided more active sites for methylene blue adsorption. The porous graphene–BaTiO<sub>3</sub> composite exhibited a threefold increase in photodegradation efficiency compared to pure BaTiO<sub>3</sub>, achieving 98.6% degradation within 80 min. Furthermore, it showed excellent cyclic stability, highlighting its potential as a durable photocatalyst for environmental remediation. This study serves as a valuable reference for designing porous graphene–BaTiO<sub>3</sub> nanocomposites, leveraging solar energy for sustainable pollutant degradation.

Bashir et al. conducted a theoretical investigation of Ga-modified BaTiO<sub>3</sub> perovskite ceramics (Ba<sub>1-x</sub>Ga<sub>x</sub>TiO<sub>3</sub>, x = 50%) using DFT calculations [152]. Their study explored the optoelectronic, elastic, and mechanical properties of both pure and Ga-doped BaTiO<sub>3</sub>. The results revealed that Ga substitution altered the electronic structure. Optical analysis indicated enhanced absorption in the ultraviolet region, lower reflectivity, and a static refractive index of 12.2. The modified BaTiO<sub>3</sub> exhibited higher ductility, anisotropy, and

bulk modulus (169.96 GPa) compared to the pure form. Additionally, prominent peaks in optical conductivity at 4.2 and 5.8 eV suggested potential applications in optoelectronics and spintronics. These findings highlight Ga-doped BaTiO<sub>3</sub> as a promising material for infrared detectors and antireflective coatings.

Wang et al. developed a flower-like core-shell heterostructured oxygen evolution reaction electrocatalyst by integrating tetragonal BaTiO<sub>3</sub> nanoparticles with NiFe-layered double hydroxide nanoarrays [153]. The study explored how the self-polarization effect of tetragonal BaTiO<sub>3</sub> influenced the oxygen evolution reaction performance of NiFe-layered double hydroxide nanoarray. In alkaline media (1.0 M KOH), the tetragonal BaTiO<sub>3</sub>/NiFe-layered double hydroxide nanoarray heterojunction exhibited a remarkably low overpotential of 186 mV at 10 mA/cm<sup>2</sup> and a Tafel slope of 38.3 mV dec<sup>-1</sup>, outperforming its individual components. DFT calculations demonstrated that electronic modulation between tetragonal BaTiO<sub>3</sub> and the NiFe-layered double hydroxide nanoarray reduced the bandgap, enhanced conductivity, and optimized the adsorption of oxygen-containing intermediates. The synergistic effects of these heterostructures resulted in superior electrocatalytic activity, offering insights into the rational design of efficient, noble metal-free oxygen evolution reaction electrocatalysts.

Chen et al. developed an amorphous PtOx-supported BaTiO<sub>3</sub> catalyst with oxygen vacancies (Figure 7) designed for efficiently producing hydrogen from wastewater while simultaneously degrading organic pollutants [154]. The catalyst features Pt-O-Ti<sup>3+</sup> charge separation sites, enhancing photocatalytic efficiency. PtOx-supported BaTiO<sub>3</sub> achieved a remarkable hydrogen generation rate of 1891  $\mu\text{mol}\cdot\text{g}^{-1}\cdot\text{h}^{-1}$  and exhibited a degradation rate constant of 0.0485 min<sup>-1</sup> for pefloxacin, significantly outperforming pristine BaTiO<sub>3</sub>. The introduction of PtOx facilitated oxygen vacancy formation, improving charge transfer and catalytic activity. This work highlights an effective strategy for developing bifunctional photocatalysts by engineering multiple active sites on a single catalyst for simultaneous redox reactions.

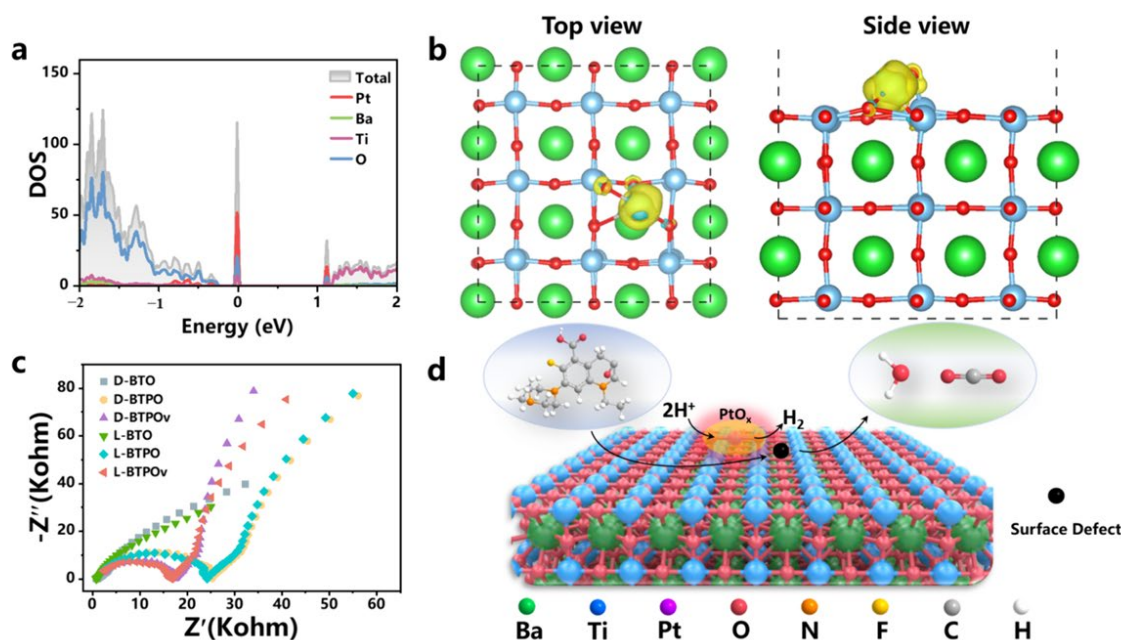


**Figure 7.** Interface reaction mechanism. (a) Density of state configuration for PtOx-supported BaTiO<sub>3</sub>, (b) top and side views of charge distribution in PtOx-supported BaTiO<sub>3</sub>, (c) Nyquist plots of BaTiO<sub>3</sub> and PtOx-supported BaTiO<sub>3</sub> under dark and light conditions, and (d) reaction mechanism diagram of PtOx-supported BaTiO<sub>3</sub>. Reprinted with permission from [154]. Copyright 2024, Elsevier [154].

Guo et al. explored the synergistic effect between piezoelectricity and photocatalysis to enhance hydrogen production via water splitting [155]. By combining experimental and theoretical analyses, they demonstrated that the inherent piezoelectric field in BaTiO<sub>3</sub> can reduce the bandgap of strontium titanate (SrTiO<sub>3</sub>)/BaTiO<sub>3</sub> heterojunction nanofibers, facilitating electron transfer through the Z-scheme mechanism. The incorporation of piezoelectric BaTiO<sub>3</sub> significantly boosted the hydrogen evolution rate of SrTiO<sub>3</sub>/BaTiO<sub>3</sub> nanofibers to 1950.2  $\mu\text{mol}\cdot\text{g}^{-1}\cdot\text{h}^{-1}$ , surpassing pure SrTiO<sub>3</sub> and BaTiO<sub>3</sub> by factors of 2.4 and 4.1, respectively. This rate also exceeded previously reported perovskite-based piezo-photocatalysts. Fabricated via electrospinning followed by thermal treatment, these nanofibers exhibited enhanced charge separation due to the piezoelectric field generated under ultrasonic vibrations. Their findings highlight the crucial role of piezoelectric-assisted photocatalysis in improving energy band alignment and efficiency, paving the way for advanced photocatalysts that address energy and environmental challenges in sustainable hydrogen production.

Zulfiqar et al. investigated the potential of chalcogen doping (X = S, Se, Te) of BaTiO<sub>3</sub> for visible light-driven photocatalysis in hydrogen production [156]. Using first-principles DFT calculations with a GGA functional, they assessed the structural, thermodynamic, electronic, and optical properties of X-doped BaTiO<sub>3</sub>. Their results indicated that incorporating a chalcogen atom at an oxygen site in BaTiO<sub>3</sub> is thermodynamically challenging due to significant differences in atomic radii and electronegativities. To enhance the synthesis feasibility, they proposed Zr co-doping at Ti-sites, which improved thermodynamic stability while maintaining bandgap reduction. Electronic structure calculations showed that Zr + X co-doping converted BaTiO<sub>3</sub> into a direct bandgap material with band edge positions favorable for overall water splitting. This study highlights the potential of Zr + X co-doped BaTiO<sub>3</sub> as an efficient photocatalyst for hydrogen evolution under both oxygen-rich and oxygen-poor conditions.

Kovač et al. investigated the role of transport layers in perovskite solar cells, focusing on their charge carrier extraction and transfer mechanisms [157]. Using ab initio calculations, they examined the interface properties of metal oxide/BaTiO<sub>3</sub> heterostructures, identifying key competing factors influencing charge dynamics. Their findings highlight the impact of bandgap character on charge carrier mobility, where a direct bandgap reduces electron–hole lifetime and diffusion length. Additionally, they explored the influence of electrostatic potential variations, which enhance charge transfer rates but are counteracted by unfavorable conduction band offsets. The study emphasizes the importance of interlayer morphology over intrinsic material properties, suggesting that optimizing atomic plane distances and atomic number distributions can improve charge transport efficiency.

Kaptagay et al. investigated the oxygen evolution reaction on a Rh-doped BaTiO<sub>3</sub> (001) surface using DFT calculations [158]. Their study assessed the Gibbs free energy changes for each reaction step and calculated the overpotential while considering solvation effects. The findings revealed that Rh doping significantly reduces the overpotential compared to the undoped BaTiO<sub>3</sub> surface, which exhibits low oxygen evolution reaction efficiency. This improvement is attributed to the oxidation state transition of Rh from 3+ to 4+ during water splitting, which enhances the charge transfer from surface oxygen ions. As a result, the binding energy between surface ions and adsorbates increases, weakening the adsorbate–adsorbate interactions and leading to a lower overpotential. The reduced overpotential on the Rh-modified TiO<sub>2</sub> surface confirms its enhanced catalytic activity in electrochemical water oxidation, aligning well with experimental results and previous studies. These insights highlight Rh doping as a promising strategy for improving oxygen evolution reaction efficiency.

Opoku et al. investigated the electronic structure, charge transfer, and photocatalytic properties of cubic lanthanum aluminate ( $\text{LaAlO}_3$ ) (001) modified with cubic  $\text{BaTiO}_3$  (001), (011), and (111) surfaces [159]. Their study aimed to understand how  $\text{LaAlO}_3$  can be activated under light irradiation through the incorporation of different  $\text{BaTiO}_3$  surfaces. The heterostructures demonstrated reduced bandgap energy, enhancing visible light absorption. Additionally,  $\text{BaTiO}_3/\text{LaAlO}_3(001)$  heterostructures exhibited a staggered type-II band alignment, which facilitated charge carrier separation and minimized recombination. The  $\text{BaTiO}_3(001)$  surface, in particular, enhanced photocatalytic activity due to its complex surface structure and active barium adsorption sites.  $\text{BaTiO}_3$  acted as a sensitizer, improving overall photoactivity. Their findings provide valuable insights into the preferential exposure of photocatalytic active surfaces, aiding in the design of advanced heterostructures for photocatalytic applications and offering a deeper understanding of photocatalytic mechanisms.

Abbasi et al. investigated the impact of ferroelectric polarization on the electronic structure and electrocatalytic activity of  $\text{BaTiO}_3$  thin films, particularly in the hydrogen evolution reaction [160]. Unlike previous studies focused on nanoparticle systems with complex interfaces, they used molecular beam epitaxy to grow epitaxial  $\text{BaTiO}_3$  films with atomically sharp interfaces. Their surface spectroscopy and ab initio DFT + U calculations revealed that upward polarization decreases the work function and lowers the hydrogen evolution reaction barrier, correlating with enhanced experimental activity. The study demonstrated that modulating polarization can dynamically switch between distinct electrocatalytic surfaces, altering charge transfer resistance and exchange current density. The findings highlight how ferroelectric layers can be used to control intermediate binding energies in electrochemical reactions, offering new avenues for nanoscale catalyst design by leveraging polarization-dependent surface properties beyond conventional catalytic descriptors.

Gunawan et al. investigated the role of ferroelectric polarization in enhancing photoelectrochemical performance, addressing challenges related to charge recombination and sluggish charge transfer kinetics [161]. They designed a heterostructure composed of multiferroic bismuth ferrite ( $\text{BiFeO}_3$ ) and photoactive bismuth vanadate ( $\text{BiVO}_4$ ) in a neutral pH electrolyte, demonstrating significant photocurrent improvements. Notably, both polarization states contributed to enhancement: the down-poled  $\text{BiFeO}_3/\text{BiVO}_4$  exhibited a 136% increase, while the up-poled configuration showed a 70% improvement at 1.23 V, surpassing previous reports. Extensive photoelectrochemical analysis, surface characterization, and DFT calculations revealed that the improvements were driven by band energy gradient modulation, band bending, and altered  $\text{BiFeO}_3$ /adsorbate interactions. The sol-gel synthesis method used is scalable and employs environmentally friendly materials, making this approach promising for next-generation dynamic photoelectrodes. Their findings advance the field of ferroelectric-based photoelectrochemical systems by enabling tunable charge dynamics and overcoming limitations of conventional semiconductor photoelectrodes.

Goumri-Said et al. conducted a comprehensive study on the electronic properties and optical absorption behavior of anion-anion co-doped  $\text{BaTiO}_3$  to design efficient photocatalysts for water redox reactions [162]. Using first-principles hybrid DFT calculations with the HSE06 functional, they analyzed the impact of double-hole doping on band structure modifications. Their findings revealed that the formation energy of mono- and co-doped configurations increased as the oxygen chemical potential decreased, with N-N co-doped  $\text{BaTiO}_3$  exhibiting the most favorable formation energy under O-poor conditions. All co-doping configurations resulted in bandgap reduction, enhancing visible light absorption and aligning band edge positions with water oxidation-reduction potentials. This study highlights the effectiveness of anionic co-doping in tuning wide-bandgap semiconductors,



demonstrating that such modifications can produce highly efficient photocatalysts for solar-driven water splitting.

Chandrappa et al. explored strategies to modify the electronic and optical properties of BaTiO<sub>3</sub> by introducing Ir doping at Ti sites [163]. While pristine BaTiO<sub>3</sub> typically exhibits strong n-type behavior and ultraviolet absorption ( $\lambda \leq 390$  nm), their study demonstrated a successful transition to p-type semiconducting behavior with extended visible-light absorption ( $\lambda \leq 600$  nm). Through a combination of advanced spectroscopy, microscopy, and computational electronic structure analysis, they elucidated the underlying mechanisms governing this transition. The redshift in optical absorption was attributed to the formation of Ir<sup>3+</sup>/Ir<sup>4+</sup> in-gap energy levels within the bandgap, facilitating optical transitions. Furthermore, the observed decrease in Ti<sup>3+</sup> donor levels and correlated oxygen vacancies played a crucial role in enabling the p-type behavior. These findings highlight the potential of Ir-doped BaTiO<sub>3</sub> as a promising visible light-absorbing semiconductor with significant applications in optoelectronics and solar fuel generation.

Bhat et al. investigated the potential of environmentally friendly BaTiO<sub>3</sub> as a photocatalyst, despite its initially wide bandgap, which limits efficiency [164]. They explored Rh doping to reduce the bandgap but avoided the formation of mid-gap recombination centers that typically hinder photocatalytic performance. Using first-principles DFT calculations, they determined that Rh occupying both Ba and Ti sites would simultaneously introduce detrimental acceptor states. To address this, they employed a hydrothermal synthesis method to direct Rh towards Ba sites, leading to donor Rh<sup>3+</sup> states that lowered the bandgap while maintaining high photocatalytic activity. Their experimental results confirmed an efficient 96% degradation of methylene blue dye within 120 min for a 0.5 Rh-doped sample. This study demonstrated a viable strategy to enhance BaTiO<sub>3</sub>'s photocatalytic efficiency and suggested that similar methods could be applied to other perovskite oxides for improved dye degradation.

Qiu et al. investigated the impact of switchable polarization in ferroelectric catalysts on the hydrogen evolution reaction, aiming to overcome the Sabatier limit faced by traditional catalysts [165]. Using BaTiO<sub>3</sub> as a model system, they demonstrated that hydrogen evolution reaction activity is tunable by controlling polarization states. First-principles calculations revealed that in-plane polarized BaTiO<sub>3</sub> enhances hydrogen evolution reaction performance compared to out-of-plane polarization, due to surface dipole–dipole interactions. Surface rumpling, influenced by polarization states, significantly affects surface oxygen reactivity, with an optimal 2p band center correlating with improved hydrogen evolution reaction activity. The study also established a link between hydrogen adsorption energy and polarization effects. Furthermore, a hydrogen evolution reaction catalytic cycle leveraging switchable polarization states was proposed, showing potential for enhanced catalytic efficiency. Their findings highlight the role of ferroelectric polarization control in designing high-performance electrocatalysts, providing insights into functional ferroelectric catalysis beyond hydrogen evolution reaction applications.

Wang et al. investigated the impact of co-doping rare earth elements on the electronic and photocatalytic properties of BaTiO<sub>3</sub> using first-principles calculations [166]. They examined BaTiO<sub>3</sub> supercell structures with La concentrations of 12.5% and 25%, focusing on doping at both Ba and Ti sites. Their analysis of band structure, density of states, and charge density difference revealed that co-doping 25% La at the Ti site significantly enhanced visible-light absorption and water-splitting performance. The introduction of La created intermediate energy levels within the bandgap, reducing the energy required for electronic transitions. Further, La-N co-doping at the Ti site effectively modified the band structure, improving photocatalytic efficiency. Optical property calculations confirmed an extended absorption edge, enhancing BaTiO<sub>3</sub>'s visible light response. Their findings



highlight La co-doping as a promising strategy for optimizing BaTiO<sub>3</sub>'s electronic structure and photocatalytic activity, making it a viable material for energy-related applications.

Saadon et al. investigated the structural, electronic, and optical properties of Pt-doped cubic BaTiO<sub>3</sub> perovskite using DFT calculations. By employing DFT calculation with the GGA, they examined the effects of substituting 0.125 Pt at Ba and Ti sites. Their findings showed that Pt doping reduced the bandgap and introduced Pt-5d states in the conduction band, significantly influencing electronic properties. Additionally, the optical absorption spectrum exhibited a red shift, extending into the visible range, making Pt-BaTiO<sub>3</sub> a promising material for optoelectronic applications. The negative formation energy confirmed the thermodynamic stability of the doped system. Mulliken charge analysis further revealed a shift from ionic to covalent bonding in Ba–Pt and Ti–Pt interactions. Future studies may explore the material's potential in photocatalysis and environmental applications [167].

Sharma et al. synthesized nanostructured BaTiO<sub>3</sub>/copper (I) oxide (Cu<sub>2</sub>O) heterojunction electrodes with varying Cu<sub>2</sub>O film thickness using spray deposition onto spin-coated BaTiO<sub>3</sub> thin films [168]. For the first time, first-principles DFT calculations were performed to determine band offsets and effective masses of charge carriers for bulk BaTiO<sub>3</sub> and Cu<sub>2</sub>O. The study revealed enhanced separation of photogenerated charge carriers at the BaTiO<sub>3</sub>/Cu<sub>2</sub>O interface. Experimental photoelectrochemical analysis confirmed these findings, showing a maximum photocurrent density of 1.44 mA/cm<sup>2</sup> at 0.95 V for a 442 nm thick heterojunction electrode. This structure exhibited superior charge transfer, reduced resistance, and improved light absorption compared to individual BaTiO<sub>3</sub> or Cu<sub>2</sub>O electrodes. The study demonstrated that BaTiO<sub>3</sub>/Cu<sub>2</sub>O heterojunctions improve water-splitting efficiency in photoelectrochemical cells, achieving a peak conversion efficiency of 0.66%. The theoretical results aligned well with the experimental data, providing insights into charge separation mechanisms.

Inerbaev et al. explored the potential of modified BaTiO<sub>3</sub>, a cost-effective perovskite oxide, as an efficient water oxidation electrocatalyst using first-principles calculations [58,136,169]. Their study demonstrated that Rh doping enhances BaTiO<sub>3</sub>'s light absorption capabilities while reducing the overpotential required for water oxidation. The TiO<sub>2</sub>-terminated BaTiO<sub>3</sub> (001) surface was identified as particularly promising for catalytic applications (Figure 8). Rh doping expanded the material's absorption spectrum to cover the entire visible range, with the aqueous environment playing a crucial role in modulating its solar radiation absorption. Upon Ti→Rh substitution, rhodium ions partially acquired electron density from surrounding oxygen atoms, stabilizing an intermediate oxidation state (3+ to 4+) during water oxidation. This interaction influenced the adsorption energies of reaction intermediates, effectively lowering the overpotential. The study concluded that Rh-modified BaTiO<sub>3</sub> surfaces exhibit significant potential as photoanodes in photoelectrochemical systems for water oxidation.

Inerbaev et al. also investigated the optical properties of tetragonal BaTiO<sub>3</sub> using DFT calculations, incorporating both static lattice calculations and ab initio MD simulations [135,169]. Their study, which applied GGA + U and hybrid functionals, revealed that atomic motion significantly lowers the optical absorption threshold. This reduction occurs due to thermal fluctuations enabling previously forbidden electronic transitions and shifting the energy levels of optical absorption, providing insights into the photoluminescence behavior of BaTiO<sub>3</sub> [169].

Tyminska et al. investigated the impact of oxygen vacancy on the oxygen evolution reaction at the TiO<sub>2</sub>-terminated (001) surface of cubic BaTiO<sub>3</sub> using spin-polarized DFT + U calculations and the standard four-step proton-coupled electron transfer mechanism [170]. Their study revealed that excess electrons from oxygen vacancy contribute to charge transfer

with intermediate adsorbates ( $\text{HO}^*$ ,  $\text{O}^*$ , and  $\text{HOO}^*$ ) or generate surface oxygen hole states. This charge transfer enhances the binding energies of these species in proportion to their electronegativity. Notably,  $\text{HO}^*$  and  $\text{O}^*$  are stabilized more strongly than  $\text{HOO}^*$ , leading to increased oxygen evolution reaction overpotential on the oxygen-deficient surface. This contradicts experimental findings that indicate enhanced efficiency of oxygen-deficient  $\text{BaTiO}_3$ , suggesting that a different mechanism or surface structure may be responsible under experimental conditions. Additionally, they identified novel  $\text{HO}^*$  and  $\text{O}^*$  adsorption structures that induce surface oxidation, attributed to the low work function of  $\text{Ti}-\text{O}-\text{Ti}$  moieties.

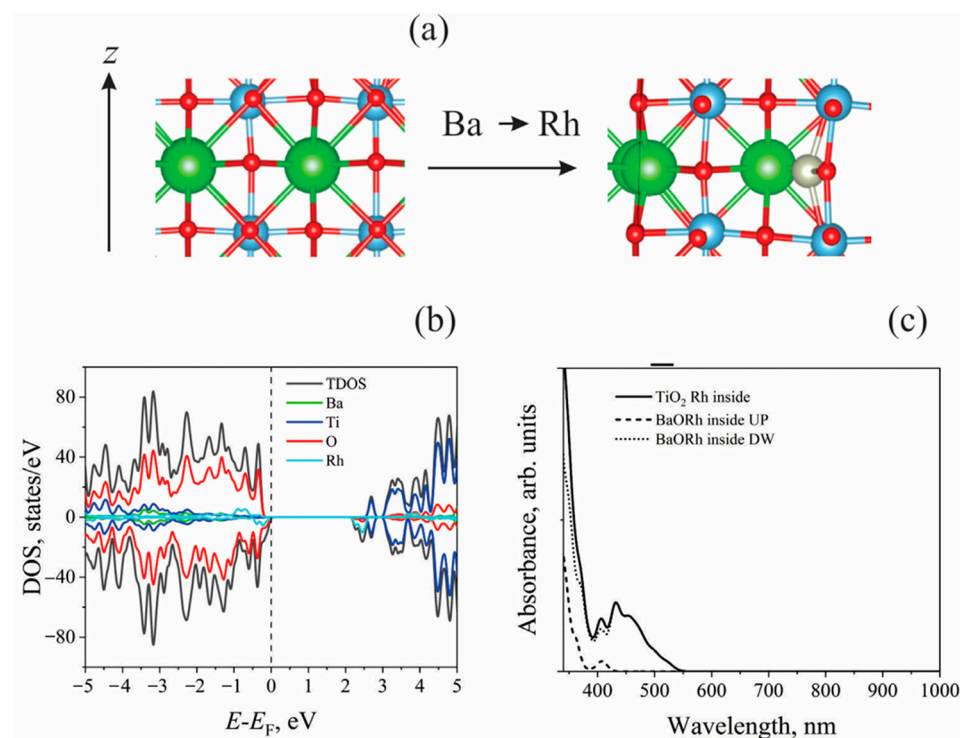


**Figure 8.** (a) Ion arrangement changes in the slab after Ba substitution with Rh, (b) electronic DOS of the relaxed slab, and (c) optical absorption spectrum of the investigated model. Dashed and dotted lines indicate optical absorption for spin-up and spin-down states, respectively, while the solid line represents total absorption. Reprinted from [58].

## 2.2. Ab Initio MD Simulations

Atomistic simulations play a crucial role in understanding the fundamental mechanisms governing photocatalytic activity in  $\text{BaTiO}_3$ -based systems [59]. Among these methods, ab initio MD simulation is widely employed to capture the electronic structure and dynamic behavior of catalytic interfaces at finite temperatures. However, ab initio MD simulations are computationally expensive, limiting their application to short time scales [170–175]. To overcome this limitation, machine learning potentials (MLPs) trained on DFT data have been developed, offering an efficient alternative for extended simulations while retaining DFT-level accuracy [176–185].

This study employs MLP to investigate the oxygen evolution reaction through metadynamics simulations. Figure 9 outlines the MLP training process, which involves constructing a dataset that captures the configurational space of oxygen evolution reaction over  $\text{BaTiO}_3$  and  $\text{Ni}/\text{BaTiO}_3$  slabs [60]. Additionally, single-point DFT calculations can be applied to selected structures, improving efficiency through parallelization, unlike the inherently sequential nature of MD simulation.

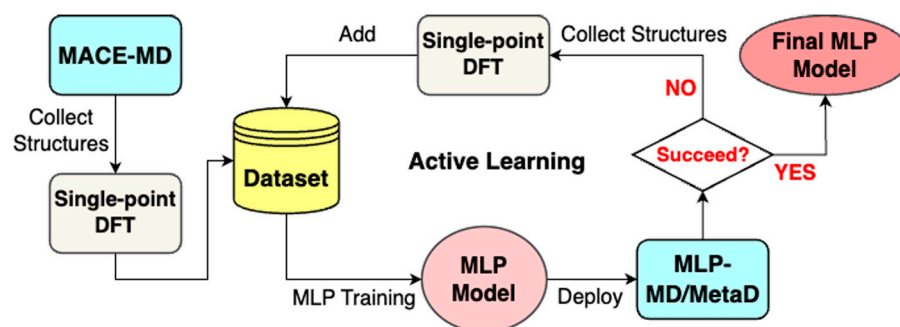


**Figure 9.** Overview of the MLP training workflow for MD simulations using DFT data. Reprinted from [60].

The stepwise mechanism of oxygen evolution reaction mechanism, as depicted in Figure 10, is analyzed using free energy surface calculations.

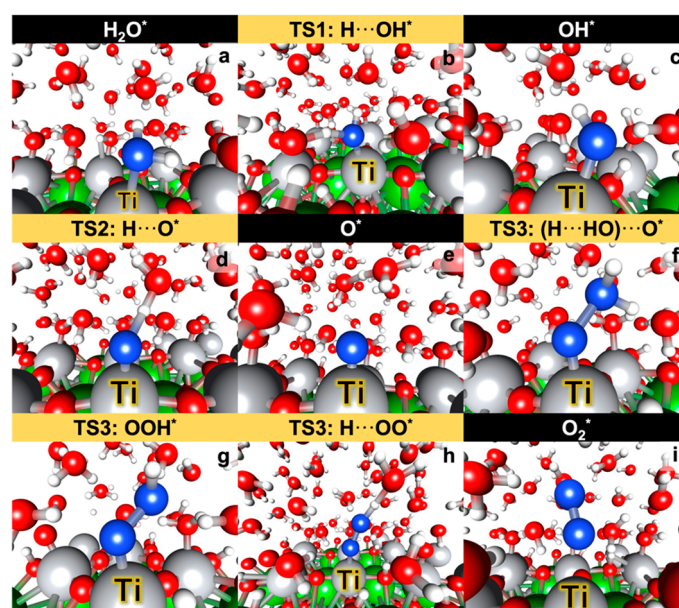


**Figure 10.** Illustration of the oxygen evolution reaction mechanism observed in the MLP-metadynamics trajectory of the BaTiO<sub>3</sub> (4 × 4)/128H<sub>2</sub>O system, with the Ti active site annotated. Reprinted from [60].

The catalytic process was analyzed using ab initio MD simulations with VASP, as shown in Figure 11. The newly formed oxygen molecule indicates that oxygen continuously dissolves in water, sustaining OOH generation and continuous H<sub>2</sub>O<sub>2</sub> production. Figure 11d,e further reveal the presence of OH radicals, formed either by water oxidation or H<sub>2</sub>O<sub>2</sub> decomposition, emphasizing the role of O<sub>2</sub><sup>−</sup> radicals in OH radical formation (Table 2).

Boonpalit et al. investigated the oxygen evolution reaction on pristine and Ni-doped BaTiO<sub>3</sub> surfaces using metadynamics simulations with machine learning interatomic potentials. Their study aimed to develop cost-effective alternatives to expensive Pt and IrOx/RuOx catalysts for electrocatalytic water splitting [60]. Their results revealed that Ni doping enhances BaTiO<sub>3</sub>'s catalytic activity by lowering the free energy barrier for oxo-oxo bond formation, aligning with experimental findings. However, the study did not account for the lattice oxygen-mediated mechanism, suggesting future work in this area. The database and machine learning potential developed in this study lay a foundation for further investigations into complex catalytic pathways, extending to broader electrochemical reactions at electrode–electrolyte interfaces in explicit solvent environments [60].

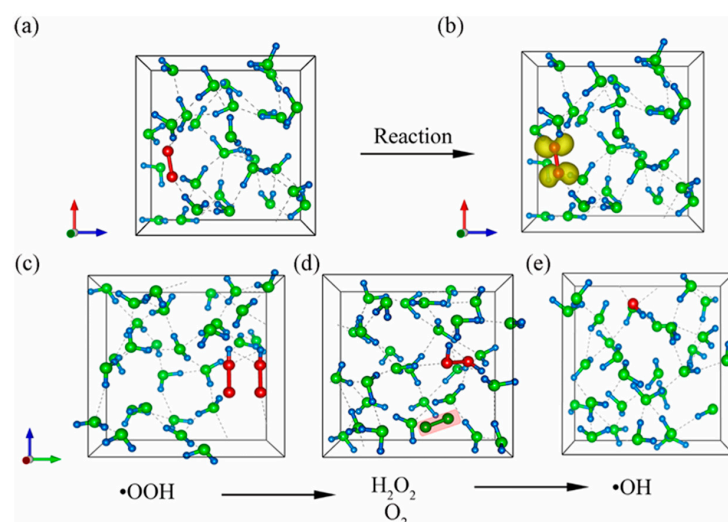


**Figure 11.** Representations of the ab initio MD simulations, depicting (a) a model with water molecules and a single oxygen molecule before the catalytic reaction and (b) after the reaction. It also includes (c) a model of a single OOH radical before the reaction, (d) the conversion of two OOH radicals into a single  $\text{H}_2\text{O}_2$  and  $\text{O}_2$  molecule, and (e) OH radicals derived from  $\text{H}_2\text{O}_2$  after the reaction. Reprinted with permission from [186]. Copyright 2024, American Chemical Society [186].

**Table 2.** Recently performed ab initio MD simulation details and main findings.

Designed System	Methods	Main Findings
BaTiO <sub>3</sub> surface [60]	Spin-polarized DFT calculations (VASP) with PAW pseudopotentials. High plane-wave cutoff (520 eV). Dataset of 16,162 configurations, trained with a 95:5 train-validation split, utilizing a multi-layer perceptron (tanh activation).	The energy barrier for oxygen desorption is lower than for oxygen evolution reaction, leading to the choice of specific metadynamics parameters (Gaussian height = 0.01 eV, width = 0.05, deposition rate = 6.25 fs). Water dissociation on the surface forms OH* intermediates with a free energy barrier ( $\Delta G^\ddagger \text{H}_2\text{O} \rightarrow \text{OH}$ ) of 0.06 eV for BaTiO <sub>3</sub> .
	MD simulations were conducted at 300 K, 500 K, and 700 K for 50 ps. Production MD simulations: accelerated with MLP models and run for 500 ps at 300 K with a timestep of 0.25 fs.	Oxygen evolution reaction steps analyzed using coordination number as collective variables. Formation of OOH* species occurs when coordination number ( $\text{O}_\text{s}\text{-O}_\text{aw}$ ) $\approx$ 0.3. Transition from OOH* to $\text{O}_2^*$ is barrierless with rapid proton abstraction.
	Metadynamics simulations: explored oxygen evolution reaction mechanisms using coordination number as collective variables and studied oxygen desorption by tracking Ti-O <sub>2</sub> /Ni-O <sub>2</sub> distances.	The calculated free energy barrier for the $\text{O} \rightarrow \text{O}_2$ transition ( $\Delta G^\ddagger \text{O} \rightarrow \text{O}_2$ ) is 1.57 eV for BaTiO <sub>3</sub> and 1.20 eV for Ni/BaTiO <sub>3</sub> . The oxygen desorption step is endothermic, with $\Delta G^\circ \text{O} \rightarrow \text{O}_2$ values of 1.37 eV for BaTiO <sub>3</sub> and 0.97 eV for Ni/BaTiO <sub>3</sub> . MLP models enable longer simulation times with DFT-level accuracy, improving efficiency compared to ab initio MD.
Covalent triazine frameworks (CTF)/BaTiO <sub>3</sub> photoanodes [186]	DFT calculations using VASP 6.3.0. PBE functional within GGA. Plane-wave energy cutoff: 500 eV. K-mesh: $8 \times 8 \times 8$ for bulk and $3 \times 2 \times 1$ for supercell BaTiO <sub>3</sub> -x. BaTiO <sub>3</sub> -x slab modeled with (001) surface and $(3 \times 3 \times 1)$ supercell with 30 Å vacuum. CTF/BaTiO <sub>3</sub> -x model constructed by depositing CTF on BaTiO <sub>3</sub> -x slab.	Introduction of CTF reduces the rate-determining step energy barrier from 1.03 eV to 0.84 eV, enhancing oxygen evolution reaction kinetics. The CTF/BaTiO <sub>3</sub> -x photoanode achieves a high photocurrent density of 0.83 mA/cm <sup>2</sup> at 1.23 V and a low onset potential of 0.23 V. CTF acts as a protective layer, improving stability for real water redox reactions. Provides a universal strategy for organic/inorganic hybrid photoanodes with high photoconversion efficiency.

Next, Wang et al. investigated the piezo-photocatalytic process by fabricating Ba<sub>0.7</sub>Sr<sub>0.3</sub>TiO<sub>3</sub> nanorod arrays on fluorine-doped tin oxide-coated glass as recoverable



catalysts. Their study demonstrated that the piezoelectric effect significantly enhances photocatalytic efficiency. Under ultrasonic vibrations, the degradation rate constant ( $k$ ) for rhodamine B using poled  $\text{Ba}_{0.7}\text{Sr}_{0.3}\text{TiO}_3$  nanorod reached  $0.0447 \text{ min}^{-1}$ , which was twice as high as that of the unpoled  $\text{Ba}_{0.7}\text{Sr}_{0.3}\text{TiO}_3$  nanorod ( $0.00183 \text{ min}^{-1}$ ). This improvement was attributed to the piezoelectric potential generated by poled  $\text{Ba}_{0.7}\text{Sr}_{0.3}\text{TiO}_3$  nanorod. Additionally, the  $\text{Ba}_{0.7}\text{Sr}_{0.3}\text{TiO}_3$  nanorodarray exhibited a hydrogen production rate of  $411.5 \mu\text{mol g}^{-1} \text{ h}^{-1}$ . Ab initio MD simulations revealed that hydroxyl radicals ( $\bullet\text{OH}$ ) played a dominant role over superoxide radicals ( $\bullet\text{O}_2^-$ ) in the degradation process [186].

### 2.3. Classical All-Atom MD Simulations

Classical all-atom MD simulations have proven to be an essential tool for understanding the atomic-scale interactions between the  $\text{BaTiO}_3$  surface and  $\text{OH}^-$  ions in aqueous environments, particularly under different polarization conditions [186–194]. These simulations provide valuable insights into adsorption behavior, surface charge effects, and polarization-induced modifications that influence  $\text{BaTiO}_3$ 's role in solar water splitting applications. To illustrate this, Figure 12 presents the adsorption of  $\text{OH}^-$  ions on  $\text{BaTiO}_3$  surfaces at varying  $\text{H}_2\text{O}:\text{OH}^-$  ratios under both unpolarized and positively polarized conditions. Additionally, Table 3 summarizes recent classical all-atom MD studies investigating these interactions, detailing their methodologies and key findings.

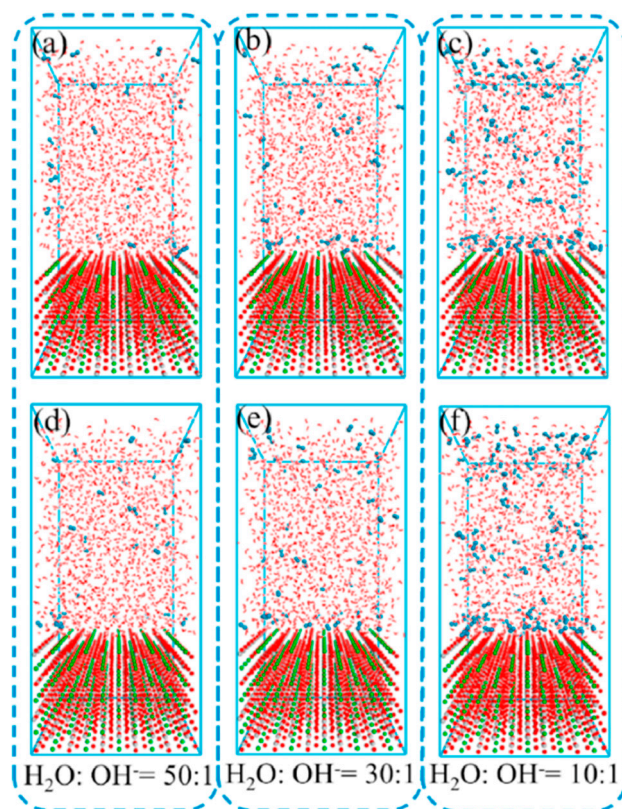


**Figure 12.** Adsorption of  $\text{OH}^-$  ions onto the  $\text{BaTiO}_3$  surface at different  $\text{H}_2\text{O}:\text{OH}^-$  ratios, including (a) unpolarized and (d) positively polarized ( $0.01 \text{ V \AA}^{-1}$ )  $\text{BaTiO}_3$  surfaces at an  $\text{H}_2\text{O}:\text{OH}^-$  ratio of 30:1, (b) unpolarized and (e) positively polarized ( $0.01 \text{ V \AA}^{-1}$ )  $\text{BaTiO}_3$  surfaces at an  $\text{H}_2\text{O}:\text{OH}^-$  ratio of 10:1, and (c) unpolarized and (f) positively polarized ( $0.01 \text{ V \AA}^{-1}$ )  $\text{BaTiO}_3$  surfaces at an  $\text{H}_2\text{O}:\text{OH}^-$  ratio of 50:1. Reprinted with permission from [59]. Copyright 2022, Elsevier [59].



**Table 3.** Recently performed classical all-atom MD simulation details and main findings.

Designed Systems	Methods	Main Findings
BaTiO <sub>3</sub> surface and its interaction with OH <sup>−</sup> ions in an electrolyte [59]	DFT calculation. Materials Studio. Classical all-atom MD Simulations. Forcite module in Materials Studio. COMPASSIII force field. Electric field of 0.01 eV/Å applied to study positive polarization effects.	Higher OH <sup>−</sup> concentration leads to increased adsorption on the BaTiO surface. At a 10:1 (H <sub>2</sub> O:OH <sup>−</sup> ) ratio, adsorption is significantly higher compared to a 50:1 ratio. At a 50:1 (H <sub>2</sub> O:OH <sup>−</sup> ) ratio, polarization significantly impacts OH <sup>−</sup> adsorption, but at higher OH <sup>−</sup> concentrations, the effect diminishes. Polarization field enhances photoanode performance in near-neutral conditions by improving surface states and hole collection efficiency.

At lower pH values, the positively polarized sample exhibits the highest  $V_{ph}$ , while the negatively polarized sample shows the lowest photovoltage, indicating that polarization enhances the generation of non-equilibrium carriers (Figure 12). However, at higher pH values, the photovoltage of both polarized photoanodes decreases compared to the unpolarized sample. This suggests that, at high pH, the presence of BaTiO<sub>3</sub> influences the surface behavior differently, impacting the overall performance.

Chen et al. employed molecular dynamics simulations and density functional theory calculations to investigate the impact of ferroelectric polarization on photoelectrochemical water oxidation. Their study demonstrated that the polarization field of BaTiO<sub>3</sub> can significantly enhance the photocurrent density of a hybrid metal oxide/BaTiO<sub>3</sub> photoanode by approximately 30% in near-neutral electrolytes. This improvement is attributed to the polarization-induced enhancement of surface states and donor density within the space charge layer, which facilitates hole collection and improves reaction kinetics. However, computational findings revealed that, at high pH values, the adsorption capacity of OH<sup>−</sup> ions on polarized and unpolarized BaTiO<sub>3</sub> surfaces becomes nearly identical, weakening the effect of the ferroelectric polarization field [59]. Consequently, the polarized field has a minimal influence on photoelectrochemical performance in alkaline conditions. Their work highlights the critical role of electrolyte pH in optimizing ferroelectric materials for photoelectrochemical applications, offering new insights into their mechanistic behavior.

While classical all-atom MD simulations have predominantly been used to study BaTiO<sub>3</sub> in photoelectrochemical applications, their potential extends to photocatalytic processes as well [195–200]. By investigating ion adsorption, interfacial charge transfer, and surface state modifications, classical all-atom MD simulations can provide deeper mechanistic insights into BaTiO<sub>3</sub>-based photocatalysts for solar-driven water splitting and related reactions. In conclusion, it is also important to note that calculations of defect-induced Raman modes allow a more in-depth consideration and understanding of the role of surface defects [201–206].

While theoretical and atomistic simulation studies have greatly advanced our understanding of BaTiO<sub>3</sub> as a promising photocatalyst for solar-driven water splitting, experimental validation remains crucial for translating these insights into practical applications. Despite significant computational progress, experimental data on the photocatalytic water decomposition activity of BaTiO<sub>3</sub>, especially with various modifications, are relatively limited. This gap underscores the need for more robust experimental investigations to complement and verify theoretical predictions.

#### 2.4. Related Experimental Findings

Ferroelectric BaTiO<sub>3</sub> possesses spontaneous polarization, which creates a built-in internal electric field within the material. This internal field serves as a driving force that actively separates the photogenerated electrons and holes when the material is exposed to light [207]. By pulling the oppositely charged carriers in different directions, the field significantly suppresses their recombination, which is a key factor in enhancing photocatalytic efficiency.

The polarization-induced field also results in band bending at the surface or heterointerfaces of BaTiO<sub>3</sub>. This band bending further assists in directing electrons and holes toward different spatial regions, improving charge transport pathways, especially crucial in nanoscale structures or thin films, where surface effects dominate [208,209]. Such spatial separation enhances redox reactions at the surface, which are vital for photocatalytic applications.

However, strong interactions between the photogenerated charges and the polarized lattice ions can sometimes lead to trapping, which hinders charge mobility and reduces the benefit of polarization-induced separation. This challenge can be mitigated through heterostructure engineering [207–209]. By coupling BaTiO<sub>3</sub> with other semiconductors like TiO<sub>2</sub> or CdS, the internal electric field can propagate across the interface, extending the charge separation effect into adjacent phases. This interfacial charge migration not only mitigates charge trapping, but also boosts overall photocatalytic performance. These mechanisms are illustrated schematically in Figure 13a, which shows both the polarization-driven separation process and various modification strategies to enhance BaTiO<sub>3</sub>-based photocatalysts.

Although BaTiO<sub>3</sub> is recognized as a promising photocatalyst, its practical application on a large scale remains limited due to its wide bandgap (~3.2 eV), poor visible-light activity, and rapid recombination of photogenerated electron–hole pairs caused by strong Coulombic attraction. To overcome these limitations, various strategies have been developed to enhance charge separation and extend light absorption into the visible region. These include controlling particle size and morphology, doping with metal and non-metal elements, integrating noble metal nanoparticles (plasmonic photocatalysts), constructing heterojunctions, and others, as illustrated in Figure 13b and further discussed in relevant review articles [207–213].

Experimental studies have demonstrated the potential of BaTiO<sub>3</sub>-based materials for photocatalytic water splitting, particularly when modified through doping, polarization, or heterojunction design [207–213].

For example, BaTiO<sub>3</sub> nanocrystal films deposited on Ta substrates produced a water oxidation photocurrent of 0.141 mA/cm<sup>2</sup> at 1.23 V vs. RHE under 60 mW/cm<sup>2</sup> UV illumination, with ferroelectric polarization and a Pt co-catalyst boosting the hydrogen evolution rate by approximately 1.5× [214]. Figure 14 presents experimental evidence of hydrogen production using Pt-loaded BaTiO<sub>3</sub> in aqueous methanol under (a) 60 mW/cm<sup>2</sup> UV and (b) 375 nm LED (5.5 mW/cm<sup>2</sup>) illumination [214]. Iridium-doped BaTiO<sub>3</sub> (Ir<sup>3+</sup>:BTO) shows an approximately 1.6× increase in photocurrent under visible light and a 100-fold enhancement in hydrogen evolution compared to Ir<sup>4+</sup>:BTO, due to improved charge dynamics and Faradaic efficiency [215]. Furthermore, heterostructures such as BaTiO<sub>3</sub>/NiFe<sub>2</sub>O<sub>4</sub> nanocomposites yield higher photocurrent densities (~0.34 mA/cm<sup>2</sup>) than pristine BaTiO<sub>3</sub>, reflecting synergistic effects [216]. Similarly, SrTiO<sub>3</sub>/BaTiO<sub>3</sub> nanofiber heterojunctions exhibit piezoelectric-assisted photocatalytic hydrogen generation with notable efficiency, even though exact photocurrent values are not always reported [155]. These findings underscore that optimization of ferroelectric properties, strategic doping, and construction of het-

erostructures are effective routes for enhancing BaTiO<sub>3</sub>'s photocatalytic performance under both UV and visible light and are further discussed in relevant review articles [207–216].

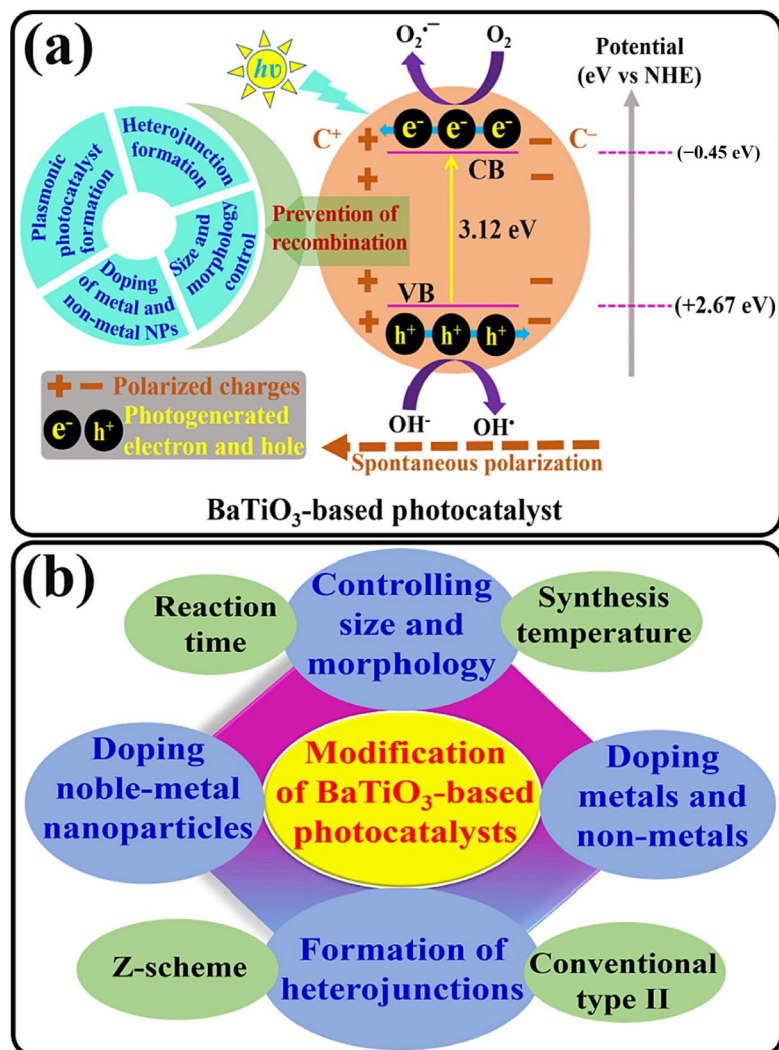


**Figure 13.** (a) Schematic representation of spontaneous polarization and the photocatalytic process in BaTiO<sub>3</sub>-based materials. (b) Various approaches for synthesizing modified BaTiO<sub>3</sub>-based photocatalysts. Reprinted with permission from [207]. Copyright 2022, Elsevier [207].

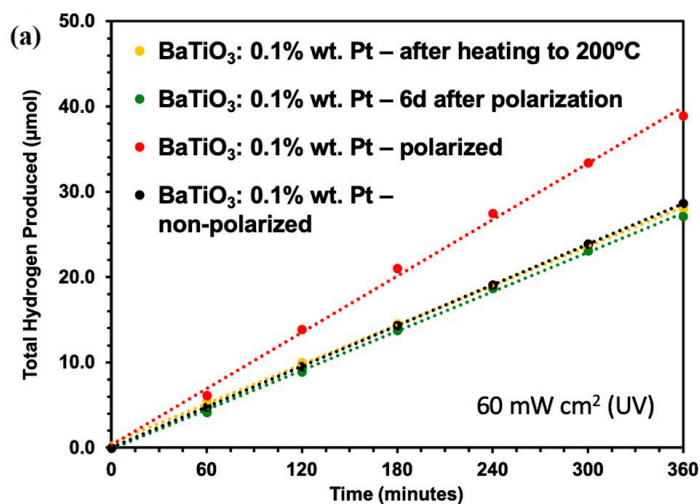


**Figure 14.** Cont.

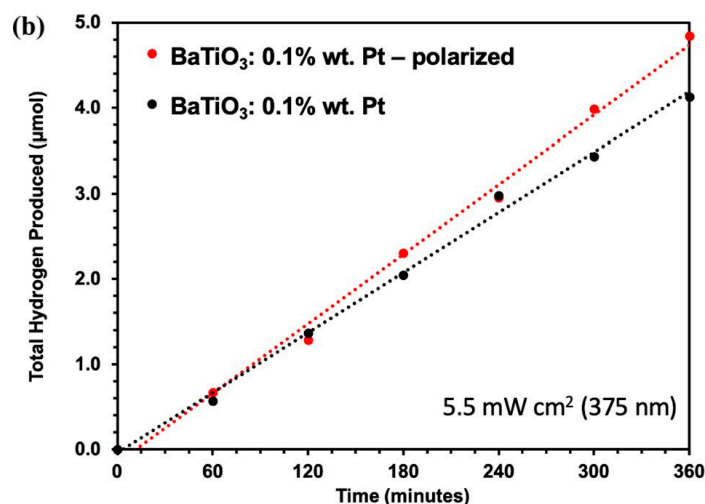


**Figure 14.** Hydrogen generation was evaluated using BaTiO<sub>3</sub> loaded with Pt in aqueous methanol solution under two conditions: (a) UV light irradiation at an intensity of 60 mW/cm<sup>2</sup> and (b) illumination with a 375 nm LED light source at 5.5 mW/cm<sup>2</sup>. Reprinted with permission from [214]. Copyright 2023, ACS [214].

### 3. Conclusions and Outlook

BaTiO<sub>3</sub> has demonstrated significant potential as a photocatalyst for solar water splitting due to its favorable electronic and ferroelectric properties. Atomistic simulations, particularly DFT, ab initio MD, classical all-atom MD, and MLP-based studies, have played a pivotal role in elucidating the fundamental mechanisms governing its photocatalytic activity. DFT calculations have provided insights into band structure modifications, defect engineering, and doping strategies, while ab initio MD and classical all-atom MD simulations have revealed the dynamic interactions of BaTiO<sub>3</sub> surfaces with water molecules under realistic conditions. Furthermore, MLP-assisted metadynamics simulations have emerged as a powerful tool for overcoming the computational limitations of traditional ab initio MD approaches. Collectively, these studies highlight the importance of computational modeling in optimizing BaTiO<sub>3</sub>-based photocatalysts. However, challenges such as charge recombination, surface stability, and scalability of synthesis methods remain critical obstacles that need to be addressed for practical applications.

Experimental studies have confirmed the photocatalytic potential of BaTiO<sub>3</sub>, particularly under ultraviolet light, and have demonstrated that strategic modifications, such as non-metal/metal doping, co-doping, and heterojunction formation, significantly enhance its visible-light activity and charge separation efficiency. Despite these advances, challenges related to scalability, stability, and limited quantum efficiency remain, highlighting the need for further experimental and computational efforts to optimize BaTiO<sub>3</sub>-based photocatalysts for practical solar hydrogen production.

Future research should focus on integrating multiscale modeling techniques to bridge the gap between atomistic simulations and experimental validation. The incorporation of hybrid DFT functionals and beyond-DFT methods could improve the accuracy of electronic structure predictions, particularly for defect states and charge transport mechanisms. Additionally, the development of advanced machine learning potentials tailored for BaTiO<sub>3</sub> could further accelerate large-scale simulations and enhance predictive capabilities. Experimentally, synthesizing BaTiO<sub>3</sub>-based heterostructures with co-catalysts and optimizing defect engineering strategies will be crucial for improving catalytic performance. A deeper exploration of photoelectrochemical and piezo-photocatalytic effects in BaTiO<sub>3</sub> could unlock new pathways for enhancing efficiency. Overall, a synergistic approach combining

computational modeling and experimental techniques will be essential to realize the full potential of BaTiO<sub>3</sub> for sustainable hydrogen production.

**Author Contributions:** A.U.A., U.Z.T. and B.M.S.: conceptualization, methodology, formal analysis, writing—original draft, review and editing; T.M.I.: funding acquisition, writing—original draft, review and editing; M.K.: conceptualization, visualization, writing—review and editing; F.U.A.: conceptualization, formal analysis, writing—original draft, review and editing; A.I.P.: funding acquisition, writing—review and editing. All authors have read and agreed to the published version of the manuscript.

**Funding:** This research was funded by the Science Committee of the Ministry of Science and Higher Education of the Republic of Kazakhstan “Development of hybrid perovskite nanostructures for hydrogen photogeneration” (Grant No. AP23489103). This research was also funded by the Science Committee of the Ministry of Science and Higher Education of the Republic of Kazakhstan “Green Energy: Foundational Research of Solar Fuel Technologies for Sustainable Production and Advanced Storage” (Grant No. BR21882439).

**Institutional Review Board Statement:** Not applicable.

**Informed Consent Statement:** Not applicable.

**Data Availability Statement:** No new data were created or analyzed in this study.

**Acknowledgments:** This research was funded by the Science Committee of the Ministry of Science and Higher Education of the Republic of Kazakhstan “Development of hybrid perovskite nanostructures for hydrogen photogeneration” (Grant No. AP23489103). This research was also funded by the Science Committee of the Ministry of Science and Higher Education of the Republic of Kazakhstan “Green Energy: Foundational Research of Solar Fuel Technologies for Sustainable Production and Advanced Storage” (Grant No. BR21882185). The work of Anatoli Popov is supported by the LZP project 2023/1-0453.

**Conflicts of Interest:** The authors declare no conflicts of interest.

## Abbreviations

BaTiO <sub>3</sub>	Barium titanate
BiFeO <sub>3</sub>	Bismuth ferrite
BiVO <sub>4</sub>	Bismuth vanadate
CB	Conduction band
CdS	Cadmium sulfide
CO	Carbon monoxide
CO <sub>2</sub>	Carbon dioxide
CTF	Carbon triazine framework
DFT	Density functional theory
DFT + U	Density functional theory + Hubbard U correction
FDTD	Finite-difference time-domain
GGA	Generalized gradient approximation
HSE	Hybrid functional
HF	Hartree–Fock
LaAlO <sub>3</sub>	Lanthanum aluminate
LDA	Local density approximation
MD	Molecular dynamics
MLP	Machine learning potentials
PAW	Projector augmented wave
PBE	Perdew–Burke–Ernzerhof
SrTiO <sub>3</sub>	Strontium titanate
TiO <sub>2</sub>	Titanium dioxide



VB	Valence band
VASP	Vienna Ab initio Simulation Package

## References

1. Atilhan, S.; Park, S.; El-Halwagi, M.M.; Atilhan, M.; Moore, M.; Nielsen, R.B. Green hydrogen as an alternative fuel for the shipping industry. *Curr. Opin. Chem. Eng.* **2021**, *31*, 100668. [\[CrossRef\]](#)
2. Qazi, U.Y. Future of hydrogen as an alternative fuel for next-generation industrial applications; challenges and expected opportunities. *Energies* **2022**, *15*, 4741. [\[CrossRef\]](#)
3. Nurmanova, S.; Kolisnichenko, S.; Kokayev, U.; Kalmanova, D.; Karazhanov, A.; Alipbayev, Z.; Abuova, F.; Abdirashev, O.; Satanova, B. Optimizing waste motor oil recycling into diesel using novel deep eutectic solvents: An atomistic study. *ES Mater. Manuf.* **2025**, *28*, 1480. [\[CrossRef\]](#)
4. Kaiwen, L.; Bin, Y.; Tao, Z. Economic analysis of hydrogen production from steam reforming process: A literature review. *Energy Sources Part B Econ. Plan. Policy* **2018**, *13*, 109–115. [\[CrossRef\]](#)
5. Franchi, G.; Capocelli, M.; De Falco, M.; Piemonte, V.; Barba, D. Hydrogen production via steam reforming: A critical analysis of MR and RMM technologies. *Membranes* **2020**, *10*, 10. [\[CrossRef\]](#)
6. Ranjekar, A.M.; Yadav, G.D. Steam reforming of methanol for hydrogen production: A critical analysis of catalysis, processes, and scope. *Ind. Eng. Chem. Res.* **2021**, *60*, 89–113. [\[CrossRef\]](#)
7. Wang, M.; Wang, Z.; Gong, X.; Guo, Z. The intensification technologies to water electrolysis for hydrogen production—A review. *Renew. Sustain. Energy Rev.* **2014**, *29*, 573–588. [\[CrossRef\]](#)
8. El-Shafie, M. Hydrogen production by water electrolysis technologies: A review. *Results Eng.* **2023**, *20*, 101426. [\[CrossRef\]](#)
9. Shayan, E.; Zare, V.; Mirzaee, I.J.E.C. Hydrogen production from biomass gasification; A theoretical comparison of using different gasification agents. *Energy Convers. Manag.* **2018**, *159*, 30–41. [\[CrossRef\]](#)
10. Tezer, Ö.; Karabağ, N.; Öngen, A.; Çolpan, C.Ö.; Ayol, A. Biomass gasification for sustainable energy production: A review. *Int. J. Hydrogen Energy* **2022**, *47*, 15419–15433. [\[CrossRef\]](#)
11. Akhlaghi, N.; Najafpour-Darzi, G. A comprehensive review on biological hydrogen production. *Int. J. Hydrogen Energy* **2020**, *45*, 22492–22512. [\[CrossRef\]](#)
12. Xu, X.; Zhou, Q.; Yu, D. The future of hydrogen energy: Bio-hydrogen production technology. *Int. J. Hydrogen Energy* **2022**, *47*, 33677–33698. [\[CrossRef\]](#)
13. Razi, F.; Dincer, I.; Gabriel, K. Exergoenvironmental analysis of the integrated copper-chlorine cycle for hydrogen production. *Energy* **2021**, *226*, 120426. [\[CrossRef\]](#)
14. Stružnik, D.; Avsec, J. Exergoeconomic machine-learning method of integrating a thermochemical Cu–Cl cycle in a multigeneration combined cycle gas turbine for hydrogen production. *Int. J. Hydrogen Energy* **2022**, *47*, 17121–17149. [\[CrossRef\]](#)
15. Myrzakhmetov, B.; Akhmetova, A.; Bissenbay, A.; Karibayev, M.; Pan, X.; Wang, Y.; Bakenov, Z.; Mentbayeva, A. Chitosan-based biopolymers for anion-exchange membrane fuel cell application. *R. Soc. Open Sci.* **2023**, *10*, 230843. [\[CrossRef\]](#)
16. Song, H.; Luo, S.; Huang, H.; Deng, B.; Ye, J. Solar-driven hydrogen production: Recent advances, challenges, and future perspectives. *ACS Energy Lett.* **2022**, *7*, 1043–1065. [\[CrossRef\]](#)
17. Takeda, S.; Nam, H.; Chapman, A. Low-carbon energy transition with the sun and forest: Solar-driven hydrogen production from biomass. *Int. J. Hydrogen Energy* **2022**, *47*, 24651–24668. [\[CrossRef\]](#)
18. Lim, Y.; Lee, D.-K.; Kim, S.M.; Park, W.; Cho, S.Y.; Sim, U. Low Dimensional Carbon-Based Catalysts for Efficient Photocatalytic and Photo/Electrochemical Water Splitting Reactions. *Materials* **2020**, *13*, 114. [\[CrossRef\]](#)
19. Eidsvåg, H.; Bentouba, S.; Vajeeston, P.; Yohi, S.; Velauthapillai, D. TiO<sub>2</sub> as a Photocatalyst for Water Splitting—An Experimental and Theoretical Review. *Molecules* **2021**, *26*, 1687. [\[CrossRef\]](#)
20. Nadeem, M.A.; Khan, M.A.; Ziani, A.A.; Idriss, H. An Overview of the Photocatalytic Water Splitting over Suspended Particles. *Catalysts* **2021**, *11*, 60. [\[CrossRef\]](#)
21. Arunachalam, P.; Nagai, K.; Amer, M.S.; Ghanem, M.A.; Ramalingam, R.J.; Al-Mayouf, A.M. Recent Developments in the Use of Heterogeneous Semiconductor Photocatalyst Based Materials for a Visible-Light-Induced Water-Splitting System—A Brief Review. *Catalysts* **2021**, *11*, 160. [\[CrossRef\]](#)
22. Tian, L.; Guan, X.; Zong, S.; Dai, A.; Qu, J. Cocatalysts for Photocatalytic Overall Water Splitting: A Mini Review. *Catalysts* **2023**, *13*, 355. [\[CrossRef\]](#)
23. Jakhar, M.; Kumar, A.; Ahluwalia, P.K.; Tankeshwar, K.; Pandey, R. Engineering 2D Materials for Photocatalytic Water-Splitting from a Theoretical Perspective. *Materials* **2022**, *15*, 2221. [\[CrossRef\]](#)
24. Dauletbekova, A.; Abuova, F.; Piskunov, S. First-principles modeling of the H color centers in MgF<sub>2</sub> crystals. *Phys. Status Solidi C* **2012**, *10*, 160–164. [\[CrossRef\]](#)
25. Abuova, F.U.; Kotomin, E.A.; Lisitsyn, V.M.; Akilbekov, A.T.; Piskunov, S. Ab initio modeling of radiation damage in MgF<sub>2</sub> crystals. *Nucl. Instrum. Methods Phys. Res. B* **2014**, *326*, 314–317. [\[CrossRef\]](#)

26. Abuova, A.U.; Mastrikov, Y.A.; Kotomin, E.A.; Kawazoe, Y.; Inerbaev, T.M.; Akilbekov, A.T. First principles modeling of Ag adsorption on the LaMnO<sub>3</sub> (001) surfaces. *Solid State Ionics* **2015**, *273*, 46–50. [\[CrossRef\]](#)
27. Guo, S.; Lin, H.; Hu, J.; Su, Z.; Zhang, Y. Computational Study of Novel Semiconducting Sc<sub>2</sub>CT<sub>2</sub> (T = F, Cl, Br) MXenes for Visible-Light Photocatalytic Water Splitting. *Materials* **2021**, *14*, 4739. [\[CrossRef\]](#)
28. Wang, G.; Xie, W.; Guo, S.; Chang, J.; Chen, Y.; Long, X.; Zhou, L.; Ang, Y.S.; Yuan, H. Two-Dimensional GeC/MXY (M = Zr, Hf; X, Y = S, Se) Heterojunctions Used as Highly Efficient Overall Water-Splitting Photocatalysts. *Molecules* **2024**, *29*, 2793. [\[CrossRef\]](#)
29. Wang, Y.; Wang, H.; Li, Y.; Zhang, M.; Zheng, Y. Designing a 0D/1D S-Scheme Heterojunction of Cadmium Selenide and Polymeric Carbon Nitride for Photocatalytic Water Splitting and Carbon Dioxide Reduction. *Molecules* **2022**, *27*, 6286. [\[CrossRef\]](#)
30. Yan, Y.; Chen, Z.; Cheng, X.; Shi, W. Research Progress of ZnIn<sub>2</sub>S<sub>4</sub>-Based Catalysts for Photocatalytic Overall Water Splitting. *Catalysts* **2023**, *13*, 967. [\[CrossRef\]](#)
31. Zhang, H.; Liu, J.; Xu, T.; Ji, W.; Zong, X. Recent Advances on Small Band Gap Semiconductor Materials ( $\leq 2.1$  eV) for Solar Water Splitting. *Catalysts* **2023**, *13*, 728. [\[CrossRef\]](#)
32. Morante, N.; Folliero, V.; Dell'Annunziata, F.; Capuano, N.; Mancuso, A.; Monzillo, K.; Galdiero, M.; Sannino, D.; Franci, G. Characterization and Photocatalytic and Antibacterial Properties of Ag- and TiO<sub>x</sub>-Based (x = 2, 3) Composite Nanomaterials under UV Irradiation. *Materials* **2024**, *17*, 2178. [\[CrossRef\]](#)
33. Zhao, Z.; Li, R.; Zhao, C.; Pei, J. A Study on the Effect of Conductive Particles on the Performance of Road-Suitable Barium Titanate/Polyvinylidene Fluoride Composite Materials. *Materials* **2025**, *18*, 1185. [\[CrossRef\]](#)
34. Mamani Flores, E.; Vera Barrios, B.S.; HuilcaHuillca, J.C.; Chacaltana García, J.A.; Polo Bravo, C.A.; Nina Mendoza, H.E.; Quispe Cohaila, A.B.; Gamarra Gómez, F.; Tamayo Calderón, R.M.; Fora Quispe, G.d.L.; et al. Cr<sup>3+</sup> Doping Effects on Structural, Optical, and Morphological Characteristics of BaTiO<sub>3</sub> Nanoparticles and Their Bioactive Behavior. *Crystals* **2024**, *14*, 998. [\[CrossRef\]](#)
35. Abidin, M.Z.U.; Ikram, M.; Moeen, S.; Nazir, G.; Kanoun, M.B.; Goumri-Said, S. A comprehensive review on the synthesis of ferrite nanomaterials via bottom-up and top-down approaches: Advantages, disadvantages, characterizations, and computational insights. *Coord. Chem. Rev.* **2024**, *520*, 216158. [\[CrossRef\]](#)
36. Jiang, Q.; Cui, X.F.; Zhao, M. Size effects on Curie temperature of ferroelectric particles. *Appl. Phys. A Mater. Sci. Process.* **2004**, *78*, 703–704. [\[CrossRef\]](#)
37. Sood, A.; Desseigne, M.; Dev, A.; Maurizi, L.; Kumar, A.; Millot, N.; Han, S.S. A Comprehensive Review on Barium Titanate Nanoparticles as a Persuasive Piezoelectric Material for Biomedical Applications: Prospects and Challenges. *Small* **2023**, *19*, e2206401. [\[CrossRef\]](#) [\[PubMed\]](#)
38. Lang, X.Y.; Jiang, Q. Size and interface effects on Curie temperature of perovskite ferroelectric nanosolids. *J. Nanopart. Res.* **2007**, *9*, 595–603. [\[CrossRef\]](#)
39. Wada, S.; Hoshina, T.; Yasuno, H.; Ohishi, M.; Kakemoto, H.; Tsurumi, T.; Yashima, M. Size Effect of Dielectric Properties for Barium Titanate Particles and Its Model. *Key Eng. Mater.* **2006**, *301*, 27–30. [\[CrossRef\]](#)
40. Chakraborty, A.; Liton, M.; Sarker, M.; Rahman, M.; Khan, M. A comprehensive DFT evaluation of catalytic and optoelectronic properties of BaTiO<sub>3</sub> polymorphs. *Phys. B Condens. Matter* **2023**, *648*, 414418. [\[CrossRef\]](#)
41. Navas, D.; Fuentes, S.; Castro-Alvarez, A.; Chavez-Angel, E. Review on Sol-Gel Synthesis of Perovskite and Oxide Nanomaterials. *Gels* **2021**, *7*, 275. [\[CrossRef\]](#)
42. Lu, W.; Quilitz, M.; Schmidt, H. Nanoscaled BaTiO<sub>3</sub> powders with a large surface area synthesized by precipitation from aqueous solutions: Preparation, characterization and sintering. *J. Eur. Ceram. Soc.* **2007**, *27*, 3149–3159. [\[CrossRef\]](#)
43. Suherman, B.; Nurosyid, F.; Khairuddin; Sandi, D.K.; Irian, Y. Impacts of low sintering temperature on microstructure, atomic bonds, and dielectric constant of barium titanate (BaTiO<sub>3</sub>) prepared by co-precipitation technique. *J. Phys. Conf. Ser.* **2022**, *2190*, 012006. [\[CrossRef\]](#)
44. Hayashi, H.; Hakuta, Y. Hydrothermal Synthesis of Metal Oxide Nanoparticles in Supercritical Water. *Materials* **2010**, *3*, 3794–3817. [\[CrossRef\]](#) [\[PubMed\]](#)
45. Khort, A.A.; Podbolotov, K.B. Preparation of BaTiO<sub>3</sub> nanopowders by the solution combustion method. *Ceram. Int.* **2016**, *42*, 15343–15348. [\[CrossRef\]](#)
46. Choi, G.J.; Kim, H.S.; Cho, Y.S. BaTiO<sub>3</sub> particles prepared by microwave-assisted hydrothermal reaction using titanium acylate precursors. *Mater. Lett.* **1999**, *41*, 122–127. [\[CrossRef\]](#)
47. Buscaglia, V.; Buscaglia, M.T.; Canu, G. BaTiO<sub>3</sub>-Based Ceramics: Fundamentals, Properties and Applications. In *Encyclopedia of Materials: Technical Ceramics and Glasses*; Elsevier: Amsterdam, The Netherlands, 2021; pp. 311–344, ISBN 9780128222331.
48. Ramakanth, S.; James Raju, K.C. Band gap narrowing in BaTiO<sub>3</sub> nanoparticles facilitated by multiple mechanisms. *J. Appl. Phys.* **2014**, *115*, 173507. [\[CrossRef\]](#)
49. Tewatia, K.; Sharma, A.; Sharma, M.; Kumar, A. Factors affecting morphological and electrical properties of Barium Titanate: A brief review. *Mater. Today Proc.* **2021**, *44*, 4548–4556. [\[CrossRef\]](#)
50. Kumar, A.; Gori, Y.; Kumar, A.; Meena, C.S.; Dutt, N. (Eds.) *Advanced Materials for Biomedical Applications*, 1st ed.; Taylor and Francis: Boca Raton, FL, USA, 2023; ISBN 9781032356068.

51. Benyoussef, M.; Mura, T.; Saitzek, S.; Azrour, F.; Blach, J.-F.; Lahmar, A.; Gagou, Y.; El Marssi, M.; Sayede, A.; Jouiad, M. Nanostructured  $\text{BaTi}_{1-x}\text{Sn}_x\text{O}_3$  ferroelectric materials for electrocaloric applications and energy performance. *Curr. Appl. Phys.* **2022**, *38*, 59–66. [\[CrossRef\]](#)
52. Qiao, L.; Bi, X. Microstructure and grain size dependence of ferroelectric properties of  $\text{BaTiO}_3$  thin films on  $\text{LaNiO}_3$  buffered Si. *J. Eur. Ceram. Soc.* **2009**, *29*, 1995–2001. [\[CrossRef\]](#)
53. Buscaglia, M.T.; Buscaglia, V.; Viviani, M.; Nanni, P.; Hanuskova, M. Influence of foreign ions on the crystal structure of  $\text{BaTiO}_3$ . *J. Eur. Ceram. Soc.* **2000**, *20*, 1997–2007. [\[CrossRef\]](#)
54. Khedhri, M.H.; Abdelmoula, N.; Khemakhem, H.; Douali, R.; Dubois, F. Structural, spectroscopic and dielectric properties of Ca-doped  $\text{BaTiO}_3$ . *Appl. Phys. A Mater. Sci. Process.* **2019**, *125*, 193. [\[CrossRef\]](#)
55. Da Lu, Y.; Han, D.D.; Liu, Q.L.; Wang, Y.D.; Sun, X.Y. Structure and Dielectric Properties of Ce and Ca Co-Doped  $\text{BaTiO}_3$  Ceramics. *Key Eng. Mater.* **2016**, *680*, 184–188. [\[CrossRef\]](#)
56. Rached, A.; Wederni, M.A.; Belkahla, A.; Dhahri, J.; Khirouni, K.; Alaya, S.; Martin-Palma, R.J. Effect of doping in the physico-chemical properties of  $\text{BaTiO}_3$  ceramics. *Phys. B Condens. Matter* **2020**, *596*, 412343. [\[CrossRef\]](#)
57. Banerjee, T.; Balasubramanian, G. Predictive Modeling of Molecular Mechanisms in Hydrogen Production and Storage Materials. *Materials* **2023**, *16*, 6050. [\[CrossRef\]](#)
58. Inerbaev, T.M.; Abuova, A.U.; Zakiyeva, Z.Y.; Abuova, F.U.; Mastrikov, Y.A.; Sokolov, M.; Gryaznov, D.; Kotomin, E.A. Effect of Rh doping on optical absorption and oxygen evolution reaction activity on  $\text{BaTiO}_3$  (001) surfaces. *Molecules* **2024**, *29*, 2707. [\[CrossRef\]](#)
59. Chen, L.; Yu, Z.; Ji, X.; Huang, R.; Luo, L.; Tang, Z.; Zhang, Y. Insight into the effect of pH on the ferroelectric polarization field applied in photoelectrochemical water oxidation. *Mater. Sci. Semicond. Process.* **2022**, *147*, 106729. [\[CrossRef\]](#)
60. Boonpalit, K.; Artrith, N. Mechanistic Insights into the Oxygen Evolution Reaction on Nickel-Doped Barium Titanate via Machine Learning-Accelerated Simulations. *arXiv* **2024**, arXiv:2412.15452. [\[CrossRef\]](#)
61. Bradley, R.; Radhakrishnan, R. Coarse-Grained Models for Protein-Cell Membrane Interactions. *Polymers* **2013**, *5*, 890–936. [\[CrossRef\]](#)
62. Ren, H.; Yang, J.; Yang, W.; Zhong, H.; Lin, J.; Radjenovic, P.M.; Sun, L.; Zhang, H.; Xu, J.; Tian, Z.; et al. Core-Shell-Satellite plasmonic photocatalyst for broad-spectrum photocatalytic water splitting. *ACS Mater. Lett.* **2020**, *3*, 69–76. [\[CrossRef\]](#)
63. Goga, N.; Mayrhofer, L.; Tranca, I.; Nedea, S.; Heijmans, K.; Ponnuchamy, V.; Vasilateanu, A. A Review of Recent Developments in Molecular Dynamics Simulations of the Photoelectrochemical Water Splitting Process. *Catalysts* **2021**, *11*, 807. [\[CrossRef\]](#)
64. Abdikarimova, U.; Bissenova, M.; Matsko, N.; Issadykov, A.; Khromushin, I.; Aksenova, T.; Munasbayeva, K.; Slyamzhanov, E.; Serik, A. Visible Light-Driven Photocatalysis of Al-Doped  $\text{SrTiO}_3$ : Experimental and DFT Study. *Molecules* **2024**, *29*, 5326. [\[CrossRef\]](#) [\[PubMed\]](#)
65. Eglitis, R.I.; Piskunov, S.; Popov, A.I.; Purans, J.; Bocharov, D.; Jia, R. Systematic Trends in Hybrid-DFT Computations of  $\text{BaTiO}_3/\text{SrTiO}_3$ ,  $\text{PbTiO}_3/\text{SrTiO}_3$  and  $\text{PbZrO}_3/\text{SrZrO}_3$  (001) Hetero Structures. *Condens. Matter* **2022**, *7*, 70. [\[CrossRef\]](#)
66. Eglitis, R.I.; Purans, J.; Jia, R. Comparative Hybrid Hartree-Fock-DFT Calculations of  $\text{WO}_2$ -Terminated Cubic  $\text{WO}_3$  as Well as  $\text{SrTiO}_3$ ,  $\text{BaTiO}_3$ ,  $\text{PbTiO}_3$  and  $\text{CaTiO}_3$  (001) Surfaces. *Crystals* **2021**, *11*, 455. [\[CrossRef\]](#)
67. Sikam, P.; Thirayatorn, R.; Kaewmaraya, T.; Thongbai, P.; Moontragoon, P.; Ikonc, Z. Improved Thermoelectric Properties of  $\text{SrTiO}_3$  via (La, Dy and N) Co-Doping: DFT Approach. *Molecules* **2022**, *27*, 7923. [\[CrossRef\]](#) [\[PubMed\]](#)
68. Eglitis, R.I.; Jia, R. Review of Systematic Tendencies in (001), (011) and (111) Surfaces Using B3PW as Well as B3LYP Computations of  $\text{BaTiO}_3$ ,  $\text{CaTiO}_3$ ,  $\text{PbTiO}_3$ ,  $\text{SrTiO}_3$ ,  $\text{BaZrO}_3$ ,  $\text{CaZrO}_3$ ,  $\text{PbZrO}_3$  and  $\text{SrZrO}_3$  Perovskites. *Materials* **2023**, *16*, 7623. [\[CrossRef\]](#)
69. Jouybar, S.; Naji, L.; Sarabadani Tafreshi, S.; de Leeuw, N.H. A Density Functional Theory Study of the Physico-Chemical Properties of Alkali Metal Titanate Perovskites for Solar Cell Applications. *Molecules* **2024**, *29*, 3355. [\[CrossRef\]](#) [\[PubMed\]](#)
70. Elegbeleye, I.F.; Maluta, N.E.; Maphanga, R.R. Density Functional Theory Study of Optical and Electronic Properties of  $(\text{TiO}_2)_{n=5,8,68}$  Clusters for Application in Solar Cells. *Molecules* **2021**, *26*, 955. [\[CrossRef\]](#)
71. Yan, Z.; Zhang, Y.; Kang, W.; Deng, N.; Pan, Y.; Sun, W.; Ni, J.; Kang, X.  $\text{TiO}_2$  Gas Sensors Combining Experimental and DFT Calculations: A Review. *Nanomaterials* **2022**, *12*, 3611. [\[CrossRef\]](#)
72. Gustavsen, K.R.; Feng, T.; Huang, H.; Li, G.; Narkiewicz, U.; Wang, K. DFT Calculation of Carbon-Doped  $\text{TiO}_2$  Nanocomposites. *Materials* **2023**, *16*, 6117. [\[CrossRef\]](#)
73. Wang, J.; Zhou, T.; Zhang, Y.; Chen, S.; Bai, J.; Li, J.; Zhou, B. The design of high-performance photoanode of CQDs/ $\text{TiO}_2$ / $\text{WO}_3$  based on DFT alignment of lattice parameter and energy band, and charge distribution. *J. Colloid Interface Sci.* **2021**, *600*, 828–837. [\[CrossRef\]](#)
74. Thongyong, N.; Chanlek, N.; Srepusharawoot, P.; Takesada, M.; Cann, D.P.; Thongbai, P. Experimental study and DFT calculations of improved giant dielectric properties of  $\text{Ni}^{2+}/\text{Ta}^{5+}$  co-doped  $\text{TiO}_2$  by engineering defects and internal interfaces. *J. Eur. Ceram. Soc.* **2022**, *42*, 4944–4952. [\[CrossRef\]](#)

75. Amrhar, O.; Lee, H.S.; Lgaz, H.; Berisha, A.; Ebenso, E.E.; Cho, Y. Computational insights into the adsorption mechanisms of anionic dyes on the rutile TiO<sub>2</sub> (110) surface: Combining SCC-DFT tight binding with quantum chemical and molecular dynamics simulations. *J. Mol. Liq.* **2023**, *377*, 121554. [\[CrossRef\]](#)
76. Zeng, Z.; Wodaczek, F.; Liu, K.; Stein, F.; Hutter, J.; Chen, J.; Cheng, B. Mechanistic insight on water dissociation on pristine low-index TiO<sub>2</sub> surfaces from machine learning molecular dynamics simulations. *Nat. Commun.* **2023**, *14*, 6131. [\[CrossRef\]](#)
77. Boboriko, N.E.; Dzichenka, Y.U. Molecular dynamics simulation as a tool for prediction of the properties of TiO<sub>2</sub> and TiO<sub>2</sub>: MoO<sub>3</sub>-based chemical gas sensors. *J. Alloys Compd.* **2021**, *855*, 157490. [\[CrossRef\]](#)
78. Raffaini, G. Surface chemistry, crystal structure, size, and topography role in the albumin adsorption process on TiO<sub>2</sub> anatase crystallographic faces and its 3D-nanocrystal: A molecular dynamics study. *Coatings* **2021**, *11*, 420. [\[CrossRef\]](#)
79. Maleki, F.; Di Liberto, G.; Pacchioni, G. pH-and facet-dependent surface chemistry of TiO<sub>2</sub> in aqueous environment from first principles. *ACS Appl. Mater. Interfaces* **2023**, *15*, 11216–11224. [\[CrossRef\]](#)
80. Nosaka, Y. Water Photo-Oxidation over TiO<sub>2</sub>—History and Reaction Mechanism. *Catalysts* **2022**, *12*, 1557. [\[CrossRef\]](#)
81. Estévez Ruiz, E.P.; Lago, J.L.; Thirumuruganandham, S.P. Experimental Studies on TiO<sub>2</sub> NT with Metal Dopants through Co-Precipitation, Sol–Gel, Hydrothermal Scheme and Corresponding Computational Molecular Evaluations. *Materials* **2023**, *16*, 3076. [\[CrossRef\]](#)
82. Kydyrbay, N.; Zhazitov, M.; Abdullah, M.; Duisebayev, T.; Tezekbay, Y.; Aldongarov, A.; Karibayev, M.; Nuraje, N.; Toktarbaiuly, O. Structural, surface, and theoretical investigation of hydrophobic-modified nanodiamond powders. *Scientific Reports* **2025**, *15*, 24329. [\[CrossRef\]](#)
83. Yang, M.; Bonati, L.; Polino, D.; Parrinello, M. Using metadynamics to build neural network potentials for reactive events: The case of urea decomposition in water. *Catal. Today* **2022**, *387*, 143–149. [\[CrossRef\]](#)
84. Ismagambetov, O.; Aldiyarov, N.; Almas, N.; Irgibaeva, I.; Baitassova, Z.; Piskunov, S.; Aldongarov, A.; Abdirashev, O. Atomistic Modeling of Natural Gas Desulfurization Process Using Task-Specific Deep Eutectic Solvents Supported by Graphene Oxide. *Molecules* **2024**, *29*, 5282. [\[CrossRef\]](#)
85. Nulimu, A.; Aldongarov, A.; Sarsenova, S.; Ibrayeva, A.; Karibayev, M. Unraveling the Role of Functional Groups in Polyaniline for Ammonia Sensing: A Theoretical Approach. *Engineered Science* **2025**, *36*, 1616. [\[CrossRef\]](#)
86. Yao, N.; Chen, X.; Fu, Z.H.; Zhang, Q. Applying classical, ab initio, and machine-learning molecular dynamics simulations to the liquid electrolyte for rechargeable batteries. *Chem. Rev.* **2022**, *122*, 10970–11021. [\[CrossRef\]](#)
87. Chen, Y.; Liu, Y.; Xu, Y.; Guo, X.; Cao, Y.; Ming, W. Review: Modeling and Simulation of Membrane Electrode Material Structure for Proton Exchange Membrane Fuel Cells. *Coatings* **2022**, *12*, 1145. [\[CrossRef\]](#)
88. Samantaray, S.; Mohanty, D.; Satpathy, S.K.; Hung, I.-M. Exploring Recent Developments in Graphene-Based Cathode Materials for Fuel Cell Applications: A Comprehensive Overview. *Molecules* **2024**, *29*, 2937. [\[CrossRef\]](#)
89. Shah, D.; Karibayev, M.; Adotey, E.K.; Amouei Torkmahalleh, M. Impact of Volatile Organic Compounds on Chromium Containing Atmospheric Particulate: Insights from Molecular Dynamics Simulations. *Sci. Rep.* **2020**, *10*, 17387. [\[CrossRef\]](#)
90. Wang, W.; Qu, Z.; Wang, X.; Zhang, J. A Molecular Model of PEMFC Catalyst Layer: Simulation on Reactant Transport and Thermal Conduction. *Membranes* **2021**, *11*, 148. [\[CrossRef\]](#)
91. Chen, X.; Hou, W.; Zhai, F.; Cheng, J.; Yuan, S.; Li, Y.; Wang, N.; Zhang, L.; Ren, J. Reversible Hydrogen Storage Media by g-CN Monolayer Decorated with NLi<sub>4</sub>: A First-Principles Study. *Nanomaterials* **2023**, *13*, 647. [\[CrossRef\]](#)
92. Li, Q.; Li, Q.; Wang, F.; Wu, J.; Wang, Y. The Carrying Behavior of Water-Based Fracturing Fluid in Shale Reservoir Fractures and Molecular Dynamics of Sand-Carrying Mechanism. *Processes* **2024**, *12*, 2051. [\[CrossRef\]](#)
93. Karibayev, M.; Shah, D. Comprehensive Computational Analysis Exploring the Formation of Caprolactam-Based Deep Eutectic Solvents and Their Applications in Natural Gas Desulfurization. *Energy Fuels* **2020**, *34*, 9894–9902. [\[CrossRef\]](#)
94. Shelyapina, M.G. Hydrogen Diffusion on, into and in Magnesium Probed by DFT: A Review. *Hydrogen* **2022**, *3*, 285–302. [\[CrossRef\]](#)
95. Mutisya, S.M.; Kalinichev, A.G. Carbonation reaction mechanisms of portlandite predicted from enhanced Ab Initio molecular dynamics simulations. *Minerals* **2021**, *11*, 509. [\[CrossRef\]](#)
96. Kohmuan, P.; Inthomya, W.; Wongkoblap, A.; Tangsathitkulchai, C. Monte Carlo Simulation and Experimental Studies of CO<sub>2</sub>, CH<sub>4</sub> and Their Mixture Capture in Porous Carbons. *Molecules* **2021**, *26*, 2413. [\[CrossRef\]](#)
97. Torkmahalleh, M.A.; Karibayev, M.; Konakbayeva, D.; Fyrrillas, M.M.; Rule, A.M. Aqueous Chemistry of Airborne Hexavalent Chromium during Sampling. *Air Qual. Atmos. Health* **2018**, *11*, 1059–1068. [\[CrossRef\]](#)
98. Dong, K.; Niu, Z.; Kong, S.; Jia, B. Impact of Supercritical Carbon Dioxide on Pore Structure and Gas Transport in Bituminous Coal: An Integrated Experiment and Simulation. *Molecules* **2025**, *30*, 1200. [\[CrossRef\]](#) [\[PubMed\]](#)
99. Filipe, H.A.L.; Loura, L.M.S. Molecular Dynamics Simulations: Advances and Applications. *Molecules* **2022**, *27*, 2105. [\[CrossRef\]](#)
100. Smith, A.; Dong, X.; Raghavan, V. An Overview of Molecular Dynamics Simulation for Food Products and Processes. *Processes* **2022**, *10*, 119. [\[CrossRef\]](#)



101. Celik, I.; Yadav, R.; Duzgun, Z.; Albogami, S.; El-Shehawi, A.M.; Fatimawali; Idroes, R.; Tallei, T.E.; Emran, T.B. Interactions of the Receptor Binding Domain of SARS-CoV-2 Variants with hACE2: Insights from Molecular Docking Analysis and Molecular Dynamic Simulation. *Biology* **2021**, *10*, 880. [\[CrossRef\]](#)
102. SdfLiu, W.D.; Yu, Y.; Dargusch, M.; Liu, Q.; Chen, Z.G. Carbon allotrope hybrids advance thermoelectric development and applications. *Renew. Sustain. Energy Rev.* **2021**, *141*, 110800. [\[CrossRef\]](#)
103. Zhang, Y.Q.; Liu, Y.J.; Liu, Y.L.; Zhao, J.X. Boosting sensitivity of Boron Nitride Nanotube (BNNT) to nitrogen dioxide by Fe encapsulation. *J. Mol. Graph. Model.* **2014**, *51*, 1–6. [\[CrossRef\]](#)
104. Rodríguez-Quintana, R.; Carbajal-Franco, G.; Rojas-Chávez, H. DFT study of the H<sub>2</sub> molecules adsorption on pristine and Ni doped graphite surfaces. *Mater. Lett.* **2021**, *293*, 129660. [\[CrossRef\]](#)
105. Zhang, W.-S.; Liu, Y.-T.; Yao, T.-T.; Wu, G.-P.; Liu, Q. Oxygen defect engineering toward the length-selective tailoring of carbon nanotubes via a two-step electrochemical strategy. *J. Phys. Chem. C* **2020**, *124*, 27097–27106. [\[CrossRef\]](#)
106. Elias, A.; Uddin, N.; Hossain, A.; Saha, J.K.; Siddiquey, I.A.; Sarker, D.R.; Diba, Z.R.; Uddin, J.; Choudhury, M.H.R.; Firoz, S.H. An experimental and theoretical study of the effect of Ce doping in ZnO/CNT composite thin film with enhanced visible light photo-catalysis. *Int. J. Hydrogen Energy* **2019**, *44*, 20068–20078. [\[CrossRef\]](#)
107. Liu, Y.; Zhang, H.; Zhang, Z.; Jia, X.; An, L. CO adsorption on Fe-doped vacancy-defected CNTs—A DFT study. *Chem. Phys. Lett.* **2019**, *730*, 316–320. [\[CrossRef\]](#)
108. Myrzakhmetov, B.; Karibayev, M.; Wang, Y.; Mentbayeva, A. Density functional theory investigation of intermolecular interactions for hydrogen-bonded deep eutectic solvents. *Eurasian Chem.-Technol. J.* **2024**, *26*, 29–36. [\[CrossRef\]](#)
109. Xu, J.; Wan, Q.; Anpo, M.; Lin, S. Bandgap opening of graphdiyne monolayer via B, N-codoping for photocatalytic overall water splitting: Design strategy from DFT studies. *J. Phys. Chem. C* **2020**, *124*, 6624–6633. [\[CrossRef\]](#)
110. Loh, G.; Pandey, R.; Yap, Y.K.; Karna, S.P. MoS<sub>2</sub> quantum dot: Effects of passivation, additional layer, and h-BN substrate on its stability and electronic properties. *J. Phys. Chem. C* **2015**, *119*, 1565–1574. [\[CrossRef\]](#)
111. Pandey, D.; Kumar, A.; Chakrabarti, A.; Pandey, R. Stacking-dependent electronic properties of aluminene based multilayer van der Waals heterostructures. *Comput. Mater. Sci.* **2020**, *185*, 109952. [\[CrossRef\]](#)
112. Lin, Y.-P.; Bocharov, D.; Isakoviča, I.; Pankratov, V.; Popov, A.A.; Popov, A.I.; Piskunov, S. Chlorine Adsorption on TiO<sub>2</sub>(110)/Water Interface: Nonadiabatic Molecular Dynamics Simulations for Photocatalytic Water Splitting. *Electron. Mater.* **2023**, *4*, 33–48. [\[CrossRef\]](#)
113. Tada, K.; Sakata, K.; Yamada, S.; Okazaki, K.; Kitagawa, Y.; Kawakami, T.; Yamanaka, S.; Okumura, M. DFT calculations for Au adsorption onto a reduced TiO<sub>2</sub> (110) surface with the coexistence of Cl. *Mol. Phys.* **2014**, *112*, 365–378. [\[CrossRef\]](#)
114. Li, Y.; Gao, D.; Peng, S.; Lu, G.; Li, S. Photocatalytic hydrogen evolution over Pt/Cd<sub>0.5</sub>Zn<sub>0.5</sub>S from saltwater using glucose as electron donor: An investigation of the influence of electrolyte NaCl. *Int. J. Hydrogen Energy* **2011**, *36*, 4291–4297. [\[CrossRef\]](#)
115. Alghamdi, H.; Idriss, H. Study of the modes of adsorption and electronic structure of hydrogen peroxide and ethanol over TiO<sub>2</sub> rutile (110) surface within the context of water splitting. *Surf. Sci.* **2018**, *669*, 103–113. [\[CrossRef\]](#)
116. Vu, N.H.; Le, H.V.; Cao, T.M.; Pham, V.V.; Le, H.M.; Nguyen-Manh, D. Anatase–rutile phase transformation of titanium dioxide bulk material: A DFT+U approach. *J. Phys. Condens. Matter* **2012**, *24*, 405501. [\[CrossRef\]](#)
117. Kolesov, G.; Grånäs, O.; Hoyt, R.; Vinichenko, D.; Kaxiras, E. Real-time TD-DFT with classical ion dynamics: Methodology and applications. *J. Chem. Theory Comput.* **2016**, *12*, 466–476. [\[CrossRef\]](#)
118. You, P.; Chen, D.; Lian, C.; Zhang, C.; Meng, S. First-principles dynamics of photoexcited molecules and materials towards a quantum description. *Wiley Interdiscip. Rev. Comput. Mol. Sci.* **2021**, *11*, e1492. [\[CrossRef\]](#)
119. Pham, T.A.; Ping, Y.; Galli, G. Modelling heterogeneous interfaces for solar water splitting. *Nat. Mater.* **2017**, *16*, 401–408. [\[CrossRef\]](#)
120. Agosta, L.; Brandt, E.G.; Lyubartsev, A.P. Diffusion and reaction pathways of water near fully hydrated TiO<sub>2</sub> surfaces from ab initio molecular dynamics. *J. Chem. Phys.* **2017**, *147*, 024704. [\[CrossRef\]](#)
121. Balzaretti, F.; Gupta, V.; Ciacchi, L.C.; Aradi, B.; Frauenheim, T.; Köppen, S. Water reactions on reconstructed rutile TiO<sub>2</sub>: A density functional theory/density functional tight binding approach. *J. Phys. Chem. C* **2021**, *125*, 13234–13246. [\[CrossRef\]](#)
122. Gao, M.; Connor, P.K.N.; Ho, G.W. Plasmonic photothermic directed broadband sunlight harnessing for seawater catalysis and desalination. *Energy Environ. Sci.* **2016**, *9*, 3151–3160. [\[CrossRef\]](#)
123. Schilling, M.; Lubner, S. Computational Modeling of Cobalt-Based Water Oxidation: Current Status and Future Challenges. *Front. Chem.* **2018**, *6*, 100. [\[CrossRef\]](#)
124. VandeVondele, J.; Mohamed, F.; Krack, M.; Hutter, J.; Sprik, M.; Parrinello, M. The influence of temperature and density functional models in ab initio molecular dynamics simulation of liquid water. *J. Chem. Phys.* **2005**, *122*, 014515. [\[CrossRef\]](#)
125. Sinha, V.; Govindarajan, N.; de Bruin, B.; Meijer, E.J. How Solvent Affects C–H Activation and Hydrogen Production Pathways in Homogeneous Ru-Catalyzed Methanol Dehydrogenation Reactions. *ACS Catal.* **2018**, *8*, 6908–6913. [\[CrossRef\]](#)
126. Cheng, J.; Liu, X.; VandeVondele, J.; Sulpizi, M.; Sprik, M. Redox Potentials and Acidity Constants from Density Functional Theory Based Molecular Dynamics. *Acc. Chem. Res.* **2014**, *47*, 3522–3529. [\[CrossRef\]](#)



127. Liu, X.; Jiang, B.; Liu, Y.; Liu, L.; Xia, T.; Zhang, X.; Ye, C.; Yu, Y.; Wang, B. Two-Dimensional As/BlueP van der Waals Hetero-Structure as a Promising Photocatalyst for Water Splitting: A DFT Study. *Coatings* **2020**, *10*, 1160. [\[CrossRef\]](#)
128. Singh, A.K.; Mathew, K.; Zhuang, H.L.; Henning, R.G. Computational screening of 2D materials for photocatalysis. *J. Phys. Chem. Lett.* **2015**, *6*, 1087–1098. [\[CrossRef\]](#) [\[PubMed\]](#)
129. Ma, X.G.; Lv, Y.H.; Xu, J.; Liu, Y.F.; Zhang, R.Q.; Zhu, Y.F. A strategy of enhancing the photoactivity of g-C<sub>3</sub>N<sub>4</sub> via doping of nonmetal elements: A first-principles study. *J. Phys. Chem. C* **2012**, *116*, 23485–23493. [\[CrossRef\]](#)
130. Li, G.; Zhao, Y.C.; Zeng, S.M.; Ni, J. The realization of half-metal and spin-semiconductor for metal adatoms on arsenene. *Appl. Surf. Sci.* **2016**, *390*, 60–67. [\[CrossRef\]](#)
131. Li, X.H.; Wang, B.J.; Cai, X.L.; Zhang, L.W.; Wang, G.D.; Ke, S.H. Tunable electronic properties of arsenene/GaS van der Waals heterostructures. *RSC Adv.* **2017**, *7*, 28393. [\[CrossRef\]](#)
132. Fang, L.Z.; Li, X.P.; Geng, Z.D.; Wang, T.X.; Xia, C.X. Band alignment tuning in GeS/arsenene staggered hetero-structures. *J. Alloy. Compd.* **2019**, *793*, 283–288. [\[CrossRef\]](#)
133. Jamdagni, P.; Thakur, A.; Kumar, A.; Ahluwalia, P.K.; Pandey, R. Two dimensional allotropes of arsenene with a wide range of high and anisotropic carrier mobility. *Phys. Chem. Chem. Phys.* **2018**, *20*, 29939. [\[CrossRef\]](#)
134. Wang, B.J.; Li, X.H.; Cai, X.L.; Yu, W.Y.; Zhang, L.W.; Zhao, R.Q.; Ke, S.H. Blue Phosphorus/Mg(OH)<sub>2</sub> van der Waals hetero-structures as Promising Visible-Light Photocatalysts for Water Splitting. *J. Phys. Chem. C* **2018**, *122*, 7075–7080. [\[CrossRef\]](#)
135. Li, Q.F.; Ma, X.F.; Lei, Z.; Wan, X.G.; Rao, W.F. Theoretical design of blue phosphorene/arsenene lateral heterostructures with superior electronic properties. *J. Phys. D Appl. Phys.* **2018**, *51*, 255304. [\[CrossRef\]](#)
136. Inerbaev, T.M.; Graupner, D.R.; Abuova, A.U.; Abuova, F.U.; Kilin, D.S. Optical properties of BaTiO<sub>3</sub> at room temperature: DFT modelling. *RSC Adv.* **2025**, *15*, 5405–5412. [\[CrossRef\]](#)
137. Ogunkunle, S.A.; Mortier, F.; Bouzid, A.; Hinsch, J.J.; Zhang, L.; Wu, Z.; Bernard, S.; Zhu, Y.; Wang, Y. Navigating Alkaline Hydrogen Evolution Reaction Descriptors for Electrocatalyst Design. *Catalysts* **2024**, *14*, 608. [\[CrossRef\]](#)
138. Miran, H.A.; Jaf, Z.N.; Altarawneh, M.; Jiang, Z.-T. An Insight into Geometries and Catalytic Applications of CeO<sub>2</sub> from a DFT Outlook. *Molecules* **2021**, *26*, 6485. [\[CrossRef\]](#) [\[PubMed\]](#)
139. Yang, C.; Chen, Y.; Chen, T.; Rajendran, S.; Zeng, Z.; Qin, J.; Zhang, X. A long-standing polarized electric field in TiO<sub>2</sub>@BaTiO<sub>3</sub>/CdS nanocomposite for effective photocatalytic hydrogen evolution. *Fuel* **2021**, *314*, 122758. [\[CrossRef\]](#)
140. Cai, W.; Ma, X.; Chen, J.; Shi, R.; Wang, Y.; Yang, Y.; Jing, D.; Yuan, H.; Du, J.; Que, M. Synergy of oxygen vacancy and piezoelectricity effect promotes the CO<sub>2</sub> photoreduction by BaTiO<sub>3</sub>. *Appl. Surf. Sci.* **2023**, *619*, 156773. [\[CrossRef\]](#)
141. Wang, M.; Wang, C.; Liu, Y.; Zhou, X. Hybrid density functional theory description of non-metal doping in perovskite BaTiO<sub>3</sub> for visible-light photocatalysis. *J. Solid State Chem.* **2019**, *280*, 121018. [\[CrossRef\]](#)
142. Rizwan, M.; Hajra, N.; Zeba, I.; Shakil, M.; Gillani, S.; Usman, Z. Electronic, structural, and optical properties of BaTiO<sub>3</sub> doped with lanthanum (La): Insight from DFT calculation. *Optik* **2020**, *211*, 164611. [\[CrossRef\]](#)
143. Xu, H.; Wang, P.; Luan, S.; Cheng, L.; Fu, Z.; Cao, X.; Zhang, L.; Yu, S.; Sun, R. Vacancy engineering for high tetragonal BaTiO<sub>3</sub> synthesized by solid-state approaches. *Powder Technol.* **2024**, *444*, 119955. [\[CrossRef\]](#)
144. Xie, P.; Yang, F.; Li, R.; Ai, C.; Lin, C.; Lin, S. Improving hydrogen evolution activity of perovskite BaTiO<sub>3</sub> with Mo doping: Experiments and first-principles analysis. *Int. J. Hydrogen Energy* **2019**, *44*, 11695–11704. [\[CrossRef\]](#)
145. Usman, M.; Rehman, J.U.; Tahir, M.B.; Hussain, A. First-principles calculations to investigate the effect of Cs-doping in BaTiO<sub>3</sub> for water-splitting application. *Solid State Commun.* **2022**, *355*, 114920. [\[CrossRef\]](#)
146. Chun, H.; Lee, Y.; Kim, S.; Yoon, Y.; Kim, Y.; Park, S. Surface termination of BaTiO<sub>3</sub>(111) single crystal: A combined DFT and XPS study. *Appl. Surf. Sci.* **2021**, *578*, 152018. [\[CrossRef\]](#)
147. Dahbi, S.; Tahiri, N.; Bounagui, O.E.; Ez-Zahraouy, H. Effects of oxygen group elements on thermodynamic stability, electronic structures, and optical properties of the pure and pressed BaTiO<sub>3</sub> perovskite. *Comput. Condens. Matter* **2022**, *32*, e00728. [\[CrossRef\]](#)
148. Dahbi, S.; Tahiri, N.; Bounagui, O.E.; Ez-Zahraouy, H. Electronic, optical, and thermoelectric properties of perovskite BaTiO<sub>3</sub> compound under the effect of compressive strain. *Chem. Phys.* **2021**, *544*, 111105. [\[CrossRef\]](#)
149. Fo, Y.; Zhou, X. A theoretical study on tetragonal BaTiO<sub>3</sub> modified by surface co-doping for photocatalytic overall water splitting. *Int. J. Hydrogen Energy* **2022**, *47*, 19073–19085. [\[CrossRef\]](#)
150. Jensen, S.J.; Inerbaev, T.M.; Abuova, A.U.; Kilin, D.S. Spin unrestricted nonradiative relaxation dynamics of cobalt-doped anatase nanowire. *J. Phys. Chem. C* **2017**, *121*, 16110–16125. [\[CrossRef\]](#)
151. Bhat, D.K.; Bantawal, H.; Pi, U.; Shenoy, U.S. Enhanced photoresponse and efficient charge transfer in porous graphene-BaTiO<sub>3</sub> nanocomposite for high-performance photocatalysis. *Diam. Relat. Mater.* **2023**, *139*, 110312. [\[CrossRef\]](#)
152. Bashir, M.Z.; Naqvi, S.A.Z.; Naeem, M.A.; Munir, R.; Noreen, S. Theoretical study of optoelectronic, elastic, and mechanical properties of gallium-modified barium titanate (Ba<sub>1-x</sub>Ga<sub>x</sub>TiO<sub>3</sub>) perovskite ceramics by DFT. *Mater. Sci. Semicond. Process.* **2024**, *182*, 108734. [\[CrossRef\]](#)
153. Wang, S.; Ge, K.; Cui, H.; Li, S.; Yang, Y.; Pan, M.; Zhu, L. Self-polarization-enhanced oxygen evolution reaction by flower-like core-shell BaTiO<sub>3</sub>@NiFe-layered double hydroxide heterojunctions. *Chem. Eng. J.* **2023**, *479*, 147831. [\[CrossRef\]](#)

154. Chen, G.; Ji, Y.; Shi, X.; An, P.; Zhang, J.; Li, Y.; Liu, S.F.; Yan, J. Oxygen-deficient BaTiO<sub>3</sub> loading sub-nm PtO<sub>x</sub> for photocatalytic biological wastewater splitting to green hydrogen production. *Chem. Eng. J.* **2024**, *496*, 154261. [\[CrossRef\]](#)
155. Guo, M.; Zhong, J.; Li, W.; Hou, H.; Bowen, C.R.; Zhan, X.; Yang, H.; Yang, M.; Chen, Z.; Chen, D.; et al. Highly efficient photocatalytic hydrogen evolution enabled by piezotronic effects in SrTiO<sub>3</sub>/BaTiO<sub>3</sub> nanofiber heterojunctions. *Nano Energy* **2024**, *127*, 109745. [\[CrossRef\]](#)
156. Zulfiqar, W.; Alay-e-Abbas, S.M. Improved thermodynamic stability and visible light absorption in Zr+X codoped (X = S, Se, and Te) BaTiO<sub>3</sub> photocatalysts: A first-principles study. *Mater. Today Commun.* **2022**, *32*, 103867. [\[CrossRef\]](#)
157. Kovač, I.; Mužević, M.; Pajtler, M.V.; Lukačević, I. Charge carrier dynamics across the metal oxide/BaTiO<sub>3</sub> interfaces toward photovoltaic applications from the theoretical perspective. *Surf. Interfaces* **2023**, *39*, 102974. [\[CrossRef\]](#)
158. Kaptagay, G.A.; Satanova, B.M.; Abuova, A.U.; Konuhova, M.; Zakiyeva, Z.; Tolegen, U.Z.; Koilyk, N.O.; Abuova, F.U. Effect of rhodium doping for photocatalytic activity of barium titanate. *Opt. Mater. X* **2025**, *25*, 100382. [\[CrossRef\]](#)
159. Opoku, F.; Akoto, O.; Kwaansa-Ansah, E.E.; Asare-Donkor, N.K.; Adimado, A.A. Role of BaTiO<sub>3</sub> crystal surfaces on the electronic properties, charge separation, and visible light-response of the most active (001) surface of LaAlO<sub>3</sub>: A hybrid density functional study. *Chem. Phys. Impact* **2023**, *6*, 100236. [\[CrossRef\]](#)
160. Abbasi, P.; Barone, M.R.; Cruz-Jáuregui, M.d.I.P.; Valdespino-Padilla, D.; Paik, H.; Kim, T.; Kornblum, L.; Schlom, D.G.; Pascal, T.A.; Fenning, D.P. Ferroelectric Modulation of Surface Electronic States in BaTiO<sub>3</sub> for Enhanced Hydrogen Evolution Activity. *Nano Lett.* **2022**, *22*, 4276–4284. [\[CrossRef\]](#)
161. Gunawan, M.; Bowdler, O.; Zhou, S.; Fang, X.; Zhang, Q.; Sakamoto, Y.; Sun, K.; Gunawan, D.; Chang, S.L.; Amal, R.; et al. Ferroelectric Polarization-Induced Performance Enhancements in BiFeO<sub>3</sub>/BiVO<sub>4</sub> Photoanodes for Photoelectrochemical Water Splitting. *Adv. Funct. Mater.* **2025**, *35*, 2417651. [\[CrossRef\]](#)
162. Goumri-Said, S.; Kanoun, M.B. Insight into the Effect of Anionic–Anionic Co-Doping on BaTiO<sub>3</sub> for Visible Light Photocatalytic Water Splitting: A First-Principles Hybrid Computational Study. *Catalysts* **2022**, *12*, 1672. [\[CrossRef\]](#)
163. Chandrappa, S.; Galbao, S.J.; Krishnan, P.S.S.R.; Koshi, N.A.; Das, S.; Myakala, S.N.; Lee, S.; Dutta, A.; Cherevan, A.; Bhattacharjee, S.; et al. Iridium-Doping as a Strategy to Realize Visible-Light Absorption and P-Type Behavior in BaTiO<sub>3</sub>. *J. Phys. Chem. C* **2023**, *127*, 12383–12393. [\[CrossRef\]](#)
164. Bhat, D.K.; Bantawal, H.; Shenoy, U.S. Rhodium Doping Augments Photocatalytic Activity of Barium Titanate: Effect of Electronic Structure Engineering. *Nanoscale Adv.* **2020**, *2*, 5688–5698. [\[CrossRef\]](#)
165. Qiu, H.; Yang, T.; Zhou, J.; Yang, K.; Ying, Y.; Ding, K.; Yang, M.; Huang, H. Tunable Hydrogen Evolution Activity by Modulating Polarization States of Ferroelectric BaTiO<sub>3</sub>. *J. Mater. Chem. A* **2023**, *11*, 7034–7042. [\[CrossRef\]](#)
166. Wang, Y.; Zhou, Q.; Zhang, Q.; Ren, Y.; Cui, K.; Cheng, C.; Wu, K. Effects of La-N Co-Doping of BaTiO<sub>3</sub> on Its Electron-Optical Properties for Photocatalysis: A DFT Study. *Molecules* **2024**, *29*, 2250. [\[CrossRef\]](#)
167. Saadon, N.M.Q.; Miran, H.A. Optoelectronic Tuning of Barium Titanate Doped with Pt: A Systematic First-Principles Study. *Pap. Phys.* **2024**, *16*, 160002. [\[CrossRef\]](#)
168. Sharma, D.; Upadhyay, S.; Satsangi, V.R.; Shrivastav, R.; Waghmare, U.V.; Dass, S. Nanostructured BaTiO<sub>3</sub>/Cu<sub>2</sub>O Heterojunction with Improved Photoelectrochemical Activity for H<sub>2</sub> Evolution: Experimental and First-Principles Analysis. *Appl. Catal. B Environ.* **2016**, *189*, 75–85. [\[CrossRef\]](#)
169. Inerbaev, T.; Akilbekov, A.; Kenbayev, D.; Dauletbekova, A.; Shalaev, A.; Polisadova, E.; Konuhova, M.; Piskunov, S.; Popov, A.I. Color Centers in BaFBr Crystals: Experimental Study and Theoretical Modeling. *Materials* **2024**, *17*, 3340. [\[CrossRef\]](#)
170. Tymieńska, N.; Wu, G.; Dupuis, M. Water Oxidation on Oxygen-Deficient Barium Titanate: A First-Principles Study. *J. Phys. Chem. C* **2017**, *121*, 8378–8389. [\[CrossRef\]](#)
171. Fan, X.T.; Wen, X.J.; Zhuang, Y.B.; Cheng, J. Molecular insight into the GaP (110)-water interface using machine learning accelerated molecular dynamics. *J. Energy Chem.* **2023**, *82*, 239–247. [\[CrossRef\]](#)
172. Miao, L.; Jia, W.; Cao, X.; Jiao, L. Computational chemistry for water-splitting electrocatalysis. *Chem. Soc. Rev.* **2024**, *53*, 2771–2807. [\[CrossRef\]](#)
173. Zhang, M.; Hou, Y.C.; Jiang, Y.; Ni, X.; Wang, Y.; Zou, X. Rational design of water splitting electrocatalysts through computational insights. *Chem. Commun.* **2024**, *60*, 14521–14536. [\[CrossRef\]](#)
174. Orhan, I.B.; Zhao, Y.; Babarao, R.; Thornton, A.W.; Le, T.C. Machine Learning Descriptors for CO<sub>2</sub> Capture Materials. *Molecules* **2025**, *30*, 650. [\[CrossRef\]](#)
175. Ma, K.; Yang, C.; Zhang, J.; Li, Y.; Jiang, G.; Chai, J. Machine Learning-Assisted Hartree–Fock Approach for Energy Level Calculations in the Neutral Ytterbium Atom. *Entropy* **2024**, *26*, 962. [\[CrossRef\]](#)
176. Tereshchenko, A.; Pashkov, D.; Guda, A.; Guda, S.; Rusalev, Y.; Soldatov, A. Adsorption Sites on Pd Nanoparticles Unraveled by Machine-Learning Potential with Adaptive Sampling. *Molecules* **2022**, *27*, 357. [\[CrossRef\]](#)
177. Biswas, M.; Desai, R.; Mannodi-Kanakithodi, A. Screening of novel halide perovskites for photocatalytic water splitting using multi-fidelity machine learning. *Phys. Chem. Chem. Phys.* **2024**, *26*, 23177–23188. [\[CrossRef\]](#)

178. Allam, O.; Maghsoodi, M.; Jang, S.S.; Snow, S.D. Unveiling competitive adsorption in TiO<sub>2</sub> photocatalysis through machine-learning-accelerated molecular dynamics, DFT, and experimental methods. *ACS Appl. Mater. Interfaces* **2024**, *16*, 36215–36223. [\[CrossRef\]](#)
179. Agrawal, S.; Wang, B.; Wu, Y.; Casanova, D.; Prezhdo, O.V. Photocatalytic activity of dual defect modified graphitic carbon nitride is robust to tautomerism: Machine learning assisted ab initio quantum dynamics. *Nanoscale* **2024**, *16*, 8986–8995. [\[CrossRef\]](#)
180. Gao, Y.; Zhang, Q.; Hu, W.; Yang, J. First-principles computational screening of two-dimensional polar materials for photocatalytic water splitting. *ACS Nano* **2024**, *18*, 19381–19390. [\[CrossRef\]](#)
181. Raman, A.S.; Vojvodic, A. Providing atomistic insights into the dissolution of rutile oxides in electrocatalytic water splitting. *J. Phys. Chem. C* **2022**, *126*, 922–932. [\[CrossRef\]](#)
182. Li, Z.; Wang, J.; Yang, C.; Liu, L.; Yang, J.Y. Thermal transport across TiO<sub>2</sub>–H<sub>2</sub>O interface involving water dissociation: Ab initio-assisted deep potential molecular dynamics. *J. Chem. Phys.* **2023**, *159*, 144701. [\[CrossRef\]](#)
183. Jia, M.; Zhuang, Y.B.; Wang, F.; Zhang, C.; Cheng, J. Water-mediated proton hopping mechanisms at the SnO<sub>2</sub> (110)/H<sub>2</sub>O interface from ab initio deep potential molecular dynamics. *Precis. Chem.* **2024**, *2*, 644–654. [\[CrossRef\]](#)
184. Schienbein, P.; Blumberger, J. Data-Efficient Active Learning for Thermodynamic Integration: Acidity Constants of BiVO<sub>4</sub> in Water. *ChemPhysChem* **2025**, *26*, e202400490. [\[CrossRef\]](#)
185. Park, H.; Kim, Y.; Choi, S.; Kim, H.J. Data-driven computational design of stable oxygen evolution catalysts by DFT and machine learning: Promising electrocatalysts. *J. Energy Chem.* **2024**, *91*, 645–655. [\[CrossRef\]](#)
186. Wang, W.; Zhang, M.; Li, X.; Zhang, S.; Yu, F.; Li, S.; Comini, E.; Wang, Z.L.; Ren, K. Boosting efficiency in piezo-photocatalysis process using POLED Ba<sub>0.7</sub>Sr<sub>0.3</sub>TiO<sub>3</sub> nanorod arrays for pollutant degradation and hydrogen production. *ACS Appl. Mater. Interfaces* **2024**, *16*, 20497–20509. [\[CrossRef\]](#)
187. Shao, Y.; de Ruiter, J.M.; de Groot, H.J.M.; Buda, F. Photocatalytic Water Splitting Cycle in a Dye-Catalyst Supramolecular Complex: Ab Initio Molecular Dynamics Simulations. *J. Phys. Chem. C* **2019**, *123*, 21403–21414. [\[CrossRef\]](#)
188. Zhang, S.; Ye, H.; Hua, J.; Tian, H. Recent Advances in Dye-Sensitized Photoelectrochemical Cells for Water Splitting. *EnergyChem* **2019**, *1*, 100015. [\[CrossRef\]](#)
189. Nada, H.; Kobayashi, M.; Kakihana, M. Anisotropy in Conformation and Dynamics of a Glycolate Ion Near the Surface of a TiO<sub>2</sub> Rutile Crystal Between Its {001} and {110} Planes: A Molecular Dynamics Study. *J. Phys. Chem. C* **2016**, *120*, 6502–6514. [\[CrossRef\]](#)
190. YazdanYar, A.; Aschauer, U.; Bowen, P. Interaction of Biologically Relevant Ions and Organic Molecules with Titanium Oxide (Rutile) Surfaces: A Review on Molecular Dynamics Studies. *Colloids Surf. B Biointerfaces* **2018**, *161*, 563–577. [\[CrossRef\]](#)
191. Harmon, K.J.; Chen, Y.; Bylaska, E.J.; Catalano, J.G.; Bedzyk, M.J.; Weare, J.H.; Fenter, P. Insights on the Alumina–Water Interface Structure by Direct Comparison of Density Functional Simulations with X-ray Reflectivity. *J. Phys. Chem. C* **2018**, *122*, 26934–26944. [\[CrossRef\]](#)
192. Biriukov, D.; Kroutil, O.; Předota, M. Modeling of Solid–Liquid Interfaces Using Scaled Charges: Rutile (110) Surfaces. *Phys. Chem. Chem. Phys.* **2018**, *20*, 23954–23966. [\[CrossRef\]](#)
193. Futera, Z.; English, N.J. Exploring Rutile (110) and Anatase (101) TiO<sub>2</sub> Water Interfaces by Reactive Force-Field Simulations. *J. Phys. Chem. C* **2017**, *121*, 6701–6711. [\[CrossRef\]](#)
194. Cheng, J.; Sprik, M. Aligning Electronic Energy Levels at the TiO<sub>2</sub>/H<sub>2</sub>O Interface. *Phys. Rev. B* **2010**, *82*, 081406. [\[CrossRef\]](#)
195. Asproulis, N.; Drikakis, D. An Artificial Neural Network-Based Multiscale Method for Hybrid Atomistic-Continuum Simulations. *Microfluid. Nanofluidics* **2013**, *15*, 559–574. [\[CrossRef\]](#)
196. Smith, E.R.; Müller, E.A.; Craster, R.V.; Matar, O.K. A Langevin Model for Fluctuating Contact Angle Behaviour Parametrised Using Molecular Dynamics. *Soft Matter* **2016**, *12*, 9604–9615. [\[CrossRef\]](#)
197. Smith, E.R.; Theodorakis, P.E.; Craster, R.V.; Matar, O.K. Moving Contact Lines: Linking Molecular Dynamics and Continuum-Scale Modeling. *Langmuir* **2018**, *34*, 12501–12518. [\[CrossRef\]](#) [\[PubMed\]](#)
198. Zhang, X.; Bieberle-Hütter, A. Modeling and Simulations in Photoelectrochemical Water Oxidation: From Single Level to Multiscale Modeling. *ChemSusChem* **2016**, *9*, 1223–1242. [\[CrossRef\]](#)
199. Jung, C.K.; Braunwarth, L.; Jacob, T. Grand Canonical ReaxFF Molecular Dynamics Simulations for Catalytic Reactions. *J. Chem. Theory Comput.* **2019**, *15*, 5810–5816. [\[CrossRef\]](#) [\[PubMed\]](#)
200. Islam, M.M.; Kolesov, G.; Verstraelen, T.; Kaxiras, E.; van Duin, A.C.T. EReaxFF: A Pseudoclassical Treatment of Explicit Electrons within Reactive Force Field Simulations. *J. Chem. Theory Comput.* **2016**, *12*, 3463–3472. [\[CrossRef\]](#) [\[PubMed\]](#)
201. Tranca, D.C.; Zimmerman, P.M.; Gomes, J.; Lambrecht, D.; Keil, F.J.; Head-Gordon, M.; Bell, A.T. Hexane Cracking on ZSM-5 and Faujasite Zeolites: A QM/MM/QCT Study. *J. Phys. Chem. C* **2015**, *119*, 28836–28853. [\[CrossRef\]](#)
202. Rusevich, L.L.; Kotomin, E.A.; Zvejniece, G.; Popov, A.I. Ab initio calculations of structural, electronic and vibrational properties of BaTiO<sub>3</sub> and SrTiO<sub>3</sub> perovskite crystals with oxygen vacancies. *Low Temp. Phys.* **2020**, *46*, 1185–1195. [\[CrossRef\]](#)
203. Eglitis, R.; Purans, J.; Popov, A.I.; Jia, R. Systematic trends in YAlO<sub>3</sub>, SrTiO<sub>3</sub>, BaTiO<sub>3</sub>, BaZrO<sub>3</sub> (001) and (111) surface ab initio calculations. *Int. J. Mod. Phys. B* **2019**, *33*, 1950390. [\[CrossRef\]](#)

204. Eglitis, R.I.; Purans, J.; Popov, A.I.; Bocharov, D.; Chekhovska, A.; Jia, R. Ab initio computations of O and AO as well as  $\text{ReO}_2$ ,  $\text{WO}_2$  and  $\text{BO}_2$ -terminated  $\text{ReO}_3$ ,  $\text{WO}_3$ ,  $\text{BaTiO}_3$ ,  $\text{SrTiO}_3$  and  $\text{BaZrO}_3$  (001) surfaces. *Symmetry* **2022**, *14*, 1050. [\[CrossRef\]](#)
205. Eglitis, R.I.; Kotomin, E.A.; Popov, A.I.; Kruchinin, S.P.; Jia, R. Comparative ab initio calculations of  $\text{SrTiO}_3$ ,  $\text{BaTiO}_3$ ,  $\text{PbTiO}_3$  and  $\text{SrZrO}_3$  (001) and (111) surfaces as well as oxygen vacancies. *Low. Temp. Phys.* **2022**, *48*, 80–88. [\[CrossRef\]](#)
206. Eglitis, R.I.; Popov, A.I. Comparative ab initio calculations for  $\text{ABO}_3$  perovskite (001), (011) and (111) surfaces as well as  $\text{YAlO}_3$  (001) surfaces and  $F$  centers. *J. Nano Electron. Phys.* **2019**, *11*, 01001. [\[CrossRef\]](#)
207. Panthi, G.; Park, M. Approaches for enhancing the photocatalytic activities of barium titanate: A review. *J. Energy Chem.* **2022**, *73*, 160–188. [\[CrossRef\]](#)
208. Liu, X.; Lv, S.; Fan, B.; Xing, A.; Jia, B. Ferroelectric Polarization-Enhanced Photocatalysis in  $\text{BaTiO}_3$ - $\text{TiO}_2$  Core-Shell Heterostructures. *Nanomaterials* **2019**, *9*, 1116. [\[CrossRef\]](#)
209. Rauf, A.; Wang, W.; Zheng, D.; Feng, S.; Khan, U.; Akbar, A.R.; Peng, G.; Wu, Z.; Liu, F. Ferroelectric polarization induced charge separation in  $\text{BaTiO}_3/\text{Si}$ : A pathway for non-PN junction photovoltaics. *Ceram. Int.* **2022**, *48*, 28413–28418. [\[CrossRef\]](#)
210. Abuova, A.U.; Matrikov, Y.A.; Kotomin, E.A.; Piskunov, S.N.; Inerbaev, T.M.; Akilbekov, A.T. First-principles modeling of oxygen adsorption on Ag-doped  $\text{LaMnO}_3$  (001) surface. *J. Electron. Mater.* **2020**, *49*, 1421–1434. [\[CrossRef\]](#)
211. Fan, J.; Song, Z.; Tan, B.; Wang, H.; Chen, Z.; Xu, H.; Yan, J. Enhanced hydrogen production via piezo-photocatalytic water splitting using  $\text{BaTiO}_3$  crystal phase engineering. *J. Solid State Chem.* **2025**, *345*, 125251. [\[CrossRef\]](#)
212. Chandrasekaran, S.; Wang, Q.; Liu, Q.; Wang, H.; Qiu, D.; Lu, H.; Liu, Y.; Bowen, C.; Huang, H. Dynamic regulation of ferroelectric polarization using external stimuli for efficient water splitting and beyond. *Chem. Soc. Rev.* **2025**, *54*, 2275–2343. [\[CrossRef\]](#)
213. Nagarajarao, S.H.; Mokshanatha, P.B.; Servottam, S. Photocatalytic water treatment by perovskite materials. *Synth. Met.* **2025**, *312*, 117875. [\[CrossRef\]](#)
214. Assavachin, S.; Sawangphruk, M.; Osterloh, F.E. Ferroelectric  $\text{BiFeO}_3$  and  $\text{BaTiO}_3$  photocatalysts for photoelectrochemical water splitting. *Curr. Opin. Chem. Eng.* **2025**, *48*, 101123. [\[CrossRef\]](#)
215. Chandrappa, S.; Myakala, S.N.; Koshi, N.A.; Galbao, S.J.; Lee, S.-C.; Bhattacharjee, S.; Eder, D.; Cherevan, A.; Murthy, D.H.K. Unveiling valence state-dependent photocatalytic water splitting activity and photocathodic behavior in visible light-active iridium-doped  $\text{BaTiO}_3$ . *ACS Appl. Mater. Interfaces* **2024**, *16*, 8763–8771. [\[CrossRef\]](#) [\[PubMed\]](#)
216. Parangusan, H.; Bhadra, J.; Ahmad, Z.; Karuppasamy, K.; Mallick, S.; Touati, F.; Al-Thani, N. Hierarchical  $\text{BaTiO}_3/\text{NiFe}_2\text{O}_4$  nanocomposite as an efficacious photoanode for photoelectrochemical water splitting. *Ceram. Int.* **2022**, *48*, 29136–29143. [\[CrossRef\]](#)

**Disclaimer/Publisher’s Note:** The statements, opinions and data contained in all publications are solely those of the individual author(s) and contributor(s) and not of MDPI and/or the editor(s). MDPI and/or the editor(s) disclaim responsibility for any injury to people or property resulting from any ideas, methods, instructions or products referred to in the content.